

6. Automotive Metals - Crosscutting

A. Magnesium Research and Technology Development

Principal Investigator: Eric A. Nyberg
Pacific Northwest National Laboratory
PO Box 999, Richland, Washington 99352
(509) 375-2103; e-mail: Eric.Nyberg@pnl.gov

Technology Area Development Manager: William Joost
(202) 287-6020; e-mail: william.joost@ee.doe.gov

Field Technical Manager: Mark T. Smith
(509) 375-4478; e-mail: mark.smith@pnl.gov

Contractor: Pacific Northwest National Laboratory
Contract No.: DE-AC05-76RL01830

The Magnesium Research and Technology Development (MR&TD) project supports and manages efforts to increase the use of magnesium (Mg) in automotive and other transportation applications. These projects look at property improvements while reducing costs associated with existing or new processes and manufacturing technologies.

Objectives

- Support the U.S. Department of Energy (DOE)/United States Automotive Materials Partnership (USAMP) Magnesium Front End Research and Development (MFERD) project in collaboration with China and Canada.
- Increase awareness and familiarity with magnesium as a viable option for automotive applications.
- Compile, document, and evaluate state-of-the-art research and development (R&D) activities in Mg research around the world as a resource to best determine where U.S. government resources should be directed.

Approach, including partner/collaborator and path to technology transfer and commercialization

- Provide the U.S. MFERD Project Steering Committee (PSC) member from the DOE Office of Vehicle Technologies with information as it relates to funding or technical developments and challenges of the MFERD project. Review the monthly U.S. MFERD task leaders' progress and note any financial issues relevant to DOE funding.
- Attend and evaluate both the semi-annual and annual U.S. MFERD task leaders' review meetings and assess effectiveness of the nine U.S. tasks of the MFERD and Magnesium Front-End Design and Development (MFEDD) projects.

- Conduct quarterly teleconferences with the Chinese and Canadian Project Technical Committee (PTC) co-chairs for the organization of the annual MFERD report and annual review meeting.
- Report on significant technical progress in international research related to Mg R&D.
- Promote international non-competitive Mg R&D.
- Develop and maintain the Mg R&D Bibliographic Database located at magnesium.pnl.gov.

Milestones, Metrics and Accomplishments

- Milestone 1: Conduct and report on the gaps in international research related to Mg R&D and implement into new basic science R&D Program (December 2008).
 - This milestone was completed through the issuance of the October 2008 research report to Dr. Joseph Carpenter entitled, “International Experience and Gaps in Magnesium Research and Development in the Automotive Industry.”
- Milestone 2: Update the Magnesium R&D Bibliographic Database located at magnesium.pnl.gov (September 2009).
 - This milestone was completed by periodically updating the bibliographic database to now include more than 1700 Mg-related citations.
- Milestone 3: Initiate planning and analysis of candidate direct liquid metal processing and direct sheet-forming technologies in support of a technical roadmap for Light Metal Processing and Manufacturing (LMPM) (September 2009; completed December 2009).
 - This milestone was completed with the identification of several candidate direct metal-forming process technologies, including the Alcoa Liquid Metal Extrusion, Large Strain Machining Extrusion (Purdue University) and technology updates for semi-solid processing. Oak Ridge National Laboratory has been engaged in the LMPM assessment to develop a direct metal-forming cost model based on an earlier DOE-funded Twin Roll Casting cost model.
- Milestone 4: Provide a framework for a U.S. Magnesium Fundamental and Applied R&D Program that crosses government offices.
 - This milestone was completed through the continued interaction with Dr. Suveen Mathaudhu at the U.S. Army Research Laboratory (ARL), Dr. Sean Agnew at the University of Virginia, representatives at the National Science Foundation (NSF), and Dr. John Vetrano at the DOE’s Office of Basic Energy Sciences. In 2010, ARL will fund a workshop to identify areas of interest to fund basic, fundamental Mg research. Dr. Agnew, NSF, and DOE continue to investigate a meaningful framework with which to form a collaborative research program. It is expected that an initiative to fund basic Mg R&D can begin in calendar year 2010.

MFERD:

In FY 2009, EA Nyberg was the MFERD PTC co-chairman responsible for coordinating the quarterly PTC teleconferences, organizing the annual review, and coordinating the U.S. portion of the annual report in both English and Chinese. It has been critical to maintain frequent, open communication with the Canadian and Chinese PTC members and has resulted in significant technical progress in a relatively short time. As a DOE-funded program, U.S. tasks are driven by USAMP representatives. Through monthly teleconferences, the USAMP task leaders were able to provide frequent updates regarding progress and issues. Specifically as MFERD co-chair, activities included:

- Reviewed progress by the nine U.S. task leaders
- Participated in quarterly international conference calls with PTC members from China and Canada
- Edited the 2009 U.S. and International semi-annual and annual MFERD Project Reports
- Reviewed the U.S. task leaders annual presentations held at the United States Council for Automotive Research (USCAR) headquarters on November 19, 2009
- Maintained a central repository for electronic project files available to all project members
- Co-organized the annual Task Leaders and PSC/PTC meeting held in Niagara, Canada
- Co-authored, with other PTC members, a paper published in the October 2008 (FY 2009) issue of *Advanced Materials and Processes*, entitled, “Magnesium for Future Autos: Magnesium-intensive vehicles and enabling technologies are under development through an international collaboration,” which highlights a model for international collaborative success.

MRETD:

- Expanded the publicly available Mg bibliographic database located at www.magnesium.pnl.gov to more than 1700 publications and presentations on Mg R&D
- Invited presenter at the International Magnesium Association’s meeting in Taiyuan, China (June 2009)
- 2009/2010 Magnesium Outgoing Committee chairman organizing the 2009 Magnesium Technology Symposium and editing the associated technical proceeding
- Served on the International Program Organizing Committee for the 8th International Conference on Magnesium Alloys and their Applications in Weimar, Germany (October 2009)

Future Directions

- Coordinate the Phase 2 MFERD Project Steering Committee meeting that will be held in Seattle, Washington in March 2010.
- Coordinate the 2010 MFERD annual meeting that will be held in the U.S. (October 2010). This annual meeting requires contracting for hotel, dining, and meeting space. It also requires contracting for translation and production of the bilingual 2009 annual report (book) (see Figure 1).
- Develop national and international collaboration with the U.S. Army, the National Science Foundation (NSF), and the DOE on efforts for fundamental Mg R&D.
- Continue to evaluate and propose Mg R&D activities that are unique and necessary.
- Maintain an awareness of the latest R&D by participationg on the TMS Magnesium Light Metals Committee and Symposium and other international magnesium committees as available.

Introduction

The primary purpose of this project is to support the Canada-China-U.S. collaborative project, Magnesium Front End Research and Development (MFERD). The goal for Phase 1 of the MFERD

project was to develop key enabling technologies for a lightweight magnesium (Mg) front-end body structure and other body applications. The MFERD project has been developing enabling technologies in areas such as high-integrity casting, wrought Mg processing, and Mg and dissimilar metal joining and corrosion. These developments have generated additional scientific understanding in corrosion science; crash-energy management; fatigue; and noise, vibration, and harshness (NVH) performance. The project also provides a platform for Mg research collaboration in Canada, China, and the U.S.

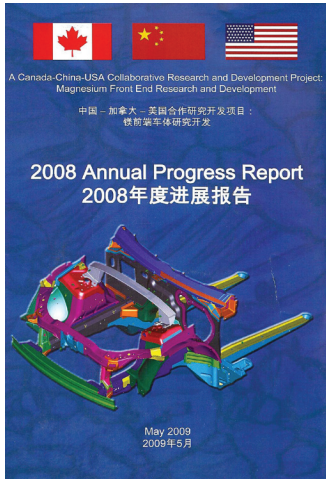


Figure 1. 2008 MFERD Bilingual Annual Report

Background

The goal of Phase 1 of the MFERD project was to develop key enabling technologies (body casting, extrusion, sheet, and joining) and knowledge base (crashworthiness, NVH, durability, and corrosion) for primary (load-path) body applications of Mg alloys. The following are some specific objectives:

- Define materials and develop manufacturing processes for Mg body castings, extrusions, sheet, and joining technologies.
- Develop knowledge base and define Mg body technical requirements in crashworthiness, NVH, durability, corrosion, and surface finishing.
- Enhance the infrastructure for integrated computational materials engineering for Mg applications, including alloy design/development, process optimization, and component manufacturing.
- Develop a total life cycle analysis showing the net benefit of vehicle lightweighting using Mg versus energy consumption, emission, and pollution in Mg production.
- Promote high-quality professionals and students educated in materials science, engineering, and Mg research and development (R&D) infrastructure in Canada, China, and the U.S.
- Establish automotive original equipment manufacturer (OEM)/supplier/academia collaboration in Mg body applications.

PNNL Approach to Supporting the MFERD Project and Database Development

Mr. EA Nyberg continues as the 2009/2010 U.S. Project Technical Committee Chairman as a liaison to the PSC representative at DOE. This position has established continuity that has been valuable in dealing with colleagues from the other participating countries, particularly China. This enables frank and open communication with the other PTC members, especially when the professional relationship is critical to workable progress. This participation has made technical issues or cultural complexities less of a hindrance than otherwise might be expected. During the annual review meeting, PSC members expressed appreciation to the PTC and task leaders for the amount of work that has been completed for the project's relatively short existence.

With the assistance of software engineers at Mississippi State University, PNNL has developed a MFERD SharePoint website. At the site, the non-proprietary project information is collected at a central location/depository for the international task teams to access the documents easily. This coordination is an effort to make communicating and sharing information efficient and effective for all of the team members around the world.

The magnesium bibliographic database—www.magnesium.pnl.gov (Figure 2)—was updated this year to include more than 1,700 referenced papers and presentations. This database is linked at both the TMS Magnesium and the International Magnesium Association websites, making the database an increasingly available tool to researchers exploring state-of-the-art Mg R&D around the world.



Figure 2. Magnesium Bibliographic Database

As an invited speaker, Nyberg attended the IMA Taiyuan Global Magnesium Conference in Taiyuan, China in June 2009, where he presented background and overview information on the international collaboration and technical developments produced via the three-country MFERD project (Figure 3). He also attended the 8th International Conference on Magnesium Alloys and Their Applications, the world's largest gathering of technical topics related to Mg alloys (Figure 4). Nyberg also highlighted the positive benefits and productive results of the three-country, international MFERD project in the October 2008 issue of *Advanced Materials and Processes* (Figure 5).

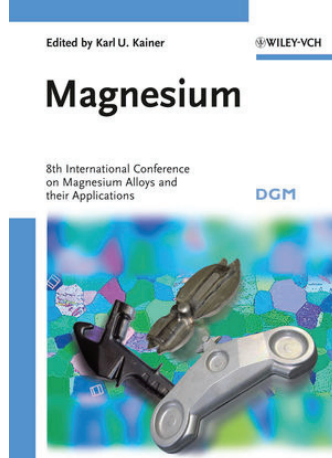


Figure 3. International Magnesium Conference



Figure 4. International Conference on Magnesium Alloys and Their Applications (2009)

Figure 5. Article from Advanced Materials and Processes (October 2008)

Current and Future Work

MFIRD: coordinate the PSC-PTC meeting on March 25, 2010 in Seattle, Washington. This will be an important meeting as its intention is to confirm the PSC's commitment to Phase 2 of the project.

Future work will involve evaluating the progress of the nine U.S. tasks, as well as participating in task leader review meetings, PTC quarterly teleconferences, reporting results, and making recommendations to the U.S. PSC Chairman. Currently, the PTC is planning the fourth annual task leaders meeting to be held in the U.S. in October 2010. This meeting will be followed by a joint PSC/PTC meeting.

In consideration for future funding, Mg research opportunities within and outside of PNNL will be reviewed and proposed to DOE. Oversight, management, and updates of the publicly available Mg R&D database at www.magnesium.pnl.gov also will continue.

Conclusions

Primarily, this technical project is aimed at assisting in the management of the U.S. portion of the three-country MFERD project. To date, the third full year of the MFERD project is complete, and the annual report is being prepared for release at the annual meeting in October 2010.

Efforts continue to develop coordinated research between countries (Germany, China, and Canada) and among U.S agencies (i.e., Army, NSF, and DOE).

Presentations/Publications/Patents

Nyberg EA. 2009. "Success of Global Collaboration: The Magnesium Front-End Research and Development (MFERD) Project." April 8, 2009, Taiyuan, Shanxi, China. IMA 2009 Taiyuan Global Magnesium Conference and Exhibition.

Nyberg E, A Luo, K Sadayappan, and W Shi. 2008. "Magnesium for Future Autos: Magnesium-intensive vehicles and enabling technologies are under development through an international collaboration." *Advanced Materials and Processes* 166(10):35-37.

Luo A, E Nyberg, K Sadayappan, and W Shi. 2009. "2008 Annual Progress Report-A Canada-China-USA Collaboration." May 2009, Niagara-on-the-Lake, Canada.

E Nyberg, et al., ed 2009. *Magnesium Technology 2009*. TMS, Warrendale, Pennsylvania.

B. Magnesium Front End Design and Development

Principal Investigator: Alan A. Luo
General Motors Research & Development Center
MC 480-106-212
30500 Mound Road
Warren, MI 48090-9055
(586) 986-8303; e-mail: alan.luo@gm.com

Program Technical Administrator: Robert C. McCune
Robert C. McCune and Associates, LLC
5451 S. Piccadilly Cir.
West Bloomfield, MI, 48322-1446
(248) 661-0085; robert.mccune@sbcglobal.net

Technology Area Development Manager: William Joost
(202) 287-6020; e-mail: william.joost@ee.doe.gov

Field Project Officer: Magda A. Rivera
(304) 285-1359; email: magda.rivera@netl.doe.gov

Expert Technical Monitor: C. David Warren
(865) 574-9693; e-mail: warrencd@ornl.gov

Contractor: U.S. Automotive Materials Partnership
Contract No.: FC26-02OR22910

Objectives

The goal of the project has been the engineering design, computer-aided engineering (CAE) analysis and technical cost modeling of exemplary magnesium-intensive, front-end structures for selected unibody (body-frame-integral: BFI) and body-on-frame (BOF) vehicle architectures having the following design stretch targets:

Mass reduction target: 60% lighter than comparator steel baseline structures and 35% lighter than comparator aluminum structures for mid-size passenger car, with comparable strength, stiffness and crashworthiness.

Vehicle mass distribution: Shift the front-to-rear mass ratio by -1/+1(%) toward 50/50 for the rear-wheel drive architecture, thereby improving handling capability.

Determine by technical cost modeling the cost penalty of implementation for 100,000 vehicles/year production volumes, via part consolidation using large magnesium castings (e.g. dash panel, shotguns) and attractive pricing of magnesium in world markets. Target value is a maximum of \$8/kg (of mass saved).

Match or improved key performance characteristics such as stiffness, durability and NVH (noise, vibration and harshness) of a “multi-material” vehicle (MMV) ‘donor’ vehicle via computer simulation.

2009 Update on Objectives: With the designs nearing completion, the original targets remain as “stretch” targets with actual design performance not yet meeting the weight savings or safety targets and durability yet to be confirmed. Design and analysis work is continuing via limited extension of the project into the 1st quarter of 2010.

Approach

The organizational structure of AMD603 has been described in detail in the prior progress report [1]. The project consists of two Tasks: 1.) Design and 2.) Technical Cost Modeling (TCM). The designs are predicated on two vehicle structural archetypes: a body-frame-integral (BFI, also known as a ‘unibody’), principally used for passenger vehicles, and body-on-frame (BOF), which incorporates a separate (presumably steel) frame, to which the body structure is attached in final assembly. This latter structure is primarily employed for light trucks and many SUVs. Both tasks have been commissioned to contractors with design and manufacturing data made available from the OEMs as required. There are no other supplier participants.

Task 1. Design.

The design task was originally divided into stages to incorporate data being simultaneously developed with regard to materials and processes as part of the AMD604 (Magnesium Front End Research and Development- ‘MFERD’) project. The initial (Phase 1) design was intended to utilize handbook properties of materials, and best general design information as was available at the outset of the project from the relevant OEMs or other sources. Phase 2 was intended to incorporate refinements to material properties occurring through AMD604 developments, and Phase 3 projects designs used optimized properties and manufacturing methods developed throughout the course of AMD604. The design Task also incorporated computer-aided engineering (CAE) techniques to explore such features as crashworthiness, modal analysis and durability. These critical topics are amenable to computer modeling when knowledge of deformation characteristics of the materials, including their strain-rate behaviors, cyclic deformation characteristics and fracture mechanics are well understood.

Task 2. Technical Cost Modeling.

Process-based technical cost modeling [2] has been employed to provide the following deliverables for the two front-end designs (BFI and BOF):

Primary Mg production costs and market impact of the electrolytic vs. direct thermal reduction (Pidgeon) processes.

Detailed cost analysis and report for all the components and assembly identified by the Design Task for both the BFI and BOF designs.

Assessment of current steel designs for both the BFI and BOF as comparators for weight and cost.

The cost-modeling Task was also divided into phases. Phase 1 originally included the primary Mg production analysis and the component cost of individual parts for each design, however final development of the primary Mg production models occurred later in the project due to the inherent complexity of these models and difficulty obtaining specific process information. Phase 2 included the assembly of the components to each other and to the remainder of the body structure. Phase 2 also incorporated updates to the front-end design as determined by the design evolution or information gathered by AMD604. The cost analysis included part manufacture, corrosion protection treatment as well as any surface finishing, machining or any other process each component requires to allow it to be attached or integrated with the rest of the front-end assembly. The overall cost of the assembly including components will be determined for each design as compared to the steel baseline.

Accomplishments

- The Phase 3 Final Design Review will be conducted during December 2009 (BOF design) and January 2010 (BFI design), with subsequent presentation to the USAMP OEM community and the DOE shortly thereafter. Interim design reviews were conducted and documented on a regular basis throughout 2009.
- Phase 2 Deliverables: “Best” mechanical property data, including deformation and fracture behaviors, and manufacturing implications (e.g. joining, finishing) have been communicated from the AMD604 Task teams and incorporated by the supplier (Cosma Engineering, Troy, MI) in the design and analyses.
- Phase 3 Progress: With the final information from the AMD604 task teams available between May 2009 and late September 2009, the last phase of the designs for both the BFI and BOF front ends is nearly complete. The challenges on meeting the crashworthiness of the donor structures are clear. The current designs are struggling to meet the crashworthiness targets with magnesium while simultaneously meeting the weight saving target.
- Mechanical Property Status: As of September, 2009, the ‘best’ material properties acquired in AMD604 have been incorporated into the designs. Further work on improving material properties, especially for the castings and extrusions will continue in the AMD604 follow-on (Phase 2) but will obviously not be in time to influence the current AMD603 designs. Super vacuum die cast AM60B can reach ultimate tensile strengths of ~220 MPa with elongations of 9% or greater, however the best yield strength values have been near 125 MPa for this process, short of the 140 MPa design goal.
- One objective for the Phase 2 “MFERD” project arising from this project will be the assessment of several alternative Mg alloys, including higher aluminum content versions of the AM series and rare-earth microalloyed systems for improved yield strength of castings (with heat treatment) and more isotropic mechanical properties of wrought magnesium alloys.
- Cost Modeling Review: A comprehensive initial review of component cost models was conducted by the contractor, Camanoe Associates (Cambridge, MA) in 2008 and updated in December, 2009. While the extractive metallurgy models are still under development, the basic formalism of their organization is in hand.
- Models for basic part fabrication using die casting (both high-vacuum and Thixomolding® processes), sheet fabrication and extrusion are complete, as is the baseline steel fabrication model.
- Status of specific design targets – BFI architecture:
 1. Part count reduction: 44 pieces (35 MFE vs. 79 steel baseline – or 56%).
 2. Mass reduction: 38.2 kg (45%) (With equivalent global body stiffness to the steel baseline, prior to meeting full requirements of crash, NVH and durability performance).
 3. Materials technologies: 15 castings, 3 extrusions, 17 formed magnesium sheet or aluminum stampings.
 4. Joining strategy developed include friction stir linear and spot welding (FSW), metal inert gas (MIG) welding, self-piercing rivets (SPR), and adhesive bonding.
 5. Crashworthiness: using the latest material properties (including provision for material fracture at maximum strains) the crash performance of the current magnesium front end design falls short of the steel baseline vehicle in IIHS Deformable Barrier and the NCAP 35 mph full frontal impact.

- 6. Modal analysis: full body, structure-only modes occur at higher frequencies than the baseline, indicating generally greater structural stiffness.
- 7. Assembly sequence has been identified permitting prospective plant layout and more detailed cost modeling.
- 8. The current corrosion prevention strategy is to pre-treat all the component parts; join the parts into the front end assembly, and further topcoat the entire assembly before attachment to the remainder steel body-in-white.
- Status of specific design targets – BOF architecture:
 - 1. Part count reduction: 2 pieces (18 MFE vs. 20 steel baseline – or 10%). One piece of the baseline design (the grill opening reinforcement) is already magnesium.
 - 2. Mass reduction: 14.19 kg (57.095kg to 42.907kg, or 24.8%).
 - 3. Materials technologies: 7 magnesium die castings, 4 steel stampings, 6 aluminum stampings, and one injection molded plastic part.
 - 4. Joining technologies: aluminum fasteners, self-piercing rivets, adhesive bonding, and resistance spot weld (steel components).
 - 5. Crashworthiness: NCAP and IIHS targets appear to be achievable.
 - 6. Modal Analysis: meets or exceeds baseline structure.
 - 7. Assembly sequence: One major sub-assembly; other magnesium parts to be assembled in vehicle body shop prior to painting.
 - 8. Corrosion protection: All Mg piece parts cleaned and pretreated prior to assembly. Sub-assembly structure topcoated as assembly; individual Mg parts topcoated separately.
 - 9. Isolation: TBD between Mg and steel elements. Topcoating process may be sufficient.
- Specific progress in the Technical Cost Modeling project includes:
 - 1. Updated component manufacturing models for die-casting (both super vacuum and Thixomolding®), warm forming, aluminum stamping, and extrusion, to incorporate the latest Phase 1 design changes.
 - 2. Technical cost modeling has permitted design modifications in such areas as sheet-formed parts, resulting in overall cost savings for the BFI front-end structure.
 - 3. Multiple joining processes for the unibody structure contribute to a greater expense of assembly, despite fewer piece parts than the comparator structure in sheet steel. Determined preliminary piece cost for magnesium-designed components.
 - 4. The framework for the surface treatment model is complete, although it needs to be tailored to the relative sizes of the piece parts or subassemblies being processed.
 - 5. Likewise, the models for electrolytic and thermal reduction (Pidgeon) extractive processes are developed, however they need to be benchmarked and verified for process and equipment assumptions by subject matter experts in the magnesium industry.

Future Direction

Crashworthiness: The design team and the project core team will continue to investigate design alternatives to meet the donor vehicles' safety targets at the minimum weight. For the BFI design, the use of aluminum components in critical energy absorbing structures will be investigated if the magnesium performance cannot be made equivalent to the donor vehicle.

Manufacturing: While initial build sequences have been proposed by the contractor, certain specifics, such as corrosion protection surface treatment and joining methodologies have not been fully developed. These developments are expected to emerge from the AMD604 research and development project – Phase 2 follow-on.

Cost Modeling: Refine the present process cost models and continue interactions between the design and cost modeling teams to provide insights and direction to the front end design to improve the component and assembly costs. Complete the extractive metallurgy models.

Continue to seek weight reduction opportunities through down-gauging, part consolidation, or other means to more closely approach the original design stretch target.

Introduction

Background for AMD603, Magnesium Front End Design and Development (MFEDD) has been provided in a prior annual progress report [1]. MFEDD is complementary to both the AMD604 (Magnesium Front End Research and Development - MFERD) and the USAMP MMV (Multi-material Vehicle) projects. Whereas, AMD604 is predicated on development of enabling magnesium technologies via leveraging with Canadian and Chinese magnesium experts on a collaborative basis, AMD603 is confined to the OEM partners of USAMP (i.e. Ford, GM and Chrysler) and two selected suppliers focused on design (Cosma Engineering, Troy, MI) and technical cost modeling (Camanoe Associates, Cambridge, MA).

The “front end” structures envisioned as the objectives of the project include two structural archetypes: 1.) a unibody (or body-frame-integral - BFI) structure as illustrated in [Figure 1](#), and a body-on-frame (BOF) approach as shown in [Figure 2](#) (shown without the underlying steel frame). The former structural type is associated with light passenger vehicles, whereas the latter is incorporated in light trucks and sport utility vehicles (SUVs). The traditional unibody structure is assembled typically from individually stamped steel parts which are then joined together, usually by resistance spot welding, and often incorporate adhesive bonding or “weld bonding” in combination with resistance spot welding for improved strength, stiffness and performance. The attraction for use of magnesium in the BFI structure arises from both weight reduction opportunity at comparable stiffness, and the prospects of combining individual piece parts into entire subassemblies, via large-scale die casting. Such large cast parts, of which present day instrument panels and radiator supports are exemplary, have excellent dimensional properties and opportunity for reduced costs over assemblies of larger numbers of steel stampings.

The remainder of this report describes the status of the design exercise as of December 2009 and generalized outcomes of the cost modeling exercise to date.

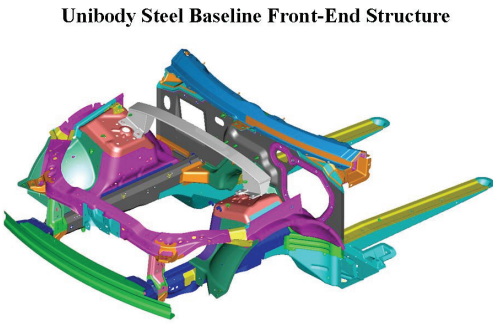


Figure 1. Unibody (BFI) steel front-end baseline structure for the donor vehicle.

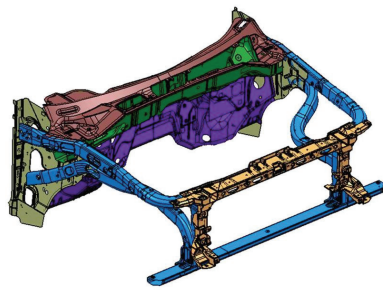


Figure 2. Baseline BOF donor vehicle steel structure.

Design Status

The “design review” is the fundamental mechanism by which proposal and discussion of design alternatives and attributes occurs within the automotive engineering community. **Table 1** depicts the ongoing agenda of design topics normally covered in some degree at each meeting. During the first two years of the project, the greater focus was on the BFI design and incorporation of “enabling technology” developments from USAMP Project AMD604. In FY 2009, greater attention was focused on the BOF design, owing firstly to substantial changes in both the baseline design as provided by the OEM (Ford), and closer attention to the details of integration of the magnesium-intensive portions of the structure into the baseline design.

Table 1. Design attributes for magnesium front end from the agenda for the design review process.

Magnesium Front End Design Attributes

1. Design CAD – structural design to match specified envelope.
2. CAE – crash studies by LS-DYNA analysis, durability.
3. Bill of Materials – parts listing, manufacture method and drawings.
4. Mass and part count summary.
5. Vibration modal analysis and structural stiffness by CAE.
6. Frontal crash analysis for NCAP and IIHS protocols.
7. Typical cross sections of major structures and substructures.
8. Joining strategy for magnesium components.
9. Magnesium-to-steel interface strategy.
10. Manufacturing implications.
11. Assembly protocol.
12. Corrosion prevention strategy.
13. Stress/durability evaluation – static and dynamic loading of structure.

The following section provides commentary on the status of each design review topic including any matters awaiting resolution as of the time of this report.

- *Design CAD (computer-aided design).* Front-end envelopes, including vehicle “hard points” and attachment points to remainder structures have been fully implemented in physical designs and individual component parts for both BFI and BOF designs. For the BFI, the original design envelope was expanded to include a multi-piece aluminum floor pan and cowl extension brackets, thereby also addressing design item 9 regarding interfacing strategies to steel components. The BOF design retains all packaging and geometric considerations, although individual components implemented in magnesium, where possible, may be discernible from stamped or hydroformed steel counterparts on the baseline.

- *CAE (computer-aided engineering).* Selected analyses of BFI and BOF structures in modal analysis, crashworthiness and durability have either been completed or are in final stages of completion. Individual details are itemized in points 5, 8 and 13 below.
- *Bill of Materials.* All relevant Bills of Materials for BFI and BOF are complete, with exceptions noted in the following sections.
- *Mass and Part Count.* (BFI) Part count original (steel) is 79 pieces having a mass of 84.3 kg; magnesium-intensive front end is 35 parts (56% reduction), and mass of 46.1 kg (45% reduction). Parts currently include: 15 magnesium castings, 3 magnesium extrusions and 17 formed magnesium sheet or aluminum stampings. (BOF) 20 baseline parts (18 steel, 1 magnesium, 1 plastic) with mass of 57.095 kg, reduced to 18 parts (7 magnesium castings, 4 steel stampings, 6 aluminum stampings, and one plastic molding) having a mass of 42.907 kg (10% part count reduction; 24.9% mass reduction).
- *Vibration modal analysis and structural stiffness.* (BFI and BOF). Structural stiffnesses either match or exceed their respective baselines, and vibration modes tend to either match baselines or occur at higher frequencies, typical of stiffer structures.
- *Frontal Crash.* NCAP (New Car Assessment Program) 35 mph full frontal and IIHS (Insurance Institute for Highway Safety) deformable barrier.

(BFI) “Best value” Phase 1 MFERD material properties for AM60B (casting), AM30 (extrusion) and AZ31 (sheet) have not yielded capabilities for acceptable performance in either crash simulation format, despite various design schemes to avoid failure modes typically leading to material fracture and loss of material continuity. MFERD Phase 2 and ICME efforts on load-path critical components (e.g. extruded frame rails and crush boxes) will focus on reductions in anisotropic deformation behavior and premature fracture through improved alloys and processing. The present design exercise in the meantime has considered material substitution in the frame rails and adjacent components with extruded aluminum in order to more fully meet crash requirements. Although such substitution is beyond the original scope of this project, it is expected to provide directional guidance for structural lightweighting (viz. in multi-material vehicles) and performance in the anticipation of acceptable magnesium alloys in the future.

(BOF) This design benefits in crashworthiness from the incorporation of the underlying steel frame which plays the major role in absorption of frontal and offset crash energy. Magnesium structural components (e.g. ‘shotgun’ pieces) must however still absorb impact loading as well as connective supporting elements. To date, however, the BOF designs suggest that crashworthiness targets equivalent to the baseline structure will be achievable through section thickness adjustment of cast magnesium components. (Current BOF designs do not call for any extruded or sheet magnesium components in the primary load path.)

- *Typical Sections.* All ‘typical’ cross sections at various points on both structures are visible through the CAD programs and a compendium of such sections is available through the supplier.
- *Joining Strategy for Magnesium Components.* (BFI) Structural adhesive bonding is included at many of the joint lines, supplanting other joining methods (e.g. self-piercing rivets, friction spot welds). The principal manufacturing stipulation for adhesive bonding, however, is that all surfaces receive some form of chemical pretreatment permitting bonding to occur. Whereas coiled or sheet materials such as steel and aluminum in comparator structures are readily bondable with minimal surface preparation, magnesium, particularly as die castings and extrusions, requires chemical cleaning to remove process artifacts (e.g. lubes, oxides) and subsequent passivation or “pretreatment” to thwart undercutting corrosion and loss of joint strength. This aspect of magnesium component assembly assumes markedly differing

manufacturing requirements than current practice for sheet steel and aluminum, which do not require metal pretreatment before adhesive bonding. Furthermore, it is not entirely clear at this point what secondary joining processes may be hampered by surface pretreatments which are required for adhesive bonding (e.g. resistance welding).

(BOF) Joining assumptions for the BOF structure are similar to those of the BFI, but with greater emphasis on use of threaded aluminum fasteners, and defined needs for isolation with remaining steel structural points. A substantial magnesium plenum structure has individual components pretreated and adhesively bonded as with the BFI. Additional large Mg castings (shotguns, brackets and grill opening) are treated as is current practice for the Mg grill-opening reinforcement used in light trucks.

- *Magnesium-to-Steel Body Interface Strategy.* The bill of materials has been modified in the case of the BFI structure to permit a number of aluminum “interface” parts as isolators between the predominant magnesium front end and remainder of the steel unibody. Isolation through use of aluminum is currently a practice in the industry. Current assumptions for the BFI front-end ‘clip’ call for complete encapsulation of the assembly with a polymeric topcoat, thereby minimizing need for additional insulating isolators. The evaluation of this approach is experimentally pending. Similarly, the BOF structure is expected to exploit topcoated pieces and subassemblies minimizing or obviating the need for additional isolation. Neither the design team nor the AMD604 corrosion team has considered needs for electrical continuity through the isolated structures.
- *Manufacturing Implications.* (BFI) Each component part has been assessed for manufacturing capability by the relevant AMD604 sub team, and recommendations provided regarding optimal choice of technologies. (BOF) All magnesium components at this point are expected to be large-scale die castings.
- *Assembly Protocols.* Assembly sequences and methods for BFI and BOF structures have been provided by the supplier, and in the case of the BFI design, tentative plant layouts for fixturing, adhesive bonding and friction stir welding (FSW) have been considered. Cost models for the principal methods of fabrication have been developed by Camanoe.
- *Corrosion Prevention Strategy.* The AMD604 Task 1.4 (Corrosion and Surface Treatment) team has provided background assumptions for this item. Most notably, cleaning and pretreatments specifically targeted for magnesium are required at a much earlier stage of manufacture in order to affect the large degree of adhesive bonding employed. Subassemblies and individual component parts are delivered to the manufacturing body shop effectively with final corrosion protection in place. Isolation strategies are also predicated on this assumption.
- *Stress/Durability Analysis (CAE).* The fatigue data including all required coefficients of the three design materials (AM60B super vacuum die casting, AM30 extrusion and AZ31 sheet) has been provided by the AMD604 fatigue task team. Final assessment of fatigue durability is expected for BFI and BOF designs by the end of the first quarter of 2010.

Technical Cost Modeling

Primary Magnesium Production. **Figures 3 and 4** show generalized schematizations that now form the basis for calculations in the present technical cost modeling architecture. The two processes under consideration are the direct silico-thermic reduction or ‘Pidgeon’ process, used primarily in China and the electrolytic extraction process used in the U.S. and other locations worldwide. Specifically because of the proprietary nature of electrolytic processes, concise data regarding unit processes is largely unavailable and validation of any proposed models will require cooperation and support from primary producers willing to review the technical cost modeling approach.

Magnesium Piece Part Cost Models. Technical cost models have been devised for the principal manufacturing processing employed in both the baseline steel structure and proposed magnesium structures for both the BFI and BOF architectures. The models include both piece part production and also assembly and finishing models where the underlying sequences and methods have been put forth by the designers.

Primary Mg Model Structure – Pidgeon Process

- Model governed by materials flow

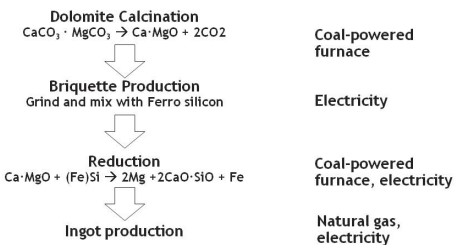


Figure 3. Block diagram of silico-thermic reduction (Pidgeon) process showing major unit subprocesses.

Primary Mg Model Structure - Electrolytic

- Model governed by materials flow

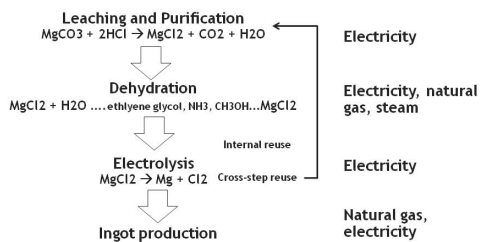


Figure 4. Block diagram of generalized electrolytic extraction process for Mg.

For the primary part production, both “super” vacuum die casting and Thixomolding® have been considered, the latter process associated with Canadian partners in the international MFERD program. **Figure 5** shows a summary of fractional contributions for each forming process considered in the overall models.

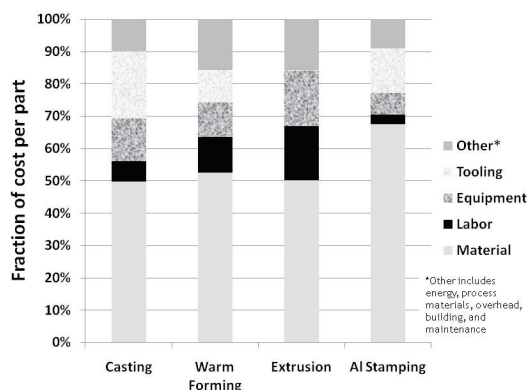


Figure 5. Approximate cost element breakdown for magnesium components as formed by casting, extrusion and sheet processes, as well as aluminum formed by stamping.

Individual cost models for each forming technology, and each individual part are different from each other, incorporating such factors as part size and impact on capital and tooling. However, some common features have emerged from the studies: 1.) a general tendency for the material cost to be among the largest single factors contributing to overall component cost, and 2.) a tendency for extrusion to show a generally lower cost of the individual forming tool. This manufacturing cost characteristic is well-known for the comparable aluminum extrusion process.

Figure 6 illustrates the overall comparison of one particular magnesium BFI substructure to that of the steel baseline considering only materials, fabrication and assembly costs. The cost structure has been normalized to a value of 1.00 for the magnesium structure. Surface finishing costs have not been included in this comparison.

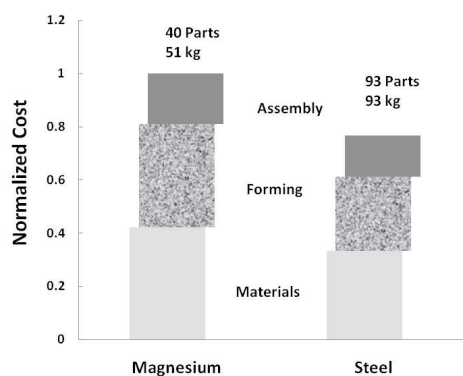


Figure 6. Comparison of normalized costs of one specific magnesium-intensive design and steel BFI baseline front end structure, not including surface finishing.

Conclusions

At the end of its third and final year, the AMD603 project has concluded all design phases ranging from handbook estimates to optimized material properties as considered in the companion R&D project, for both BFI and BOF structural archetypes. Crashworthiness, particularly of the BFI structure falls below requirements, primarily due to the physical metallurgy limitations of the selected magnesium material in the specific loading situation. The weight reduction value of 45% for the BFI structure, however, suggests a directional opportunity for the approach, even if a limited number of subsidiary parts are formed in aluminum. The BOF architecture takes advantage of the existing steel frame to aid in crashworthiness, however the weight reduction values of ~ 25% fall well below the original stretch target of 60%. Continuing design efforts of a ‘generic’ nature applied to surrogate or ‘demonstration’ structures will be incorporated directly into the ‘MFERD’ follow-on project.

References

1. A. A. Luo, R. C. McCune, J. A. Carpenter, A. D. Yocum, and P. S. Sklad, “AMD603 Magnesium Front End Design and Development,” FY 2008 Progress Report to DOE, (in press).
2. R. Kirchain and F.R. Field III, “Process-Based Cost Modeling: Understanding the Economics of Technical Decisions,” Encyclopedia of Materials Science and Engineering, 2001

Acknowledgments

The success of this project is due to the dedicated efforts of team members at Chrysler, Ford, and General Motors, as well as the suppliers Cosma Engineering and Camanoe Associates. David Wagner of Ford, Theresa Lee of GM and Steve Logan of Chrysler are specifically acknowledged for their significant contributions and tireless efforts. The continuing support of our respective organizations and the US Department of Energy is gratefully acknowledged.

C. Magnesium Front End Research and Development

Principal Investigator: Alan A. Luo
General Motors (GM) Research & Development Center
MC 480-106-212
30500 Mound Road
Warren, MI 48090-9055
(586) 986-8303; e-mail: alan.luo@gm.com

Program Technical Administrator: Robert C. McCune
Robert C. McCune and Associates, LLC
5451 S. Piccadilly Circle
West Bloomfield, MI, 48322-1446
(248) 661-0085; e-mail: robert.mccune@sbcglobal.net

Technology Area Development Manager: William Joost
(202) 287-6020; e-mail: william.joost@ee.doe.gov

Field Project Officer: Magda A. Rivera
(304) 285-1359; email: magda.rivera@netl.doe.gov

Expert Technical Monitor: C. David Warren
(865) 574-9693; e-mail: warrencd@ornl.gov

Contractor: United States Automotive Materials Partnership (USAMP)
Contract No.: DE-FC05-02OR22910 through the National Energy Technology Laboratory

Objective

The objective of this US-Canada-China collaborative project has been the concurrent development of key enabling materials and manufacturing technologies and the accompanying performance knowledge base to permit design and implementation of magnesium (Mg)-intensive, automotive-body, front-end structures having substantially-reduced mass, but with performance and cost comparable to sheet-steel baseline structures. **Figure 1** illustrates an exemplary baseline steel unibody “front end” structure that served as the design envelope for the proposed magnesium-intensive structure. A second vehicle structure utilizing a “body-on-frame” archetype of many light trucks was also developed by the project.

Two aspects of this project are unique within the USAMP:

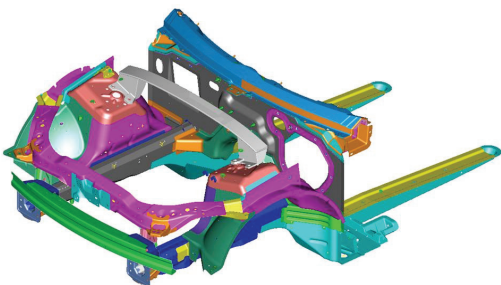
- The focus was on entire “front-end” structures as the developmental objective, in contrast to individual components, offering critical, vehicle-level benefits in terms of mass distribution and performance while challenging the technical community to devise materials and manufacturing approaches to permit affordable mass production of such structures.
- The organization and implementation of an international effort enlisting the best scientific and engineering expertise in Mg technology from the United States, Canada and China in a first-of-its-kind, global collaboration.

Approach

- *Organization and Administration:* Establishment of project and technical steering committees and systematic management of information and activities in a global environment including use of web-based platforms or other collaboration tools.

- *Partitioning of Projects:* Separation of the design function into a separate USAMP project (AMD 603) as well as Integrated Computational Materials Engineering - ICME (AMD 702 and 703), to facilitate handling of original equipment manufacturer (OEM)-sensitive design data and to permit a broader, more universal approach to ICME. The international “MFERD” project additionally included a life-cycle analysis (LCA) task, in which USAMP did not participate.
- *Enabling Technologies:* Assessment of the state-of-the-art and development of emerging technologies in primary forming, joining and finishing that would permit manufacture of the envisioned structures.
- *Knowledge Base:* Understand the knowledge gaps with regard to materials and structural performance in the intended application, particularly with regard to crashworthiness, noise-vibration harshness (NVH), fatigue and durability (including corrosion).
- *Technical Gateways:* Provided for assessment of progress against pre-determined metrics at sub-levels of the project, assuring that functional targets were achieved or, alternatively, that further efforts were discontinued if required metrics could not be achieved. Gateways were devised for both the design stage and also for the enabling technologies, and provided guidance in organizing the follow-on project. Overall timing and conceptual flow for projects AMD 603 and AMD 604 are illustrated in **Figure 2**, which also illustrates the positioning of the ICME project (viz. AMD703).

Figure 1. Exemplary unibody “front end” design envelope as presently implemented in sheet steel.



Magnesium Front End Project Structure and Timeline

AMD604 (MFERD): Phase 1. Enabling Technology Development (3-Country Collaboration)

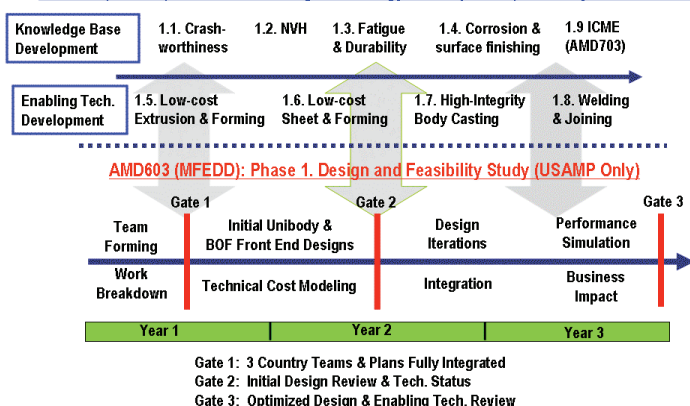


Figure 2. Schematization of AMD 603 and AMD 604 partitioning, timing and technical gateways.

Accomplishments

The relationships between activities of the individual task areas and overall project objectives are indicated in the “fishbone” diagram of [Figure 3](#). Targets for knowledge-based and enabling technologies are illustrated therein. General project accomplishments for FY 2009 are summarized below.

- Participated in 3rd International Review Conference held at Niagara-on-the-Lake, Ontario, from May 11-13, 2009.
- Contributed to the 570 page “Proceedings” volume detailing the 2nd year’s progress on the project in Canada, China and the U.S.
- Conducted meetings of the Project Steering Committee (PSC) and Project Technical Committee (PTC) in conjunction with the review at Niagara-on-the-Lake, and regular PTC conference calls during the prior year.
- Conducted the “Gate 3” technical review at the Niagara meeting and proposed that a “Phase 2” follow-on project be devised, focusing on a demonstration structure having key attributes of an entire front-end unibody structure, but at substantially lower research investment, without sacrifice of critical performance information.
- The USAMP annual review of Project AMD604 was held on November 19, 2009, and participants from the Canadian teams were in attendance. A group of U.S. participants attended the Canada annual review at the University of Windsor on September 23, 2009.
- Individual Task Team international conference calls were conducted at various times during the project year.
- The USAMP AMD604 Project presented its “Gate 3” review and proposal for Phase 2 to the AMD Board of Directors on September 29, 2009, and after some refinement was then presented and approved by the USAMP Steering Committee on October 14, 2009, pending final approval by the U.S. DOE.

USAMP AMD 604 Task Area Highlights are as follows:

Task 1.1 Crashworthiness - Completed stress vs. strain at various strain rates testing of AM60B and AM50 vacuum die cast materials complementing prior measurements of AM30 extrusion, AZ31 extrusion and AZ31 sheet. Fit the acquired stress vs. strain data to the available LS-DYNA material model, MAT_124, for use in computer prediction of component response. Predicted the response of AM30 extrusion, AZ31 sheet and AM60B die cast double top hat beams under slow four-point bending, slow axial crush and fast (6 m/s) axial crush. Completed testing of these double top hat components for all three materials under all three loading conditions. Determined varying levels of agreement from matching (0% difference) of up to 25% difference between predicted and measured responses.

Task 1.2 Noise, Vibration and Harshness (NVH) – Completed final report of measured transmission loss data for single layer Mg panels and two layer Mg panels with either an air gap or a structural foam interlayer for comparison with single layer steel panels. Provided measured sound insertion loss and sound absorption test data for three generic acoustic treatment packages to international partners to assist with their CAE modeling activities.

Task 1.3 Fatigue and Durability – Completed fatigue tests on Friction Stir Spot Weld (FSSW) of magnesium joints and established preliminary damage model. Commonized fatigue test specimen design and test procedure for magnesium joints and arranged and distributed specimen for ‘round robin’ fatigue testing of FSSW of AZ31 sheet. Obtained fatigue data on AM60 super-vacuum die casting (SVDC) shock towers.

Task 1.4 Corrosion and Surface Treatment – All candidate commercial and experimental pretreatments have now been assessed using one or more methods developed by the task team. The “AC/DC/AC” method for total protection system assessment was developed. Fastener coating evaluation is underway for mitigation of galvanic corrosion with steel fasteners. Intrinsic corrosion measurements on base materials have been completed. First studies of pretreatment durability in advanced paint shops have been completed.

Task 1.5 Extrusion - Fully characterized the tension-compression asymmetry and plastic anisotropy in magnesium alloy extrusions. Developed a flow stress model and adapted DEFORM® 3D for Mg extrusion simulation using porthole dies (seam-weld) and conducted extrusion simulation.

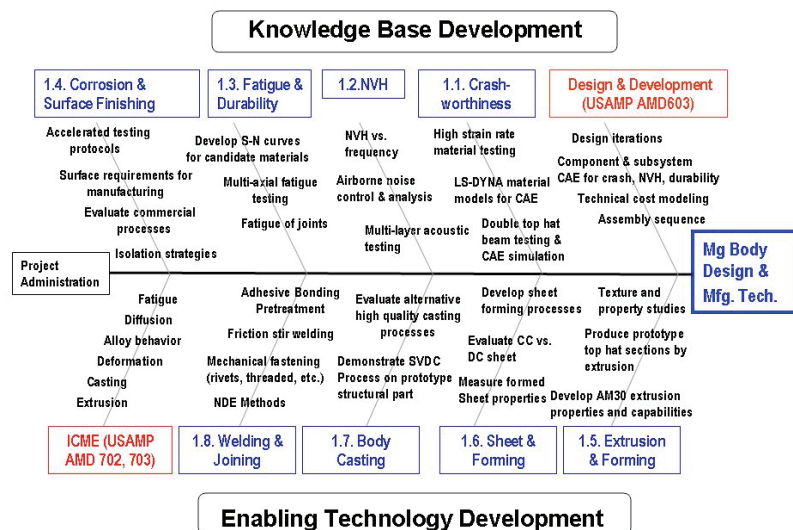
Task 1.6 Sheet Forming – AZ31 sheets representing both DC (direct chill) and CC (continuous cast) processes were obtained from five different sources and showed very similar constitutive behavior, approximating the Sellars-Tegart model. Warm forming windows – i.e. temperature-binder pressure 2D “maps” depicting successful pan forming regimes, were completed for all five materials. Both DC and CC materials showed comparable warm formability. A continuous warm forming process under high volume, run-at-rate conditions was successfully demonstrated as part of the companion USAMP project AMD602.

Task 1.7 High-Integrity Body Castings – Castings of the top-hat design were produced using AZ91 and the “super vacuum die-casting (SVDC)” process, following earlier production of these structures in AM60B for crashworthiness and other studies, thereby completing all casting work planned.

Task 1.8 Joining – Completed screening of 14 pretreatments applied to AZ31 sheet, AM60B casting and AM30 extruded magnesium based on strength, durability and corrosion performance. Completed performance measurements of crash toughened adhesive with 3 selected pretreatments using lap shear, wedge peel and wedge impact tests at various temperatures. Advanced the understanding of Friction Stir Spot Welding (FSSW) and Friction Stir Lap Linear Welding (FSLLW) of AZ31 sheet, AM30 extrusion, and AM60 casting. Produced strong, crack-free joints using self-piercing rivets using local preheating, and completed several fastener application guidelines.

Task 1.9 ICME – (International nomenclature) Reported separately as USAMP project AMD703.

USAMP AMD604 Development Activities



Future Direction

Launch of international MFERD “Phase 2” follow-on project to occur in calendar 2010.

Focus will be on: advanced alloys, durability, corrosion mitigation and joining.

Companion USAMP. Design Project (AMD603) to conclude in 2010 and incorporate findings of this international project for mechanical properties of materials and manufacturing technologies.

Design aspects of the surrogate or “demonstration” structure to be incorporated in the international MFERD “Phase 2” follow-on project instead of a separate OEM only USAMP project.

Next PTC and PSC face-to-face meetings to be conducted in Washington state on March 25, 2010.

Next 3-Country review meeting to be held in Southeast Michigan, October 25-27, 2010.

Introduction

Details of the Magnesium Front-End Research and Development (MFERD) project background and rationale have been included in prior annual reviews and are not repeated here [1]. This document reports achievements of the third and final year of the project, focusing on tasks accomplished through the AMD604 Project of the U.S. Automotive Materials Partnership (USAMP). Accomplishments of the International partners during much of this period are detailed in a separate report [2]. The overarching objectives of the effort are

1. Development of a knowledge base for use in eventual design
2. Realization of enabling manufacturing technologies for magnesium componentry, as may be assembled into durable vehicle substructures.

These broad objectives collectively support design and potential manufacture of magnesium-intensive automotive structures such as the “front end” portrayed in Figure 1. Technical obstacles to the realization of structurally-sound and durable magnesium-intensive assemblies are well known and itemized in USAMP’s “roadmap” document for magnesium technology [3]. The organization of the various project tasks, as detailed in Figure 3, has then supported the overarching technical challenges of the project as a whole.

During FY 2009, substantial progress was made in all task areas, not only in the U.S., but in Canada and China as well, as had been reported at both the international review held at Niagara-on-the-Lake, Ontario in May, and the Canadian annual meeting at the University of Windsor in September. All sample materials of interest have been distributed to the various laboratories and measurements have either been reported or are in progress. Several of the international task teams have convened telephone or web meetings as needed. The “SharePoint®” web site, maintained by Mississippi State University, has been populated with project reports and data.

The project vision, dating back to initial discussions of such an extensive collaborative effort, encompasses both extraordinary opportunities in vehicle design and performance, and concomitantly, a set of “grand” challenges for the scientific and technological underpinnings of the concept. The opportunities arise from the theoretical potential for an approximate 50% (or greater) mass savings as compared to a mild steel baseline for components of comparable stiffness. Such projections are now being realized, at least for the unibody architecture and are reported as part of the companion design project, AMD603. Furthermore, the die-casting process, and its derivatives for magnesium alloys (e.g. “super” vacuum die casting) permit piece-part consolidation and thereby systemic cost reduction. Vehicle-level design targets such as mass redistribution and mass-loss compounding are also realizable. The “grand” challenges derive principally from the fundamental physical metallurgy of magnesium metal and its various

commercial alloys - to wit: a.) highly anisotropic and temperature-dependent mechanical properties fundamentally attributable to its hexagonal close-pack (hcp) crystal structure, and b.) its extraordinarily large electrochemical oxidation potential, rendering it anodic to virtually all other engineering materials to which it is coupled. While scientific and technical approaches to these “grand” challenges exist, principally through alloying, microstructural control, thermomechanical processing and protective surface treatments, it is not clear that any of the scientifically-accepted remedies might become so commonplace as to be readily accepted into the automotive manufacturing environment, where cost, availability and performance are paramount.

Integrated Computational Materials Engineering (ICME) has the potential to address the “grand” challenges from the standpoint of orchestration of the basic physical metallurgy of magnesium and its processing into a less formidable undertaking [4]. The companion ICME projects (AMD702 and 703) seek to take advantage of the ICME approach and worldwide community of practitioners.

The following sections describe key technical attributes of the project and accomplishments occurring during Federal fiscal year (FY) 2009.

2009 Progress and Accomplishments

Task 1.1 - Crashworthiness: This task included material testing, Computer-Aided Engineering (CAE), and testing of beams in bending and axial compression. During 2009, the remainder of the material testing was completed on the five magnesium alloys of interest: AM30 and AZ31 extrusions, AZ31 sheet, AM60B and AM50 die castings. Additionally, the material response data was fit to an available LS-DYNA® material model, MAT_124. AZ31 stamped sheet and AM60B “super” vacuum die cast double top-hat beams were tested in slow four-point bend, slow axial compression and fast axial compression, supplementing the data from the previously-tested AM30 extrusion beams. LS-DYNA® models predicted beam response and included a maximum plastic strain criterion for element deletion to mimic material fracture. The high speed (6 m/s) axial crush test involved local-corner and flat-section buckling, local plastic deformation, high local strains, locally high strain rates, material cracking and separation. The LS-DYNA® predictions matched the tested response to varying degrees. For example, the AM30 extrusion predictions match the peak load and the displacement at the peak load for the four-point bend test within a few percent. However, the AM60B die cast axial crush predictions closely match the peak load in the slow axial compression test but over-predicted the absorbed energy by 25%. All the tested parts all exhibited significant material cracking and fracture as shown in [Figure 4](#).

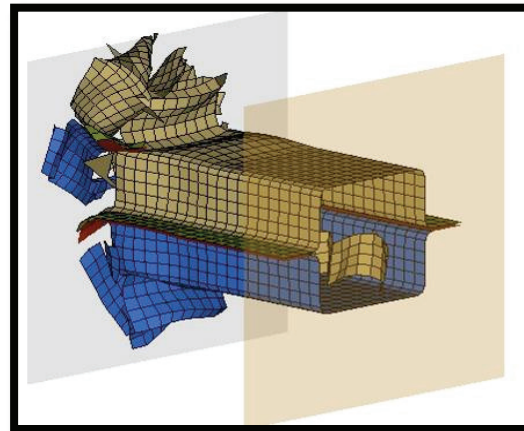


Figure 4. Deformed shape of sheet AZ31 double top hat beam after the high speed sled axial crush test, (a) physical test, (b) FEA prediction.

Future efforts in the Phase 2, follow-on project (AMD904) will refine the failure prediction models for CAE-based predictions.

Task 1.2 – NVH: The U.S. team, through their supplier partner company, IAC North America, provided a final report comparing two-layer Mg panels with either an air-gap or structural-foam interlayer between them to single layer steel panels and provided measured acoustic performance data for three generic acoustic materials to support the CAE modeling activities of the international team partners. A graph of the measured sound insertion loss data is shown in **Figure 5**, where the higher insertion loss of Material No. 2 would appear to offer an advantage over Materials No. 1 and 3 especially at the higher frequencies where a lightweight magnesium dashboard panel would need it the most. It should be noted that this same relationship was not as clear for the measured sound absorption testing (not shown). A schematic representation of Material No. 2 is shown for reference in **Figure 6**.

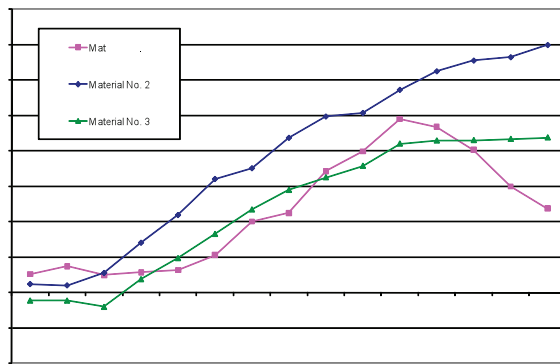


Figure 5. Sound Insertion Loss Data for three unique acoustic treatment packages

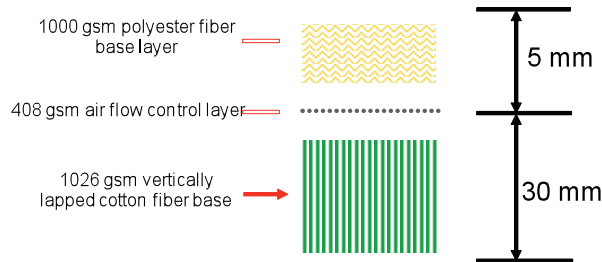
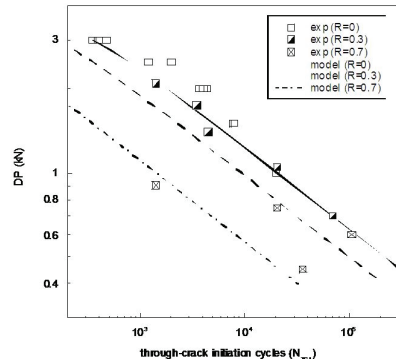


Figure 6. Schematic representation of IAC acoustic treatment package No. 2.

Task 1.3 - Fatigue and Durability: Subtasks for this topic included fatigue tests and modeling of magnesium material and magnesium joints. During 2009, Mississippi State University (MSST) completed fatigue tests of Friction Stir Spot Welded (FSSW) AZ31 sheet and established preliminary damage models as shown in **Figure 7**. Due to the nature of joints and vehicle design, joint fatigue failure is a major durability concern. There are no national or international standards for fatigue tests of joints. In order to standardize joint fatigue tests among labs for the task then, the team agreed upon a specimen design and test procedure which will be used for all future fatigue tests of joints. Specimens have been manufactured according to this design and distributed among five laboratories in Canada, China and United States to start a “round robin” testing of FSSW of AZ31. The fatigue testing of Super Vacuum Die Cast (SVDC) AM60 is also complete and the data was processed for CAE durability analysis.

Figure 7. Test data and model prediction of load range and life cycle of FSSW 2mm AZ31 sheets



Ohio State University. **Figure 8** represents a summary of observations for a variety of commercial and experimental “conversion coat” type pretreatments. Net improvements in the ‘nobility’ of the surface as measured by positive excursion of the metal’s open-circuit potential in the presence of the surface layer, was not as accurate an indicator of resistance to attack by salt fog (ASTM B117) as was the observation of a characteristic ‘knee’ in the anodic portion of the polarization curve.

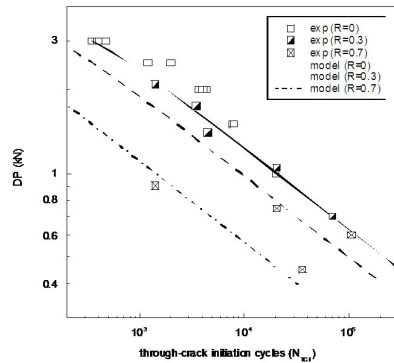


Figure 8. Summary of DC polarization characteristics of conversion coat pretreatments.

A subsidiary array of testing on all pretreatments for use with adhesive bonding was conducted jointly between the University of Michigan (Dearborn) and Ford Research Laboratory as part of Task 1.8 (Joining). This particular set of evaluations permitted both assessments of adhesive bond durability in a corrosive environment as well as relative durability of the pretreatment and polymeric topcoat. For anodizing pretreatments including “micro arc” processes, DC test methods are generally inadequate and impedance spectroscopy is used to compare differing surface treatments and their relative susceptibility to corrosive breakdown. This work was conducted by North Dakota State University. Total coating performance was assessed using a technique developed by Eastern Michigan University combining AC (impedance) and DC (polarization) techniques, and has been reported previously.

Among the more recent measurements conducted was that of “pretreatment durability.” The issue, in this case, is the protection of the magnesium substructure as it may be incorporated in a steel “body-in-white,” with regard to passivation of its surfaces and capability to acquire a protective electrophoretic or “E-coat” as is currently used for steel auto bodies. This aspect has been a particularly troublesome one for magnesium structures in the past, and has typically required magnesium subassemblies to be either entirely encapsulated before traversing the typical paint shop processing, or added to the vehicle body in final assembly. PPG Industries,

as part of its work statement, has now conducted preliminary evaluations of the durability of an advanced pretreatment process for magnesium in the case of “next generation” paint line pretreatments and electrocoats. Results from this very limited study are encouraging.

The fastener coating subteam has now engaged a number of suppliers in providing advanced coatings intended to either isolate steel fasteners from electrical contact to adjacent magnesium, or to acquire a lesser degree of galvanic potential difference due to preferred metallic pigments in the paint layer. This will be a blind test in which a third party laboratory will be engaged to conduct testing of candidate fasteners as well as the individual fastener coating suppliers.

Task 1.5 - Low-Cost Extrusion: The U.S. extrusion team continued to supply extrusion samples of AM30, AZ31 and AZ61 alloys to the appropriate task teams for testing and evaluation. Significant plastic anisotropy is observed in magnesium extrusions, as shown in [Figure 9](#). The yield strength in the transverse direction (55.5 MPa) or 45° direction (58.1 MPa) is only about one third of that in the extrusion direction (176 MPa). While the ultimate tensile strength (UTS) and ductility are less dependent on orientation, the transverse direction shows the highest UTS, but the lowest elongation. It is important to take this level of anisotropy into consideration in designing magnesium extrusions for structural applications. This is largely due to the texture developed in extrusion with the hcp c-axis parallel to the transverse direction. When the sample is subjected to tensile loading along the extrusion direction, the texture is such that twinning is suppressed by slip which requires higher stress to activate, thus, high yield strength. On the other hand, when the c-axis of the hcp magnesium crystals is parallel to the tensile loading, very low stress is required to active extension twinning, thus, lower yield strength in the transverse direction.

Lehigh University has developed a modified Barnett flow stress model for magnesium alloys and adapted DEFORM® 3D for Mg extrusion simulation using porthole dies (seam-weld) and conducted extrusion simulation. The team has successfully implemented a predictive tool for extrusion seam weld using Plata and Piwnik[5] criterion for magnesium alloy porthole extrusion.

The extrusion team has also provided samples and experimental support to the ICME Extrusion task work at Mississippi State University in microstructure-based extrusion simulation.

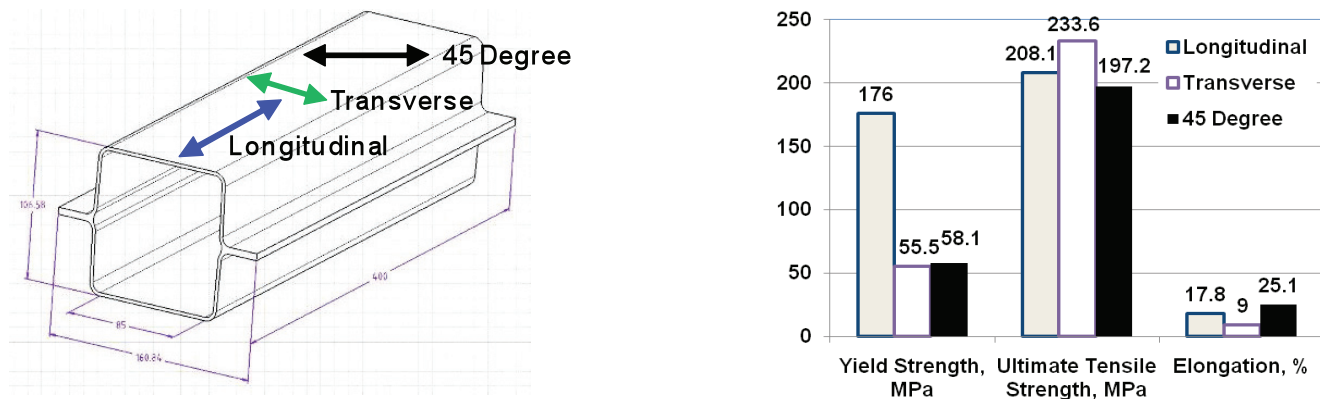


Figure 9. Tensile properties of AM30 hollow rail extrusion in extrusion, transverse and 45° directions.

Task 1.6 - Low-Cost Sheet and Forming: Efforts on low-cost sheet forming of magnesium are incorporated in the separate USAMP project AMD602, and only differentials requisite for the “front end” structure are mentioned here. To date, a variety of commercially available sheet materials of both direct chill (DC) and continuous cast (CC) materials are available and comparative sheet forming results were obtained. The various sheet materials all showed similar deformation behavior, generally capable of constitutive modeling using the Sellars-Tegart equation [6]. Characterization of thicker gage AZ31 sheets (relevant to MFERD) has been completed ([Figure 10](#)).

In “pan” forming (which has been the principal approach of AMD602), binder pressure and temperature play critical roles (Fig. 10). Similar warm-forming windows were completed for all five materials. At temperatures of 300°C and above, all materials behaved similarly and all of them produced pans successfully without cracks or wrinkles. However, at lower temperatures, materials from different sources behaved quite differently.

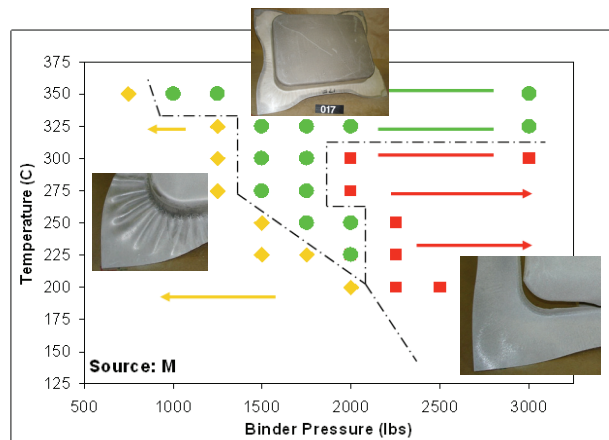


Figure 10. Regime of acceptable forming of the pan structure from AZ31 sheet, in terms of sheet preheat temperature and binder pressure.

The pan die was subsequently integrated into automated warm forming cell, and demonstrated continuous successful pan production at a rate of 5 – 10 jpm (jobs per minute).

Task 1.7 - High-Integrity Body Castings: The companion design project (USAMP AMD603) has shown reliance on large Mg alloy castings that simultaneously achieve both weight reduction and component part integration, contributing to lowering of manufacturing cost. The casting process also permits adjustment of section thickness at various locations in the component, which is generally not achievable in sheet forming processes. The traditional high-pressure die-casting process, presently used to form large structures in magnesium, can suffer from substantial reductions in localized strength and elongation when compared to the maximum theoretical values for the material. These variations are primarily due to incorporation and distribution of porosity resulting from the turbulent nature of the diecasting process itself. Computational methods are expected to play a major role in addressing those physical attributes of the metal flow and solidification leading to improved properties. Vacuum-based processes have also been found to reduce the quantity of entrained gas and permit generally improved metal flows into the die cavity. International efforts are aimed at exploring alternative casting processes (e.g. Thixomolding® (Canada), squeeze casting (China), etc.) as remedies to the challenge at hand. Additionally, heat treatments may afford an opportunity to improve performance of the as-cast structures; however porosity and entrained gases may overwhelm any benefits of heat treatment.

In FY 2009, the casting effort concluded with the delivery of AZ91D top hat castings from Contech, LLC ([Figure 11](#)). Unfortunately, this company has filed for Chapter 11 bankruptcy protection and has exited the Mg die casting business, thereby eliminating the prospects for future exploration of the “super” vacuum die casting (SVDC) process until an alternate supplier can be identified.

Another activity of Task 1.7 was to monitor developments in the USAMP Ultra Large Casting Project (ULC – AMD 406). The ULC project issued its final report in FY 2009 which contained some conclusions relevant to this project; to wit: a.) sub-liquidus casting (SLC) does not appear to be suitable for the manufacture of castings that would have desired mechanical or types of features needed for large, thin-walled automotive castings and b.) Thixomolding® has

the potential to be suitable for the manufacture of large thin-walled castings but would require significant development of multiple hot runner systems and increasing the clamping tonnage of the diecasting machines.

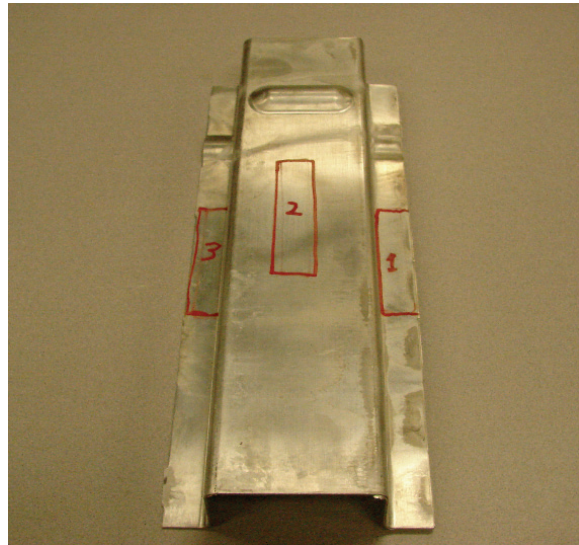


Figure 11. Photo of ‘top-hat’ casting produced by Contech, LLC. Top-hats were produced using both AM60B and AZ91D alloys.

Task 1.8 – Joining: The U.S. Task 1.8 team focused on the following subtasks: a.) adhesive bonding (including pretreatment and degradation), b.) friction-stir welding c.) fasteners (including threaded fasteners, breakstem and self-piercing rivets) and d.) non-destructive evaluation (NDE) of all joint types.

A major achievement in 2009 was the completion of screening tests of fourteen different metal pretreatments available either developmentally or in the marketplace, including several representative treatments from participating organizations in China. The pretreatments were evaluated based on initial load to failure, retained strength after cyclic corrosion testing and general corrosion resistance (see Task 1.4).

Based on these results, pretreatments “A” (baseline), “F” and “G” were subjected to a matrix of performance tests comprised of a crash-toughened adhesive; cast, sheet and extruded magnesium; lap shear, wedge peel and wedge impact tests with -40°C, 20°C, and 80°C exposures. The failure stress or dynamic resistance to cleavage for each material combination

was compared as a function of magnesium type, pretreatment, and exposure. These variations are exemplified by the wedge impact test results shown in Figure 12. Based on these measurements, pretreatments “A” and “F” were recommended for further evaluation in Phase 2, which will include fatigue and corrosion testing with extensive environmental exposure.

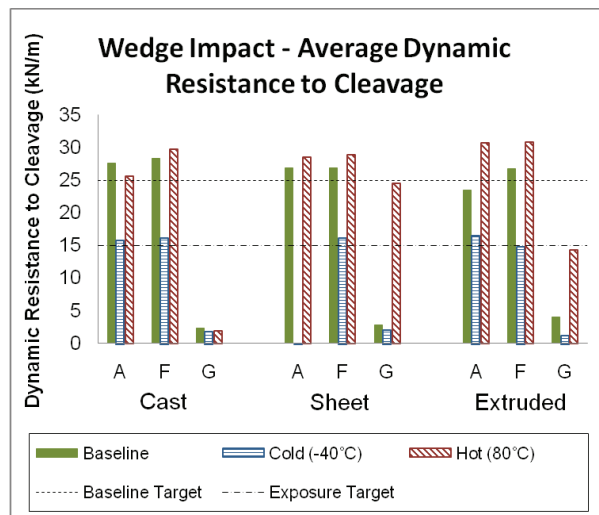


Figure 12. Summary of Task 1.8.3 wedge impact test results demonstrating the variation of dynamic cleavage observed with magnesium type, pretreatment and temperature.

Considerable progress was made in Friction Stir Spot Welding (FSSW) and Friction Stir Lap Linear Welding (FSLLW). FSW and FSLLW have been performed on AZ31-H24 sheet (2.0mm thick), AM30 extrusion (2.5mm thick), and AM60 casting (2.0mm thick) magnesium alloys in various material combinations. Using a cylindrical threaded pin tool and triangular-shaped pin welding tool, the relationships between process condition (including tool rotation speed, and plunge depth, and/or tool travel speed) and lap shear strength of friction stir welds have been developed. The effects of welding tool geometry, welding orientation, and some other factors on weld strength, and the failure mechanisms of friction stir welds have also been investigated. The supplier, Hitachi Ltd. also produced FSSW coupons for round-robin testing by the Fatigue and Durability (Task 1.3) Team.

Significant progress has also been made in fastener technology. Strong, crack-free joints of magnesium have been successfully made using self piercing rivets (SPR) by locally heating of the joint, confirming the viability of such techniques for production of robust joints with magnesium alloys. The process, however requires further optimization especially in reducing preheat time before being suitable for high volume application.

The fastener group also completed selection guidelines for structural breakstem rivets, non-structural breakstem rivets, and plastic non-structural breakstem rivets for use in Mg. They also drafted guidelines for machine threaded bolts and for thread forming screws for use in Mg. They also began investigation of the ability to manufacture magnesium fasteners in conjunction with suppliers U.S. Magnesium and MNP Corporation (fastener supplier).

Conclusions

At the end of its third and final year, AMD 604 has reached the plurality of its initial objectives, insofar as enabling technology development for manufacture of magnesium-intensive structures and knowledge-based understandings of their performance. The international collective has agreed to a second phase project, focused on a surrogate or “demonstration” structure with technical attributes of larger and more costly entire front end assemblies, which are beyond the scope of the effort. Well-known issues of mechanical property limitations of commercially-available magnesium alloys remain a challenge, particularly for such requirements as crashworthiness, and material formability. While success has been achieved for improved casting qualities through “super” vacuum die casting, the mechanical properties still remain below desirable levels to achieve optimum weight reductions in structures. A plethora of corrosion prevention and joining options have been explored through the international partnership, and while there are directional indicators for preferred approaches, there remains much defining work to be done – these efforts being highlighted in Phase 2. Fracture mechanisms, particularly fatigue and environmentally-assisted fracture, while achieving good progress in Phase 1, also remain as technical targets going forward.

The management and organizational structure of the international partnership has been a significant outcome of the project. Networks among engineers and scientists have been established as well as a format and cadence for communication and discussion, which is expected to be further developed in Phase 2.

Presentations/Publications

1. A.A. Luo, J.H. Forsmark, X. Sun, S.O. Shook, W.Z. Misolek, R.K. Mishra, “Microstructure and Mechanical Properties of Magnesium Extrusion Alloys AM30, AZ31 and AZ61”, Magnesium Technology 2010, TMS, Warrendale, PA, 2010.
2. A.A. Luo, J.H. Forsmark, X. Sun, S.O. Shook, “Mechanical and Thermophysical Properties of Magnesium Alloy Extrusions”, SAE Technical Paper 2010-01-0214, Detroit, MI, 2010.

3. D. A. Wagner, S. Logan, K. Wang and T. Skszek, "Test Results and FEA Predictions from Magnesium AM30 Extruded Beams in Bending and Axial Compression," *Magnesium Technology 2009*, ed. A.E. Nyberg, et al.,eds. TMS (The Minerals, Metals & Materials Society, Warrendale, PA), 541-547.
4. K. Lazarz, W. Wang, R. C. McCune, and P. K. Mallick, "Effect of Pretreatments on Adhesive Bonding of Several Magnesium Alloys," , SAE Paper 2009-01-0037 (2009).
5. S. Begum, D.L. Chen, S. Xu and A.A. Luo, "Low-Cycle Fatigue Properties of an Extruded AZ31 Magnesium Alloy", *International Journal of Fatigue*, 2009, 31, 726-735.
6. Z. Brown, A.A. Luo, M. Musser, L.J. Ouimet, K. Sadayappan, J. Zindel, R. Beals, "Development of Super-Vacuum Die Casting Process for Magnesium Alloys", *North American Die Casting Association Transactions*, T09-043, 2009.
7. S. Begum, D.L. Chen, S. Xu and A.A. Luo, "Strain-Controlled Low-Cycle Fatigue Properties of a Newly Developed Extruded Magnesium Alloy", *Metallurgical and Materials Transactions A*, 2008, 39A, 3014-2026.
8. E.A. Nyberg, A.A. Luo, K. Sadayappan and W. Shi, "Magnesium for Future Autos", *Advanced Materials & Processes*, 2008, 166, (10), 35-37.
- 10.S.I. Hill, A.A. Luo, S.Xu and D.A. Wagner, "Dynamic Tension and Compression Properties of Extruded AM30 Magnesium Alloy", published in *Proceedings of the Society for Experimental Mechanics (SEM) Annual Conference*, Albuquerque, NM, USA, June 1-4, 2009.

References

1. A. A. Luo, R. C. McCune, J. A. Carpenter, A. D.Yocum and P. S. Sklad, "Mg Front-End Research and Development (AMD 604)", FY 2008 Progress Report, U.S. DOE, (in press).
2. A Canada-China-USA Collaborative Research and Development Project: "Magnesium Front End Research and Development (MFERD)" 2008 Annual Progress Reports, Project Technical Committee, Alan A. Luo, Eric A. Nyberg, Kumar Sadayappan and Wenfang Shi, Niagara-on-the-Lake, Canada, May 2009.
3. USAMP, "Mg Vision 2020: A North American Automotive Strategic Vision for Mg," Nov. 1, 2006.
4. Integrated Computational Materials Engineering: A Transformational Discipline for Improved Competitiveness and National Security," Committee on Integrated Computational Materials Engineering, National research Council, ISBN: 0-309-12000-4 (2008) <http://www.nap.edu/catalog/12199.htm>
5. M. Plata and J. Piwnik, "Theoretical and experimental analysis of seam weld formation in hot extrusion of aluminum alloys", pp. 205-211, in: *Proceedings of Seventh International Aluminum Extrusion Technology Seminar ET*, Vol. I (2000).
6. C. M. Sellars and W. J. Tegart, "Relationship between strength and structure in deformation at elevated temperature", *Mem. Sci. Rev. Metall.* 63, 731-745 (1967).

Acknowledgments

The success of this project is due to the dedicated efforts of a large number of team members at Chrysler, Ford and General Motors, the various supplier organizations listed below (**Table 1**), as well as the international counterparts in Canada and China. The USAMP core team members, Steve Logan and Mike Heppler of Chrysler; John Allison, David Wagner, Joy Hines Forsmark, Xuming Su, and Jake Zindel of Ford; James Quinn, Dick Osborne, Ravi. Verma, and Theresa Lee of General Motors, are acknowledged for their significant contributions and tireless efforts. The continuing support of our respective organizations and the U.S. Department of Energy is gratefully acknowledged.

University of Dayton Research Institute	North Dakota State University
Troy Tooling Technologies	Luke Engineering & Mfg. Corp.
Cosma Engineering	Technical Applications Group
Contech U.S., LLC	Timminco Corporation
IAC Group North America	Lehigh University
Westmoreland Mech. Testing & Research	Scientific Forming Technologies Corp.
Metokote Corporation	Magnesium Elektron North America
Henkel Corporation	Contech Global, LLC
PPG Corporation	EKK Corporation
Chemetall-Oakite Corporation	.

Kamax LP	INC
Ohio State University	Visteon
Eastern Michigan University	MNP Corp.
University of Michigan - Dearborn	Dow Automotive

Table 1. Supplier Organizations

D. Dynamic Characterization of Spot Welds in Advanced High-Strength Steels

Principal Investigator: Zhili Feng
Oak Ridge National Laboratory
1 Bethel Valley Road; Oak Ridge, TN 37831
(865) 576-3797; e-mail: fengz@ornl.gov

Co-Principal Investigator: Srdjan Simunovic
Oak Ridge National Laboratory
1 Bethel Valley Road; Oak Ridge, TN 37831
(865) 241-3863; e-mail: simunovics@ornl.gov

Technology Area Development Manager: Dr. Carol Schutte
(202) 287-5371; e-mail: carol.schutte@ee.doe.gov

Field Technical Monitor: C David Warren
(865) 574-9693; e-mail: warrencd@ornl.gov

Contractor: Oak Ridge National Laboratory
Contract No.: DE-AC05-00OR22725

Objective

- Develop a new, robust Spot Weld Element (SWE) that can accurately model the deformation and fracture modes of spot welds as a function of impact loading, welding and steel chemistry while maintaining computational efficiency and ease-to-use.
- Develop the implementation procedure to incorporate the SWE in advanced crashworthiness computer aided engineering (CAE) codes used by the automotive crash modelers.
- Generate a companion experimental database on the impact behavior of advanced high-strength steel (AHSS) spot welds under various loading conditions and deformation rates to support and validate the modeling approach.

Approach

- Development of a new spot weld element and associated constitutive models.
- Modeling and characterization of weld microstructure and property.
- Integration of SWE model and weld process and microstructure model.
- Deformation and failure behavior testing under different dynamic loading conditions.

Accomplishments

Successfully completed the Phase I Concept Feasibility development of the SWE modeling framework and demonstrated the effectiveness of such modeling approach in impact simulation of spot welds. Specifically,

- Developed the initial version of SWE

1. Capable of handling weld geometry and weld property gradient;
 2. Capable of predicting different fracture modes and fracture load limit experimentally observed in impact tests.
- Developed the initial version of integrated electrical-thermal-mechanical-metallurgical resistance spot weld model
 1. Capable of predicting weld geometry, microstructure and microhardness distributions;
 2. Friendly user input interface for welding parameters, sheet thickness and steel chemistry.
 - Collected baseline spot weld impact test data on dual phase 780 MPa (DP780) and draw-quality semi-killed (DQSK) steels
 1. Characterization of effects of impact speeds and loading modes;
 2. Web-based database for user-friendly interactive data analysis and retrieval.
 - Completed the comprehensive Phase I project report to Department of Energy (DOE) and Auto-Steel Partnership (A/SP).

Future Direction

- Further expand, and validate the SWE model to cover wide range of AHSS grades and spot weld configurations to demonstrate the applicability of SWE for current generation of AHSS.
- Extend to weldbond for AHSS.
- Extend to other materials and joining processes
 1. Joining of steels to other materials (such as Al alloys, Mg alloys, polymer composites) for multi-material body structure;
 2. Friction bit joining, friction stir joining, and laser welding.
- Failure criteria evaluation and development
 1. Incorporate the effect of heat affected zone (HAZ) softening in ultra high-strength steels and Al alloys;
 2. Develop and evaluate failure criteria including the adhesive bonding.
- Further refine SWE formulation for robustness.

Introduction

A primary driver for increased use of advanced high-strength steels (AHSS) and other high strength materials in auto body structures is the improvement in crash performance while reducing the weight. Resistance spot welding (RSW) is by far the most common joining process used in automotive manufacturing. Typically, there are four to five thousand spot welds in a vehicle. Because the separation of spot welds can affect the crash response of a welded structural component, the dynamic behavior of the spot welds under impact loading of vehicle crash has been one of the critically important considerations in vehicle design and manufacturing.

RSW of AHSS presents unique technical challenges for automotive structure applications. Due to their high carbon and alloying element contents, and tailored microstructure, AHSS

are considerably more sensitive to the thermal cycle of welding than the conventional steels used in auto body structures. Therefore, RSW of AHSS can exhibit very different structural performance characteristics than the ones made of conventional steels. For example, AHSS RSW generally has higher load-bearing capacity, but can fail under different failure modes (button pullout, interfacial, or mixed). The structural performance of AHSS RSW is highly dependent on the grades and types of AHSS. Furthermore, impact experiments on joints and structural components (top-hat and double-hat sections) have shown that RSW have different responses under static and dynamic loads.

In recent years, CAE based simulation of dynamic (impact) behavior of auto body structures during crash has become an indispensable tool that enables rapid and cost-effective design and engineering of crashworthy auto body structures. However, recent impact crash tests revealed that the prediction of spot-weld failure in crashworthiness CAE simulation of auto body structures made of AHSS is generally unsatisfactory. A gap analysis conducted by A/SP concluded that the industry lacks the fundamental understanding and predictive capability for the spot-weld behavior of AHSS and other light-weight materials (such as Al alloys and Mg alloys) during impact loading of vehicles. These gaps hinder rapid and optimum insertion of AHSS and other lightweight materials in auto body structures. The weld failures, detected in later stages of new model car development cycles, have frequently resulted in design compromises that can adversely affect the weight savings available by using AHSS. Furthermore, lightweighting opportunities from optimized use of AHSS and other lightweight materials will not be possible without improved understanding of the phenomena and the development of respective models and CAE tools for crashworthiness analysis.

This program is aimed at developing a new spot weld modeling methodology, supported by experimental data that can be implemented in crash simulation FEA codes used by the automotive crash modelers. The essential feature of this new model includes, through multi-physics simulation of the spot welding process and the resulting microstructural evolution of materials, a novel spot weld element (SWE) approach capable of handling various deformation and fracture modes, the effects of microstructural and strength variations in spot welds of AHSS and other lightweight materials, and the deformation rates and loading modes encountered in vehicle crash.

A three-prong approach has been adopted in the development of the new spot weld modeling approach:

- A integrated electrical-thermal-mechanical-metallurgical resistance spot weld *process model* to generate the weld geometry, microstructure and residual stress results needed by SWE,
- A new spot weld element (SWE) and associated constitutive models for its robustness in crashworthiness CAE simulation, and with the complexity to incorporate weld geometry and microstructure effects, and
- A companion weld characterization and impact test database for development and validation of the new spot weld modeling approach.

In recognizing the complexity and the scope of efforts required to develop and mature this new modeling methodology for the wide variety of AHSS currently used in auto-body structures, as well as the use of AHSS and other lightweight materials in future multi-material vehicles, this project was divided into two phases. Phase I was an initial concept feasibility effort to develop and demonstrate the feasibility and potential of the SWE modeling approach for an initial set of steels, weld configurations, and impact testing conditions. Phase II is a comprehensive Technical Feasibility R&D which will cover a wide range of materials, thickness ranges, weld configurations and microstructures, to refine, improve, mature, validate and demonstrate the SWE methodology for eventual implementation in CAE by the industry users.

The project has successfully completed the Phase I development and has achieved the technical goals for Phase I set forth by the A/SP, which co-sponsored the work. The successful Phase I development has attracted strong support from the original equipment manufacturers (OEMs) and steel suppliers. The integrated weld process model has been licensed and transferred to industry. The SWE formulation and the Phase I results have been adopted and further refined by the OEMs and industry consortia.

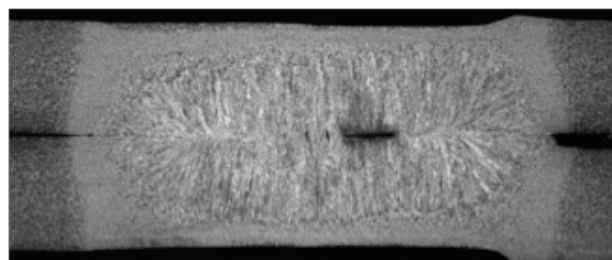
This report highlights the key developments accomplished in Phase I of the project. A comprehensive Phase I Technical Report is available that details the approaches and findings of the Phase I work.

Materials, Welding and Testing

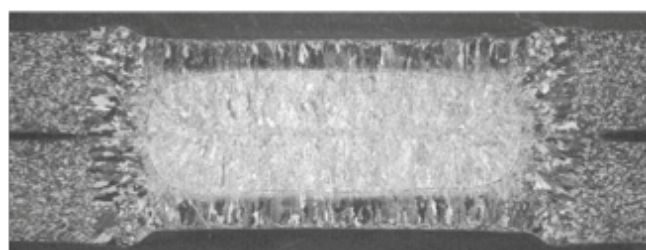
Two steels, dual-phase AHSS DP780 steel (1.15-mm thick) and DQSK mild steel (1.0-mm thick), were selected for the initial development in Phase I. DP780 was galvaneal-coated, and DQSK was hot-dip galvanized. These steels were selected and provided by the A/SP Strain Rate Characterization Committee.

For each of the steels, the welding schedule was varied to produce three different weld nugget sizes acceptable to the industry specification to study the effects of weld size on the fracture behavior of spot welds in impact testing. The welds in Phase I were made in a two-thickness (2-T) stack-up of the same steel of the same thickness.

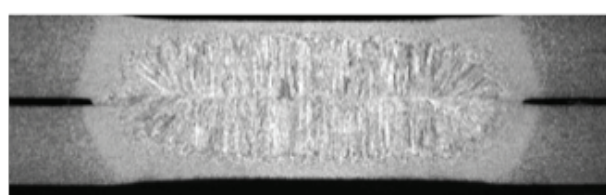
Detailed microstructural analyses were performed to characterize the microstructure and microhardness gradients, as well as the weld defects (if any), in the weld and heat-affected zone (HAZ) of the spot welds. The microstructure and microhardness results were used to validate the weld process model for RSW. **Figure 1** shows the appearance of the welds produced under different welding conditions.



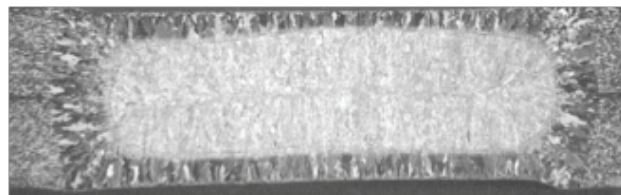
DP780 minimum nugget size



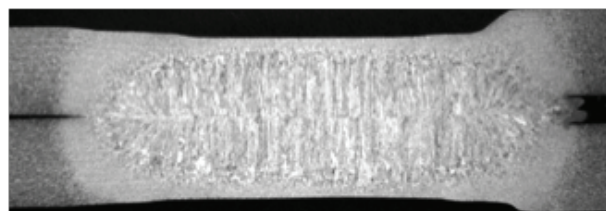
DQSK minimum nugget size



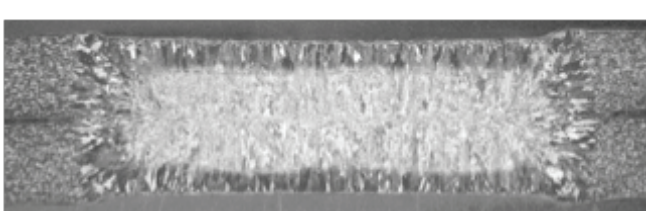
DP780 medium nugget size



DQSK medium nugget size



DP780 maximum nugget size



DQSK maximum nugget size

Figure 1. Weld nugget appearance of DP780 and DQSK welds.

Both dynamic and static testing of the spot welds, in lap-shear, cross-tension, and mixed torsion/tension loading configurations, were performed at four loading velocities: quasi-static, 2.6 m/s (5.8 mph), 3.6 m/s (8.1 mph), and 5.8 m/s (12.5 mph). The tests were carried out at University of South Carolina. A drop tower impact test machine was used for the impact tests. The fracture modes and peak loads to failure of all spot welds were analyzed. A web-based project portal and database were developed that allowed the industry members to access the project results. Dependency of the spot weld failure mode and peak load on weld size, loading mode, and loading rate were observed.

These data were used to validate the SWE modeling approach. Selected testing results are provided in **Figure 2**.

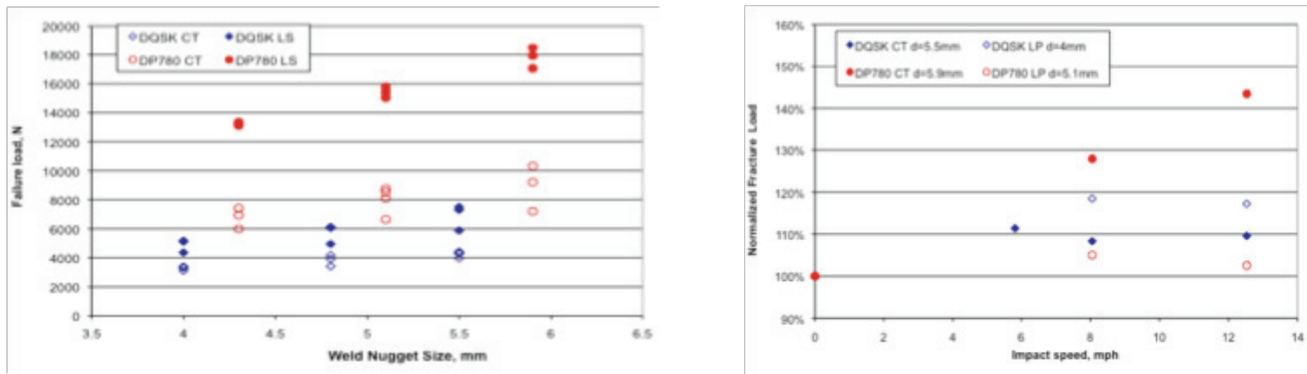


Figure 2. Effect of weld nugget size and impact speed on the fracture strength of spot welds. CT: cross-tension load, LS: lap-shear load. The fracture strength under different impact speed is normalized to the static strength of the same weld condition.

Integrated RSW Process Model

The SWE requires detailed microstructure and property information in the weld region to properly formulate the constitutive equations. An integrated electrical-thermal-mechanical-metallurgical welding process model for electric resistance spot welding was used in this project, to predict the microstructure and property gradient in the spot weld and the adjacent region. It is based on the early work with further refinement of the microstructural model for AHSS.

The integrated electrical-thermal-mechanical-metallurgical RSW process model predicts the weld size, microstructure and residual stresses in a spot weld based on the following user inputs:

- Steel chemistries and base metal microstructure
- Surface coating
- Sheet stack-ups
- Welding conditions (current and electrode force)
- Electrode geometry

A key feature of this integrated weld process model is that it predicts the microstructure evolution based on the calculations of the thermodynamics and kinetics of steel phase transformation processes. There is no need to experimentally measure the continuous cooling transformation (CCT) curves for given steel, an impossible task for all possible thermal cycles experienced in different locations of the weld and HAZ of a spot weld.

The integrated RSW process model was applied to the two steels and different welding conditions in Phase I. The simulation results compared well with the measurement results

of weld microstructure and microhardness distributions. Figure 3 shows the predicted weld nugget, volume fraction of different phases, and the resultant microhardness distributions in a DQSK spot weld. The weld nugget region exhibits a complex distribution of martensite, bainite and ferrite. The comparison of microhardness distribution of both DQSK and DP780 steels are presented in Figure 4. For each steel, the prediction is in the top contour plot, whereas the measurement results are given in the middle contour plot and also the bottom line plot along the middle thickness of the steel sheet.

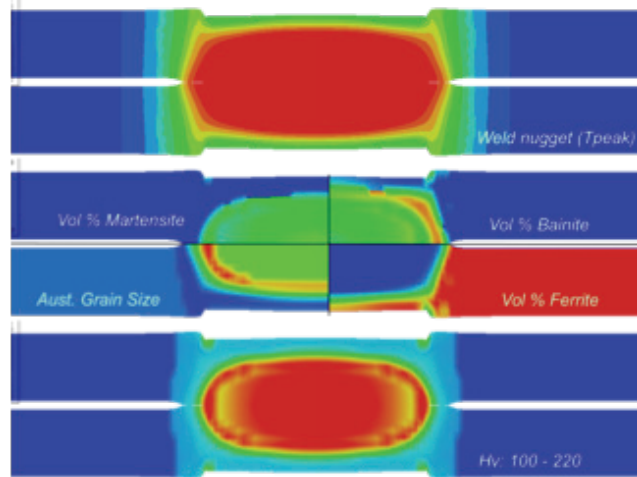
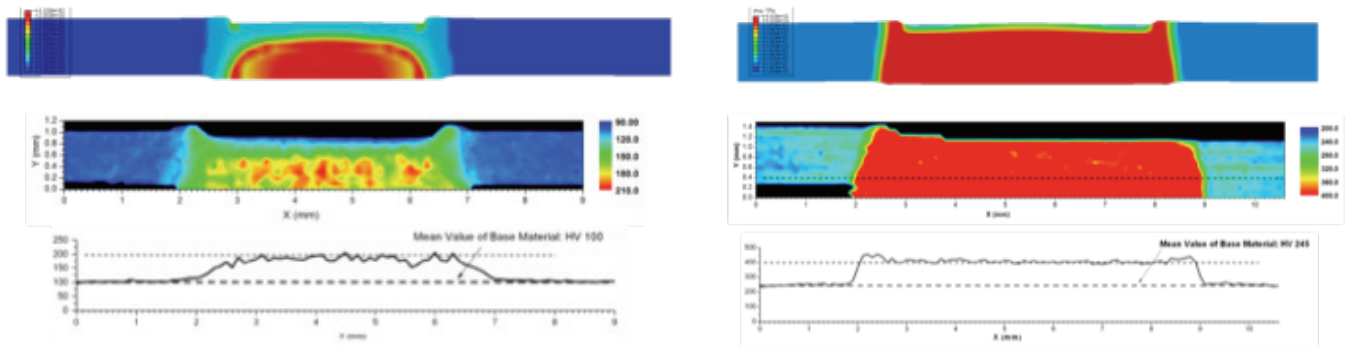


Figure 3. Predicted weld nugget as represented by the peak temperature in red color (top), volume fractions of different phases (middle), and microhardness distribution (bottom) in a DQSK spot weld.



(a)

(b)

Figure 4. Microhardness distribution. (a) DQSK, (b) DF780.

Development of Spot Weld Element

Spot welds in finite-element modeling (FEM) impact simulations are usually modeled with two sub-models; a kinematics model of the joint and the associated constitutive model describing the material-related response of the joint. Currently, the kinematics of the joint is primarily modeled as point-to-point connection by means of flexible or rigid (i.e. constrained) line finite elements. The line connection restricts the constitutive spot weld models to force-based laws. This in turn requires extensive experiments to determine the model parameters for different RSW configurations (nugget size or steel chemistry, for example). One of the principal problems with beam-based kinematics models in AHSS spot welds is that the stress and strain distributions in the weld area are not accurately represented. For RSW in conventional steel structures, the

dominant failure mode is the button pullout and the inadequate calculation of the shear stress may not be a major concern in impact simulation of vehicles. However, for AHSS RSW, accurate determination of the shear stress may be critical because of the occurrence of the interfacial failure or mixed interfacial plus pullout failure mode. In addition, the multiple failure modes and the changes in failure modes under different loading conditions require development of more versatile failure criteria based on the fracture and damage mechanics principles than the resultant force-based ones. From the structural stiffness perspective, the bar and beam models typically yield acceptable accuracy under tension, out-of-plane torsion and bending loads. For in-plane torsion and shear, the stiffness values are highly inaccurate. The brittle fracture associated with the interfacial failure of the spot weld is more likely during impact where plastic deformation of the base material may be constrained by large elastic stress field. Compared to a gradual increase in hardness in the HAZ in mild steel RSWs, the AHSS exhibit sharp hardness change that adds to brittleness and notch sensitivity of the joint.

The SWE formulation developed in this project allows for more accurate representation of the stress distribution in the weld zone that is computationally feasible for crash simulations. The recent RSW models based on solid elements inserted between shell elements of the sheet material have shown much better accuracy than the line-based elements. We have extended that approach to the model configurations illustrated below in [Figure 5](#). The schemes depict through-thickness direction of the spot weld.

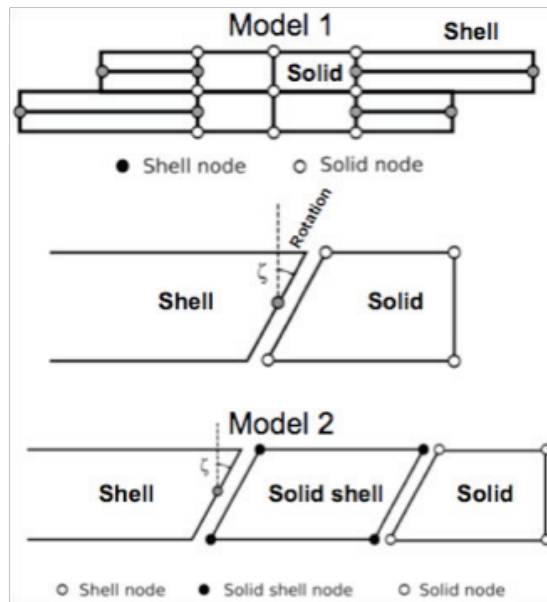


[Figure 5](#). Configuration of the spot weld model in the through-thickness direction. Model 1 has shell elements in the HAZ and the plate whereas Model 2 used 8-node solid shell for the HAZ. The middle figure shows the coupling between the 4-node shell and solid.

The models have compatible connection between the plate (shell) and the nugget (solid) regions. The principal difficulty is the element meshing of the region, but with the current computational design tools such connections should be easily manageable. Additional simplification of the connection comes from the fact that the inner region of the spot weld is relatively stress free compared to its periphery. Accordingly, the inner region of the weld can be replaced by computationally inexpensive rigid elements, or equivalently, kinematic constraints. The constraints computationally stabilize the solid elements in the deformable region of the spot weld and provide additional mass that can be used for computational speed-up of the region using mass time scaling.

Possible failure regions in the new spot weld connection are shown in [Figure 6](#). The stress-strain values in those regions can be used to evaluate various fracture criteria that would initiate failure of the spot weld. In Phase I, a simple failure criterion based on equivalent strain to failure

was used. The material properties in the weld region were based on the hardness measurements and simulations. Base material properties were scaled with the simulated/measured hardness coefficient and equivalent strain to failure was reduced accordingly. This constitutes a very simplistic model that will need to be refined by more accurate criteria in the future.

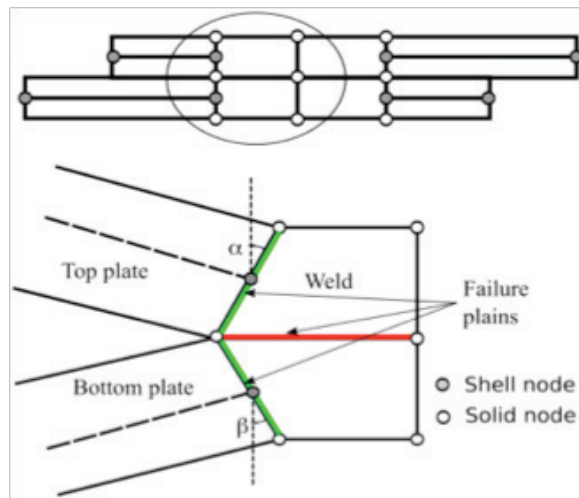


Figure 6. Failure zones in the spot weld model.

Lap-Shear Specimen Simulations

The standard lap-shear specimen geometry was simulated, with detailed FEM discretization shown in Figure 7. Figure 8 shows the simulation side view of the spot weld region of the lap-shear test with small nugget diameter. The figure shows configurations before and after the failure. The failure of the spot weld in simulation and experiments was along the interface between the two connected sheets.

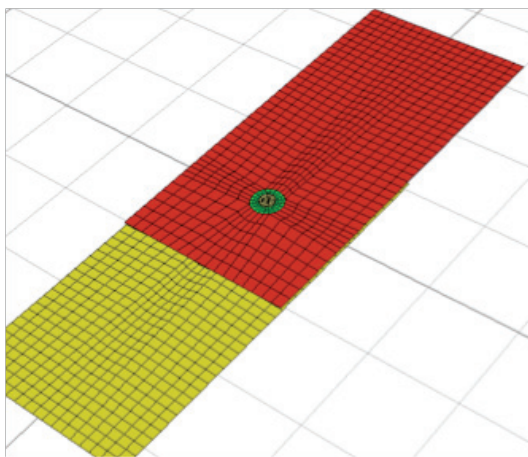
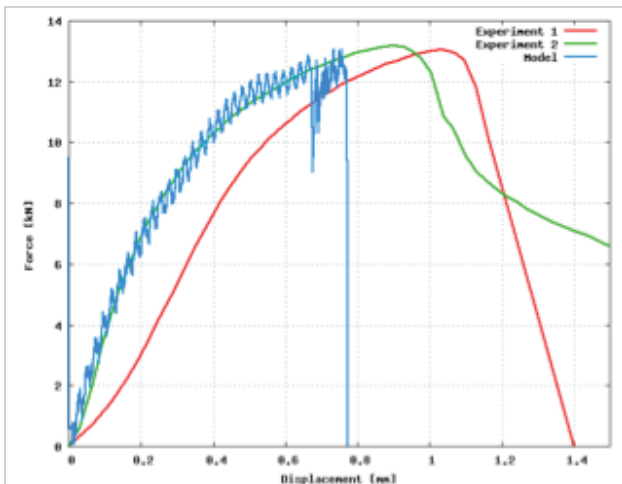


Figure 7. Lap-shear specimen model. Detailed FEM mesh.



Figure 8. Lap shear test simulation for small spot weld nugget diameter (4.3 mm). DP780 steel.

Comparison of the force-displacement data from simulation and the quasi-static test is shown in [Figure 9](#). The resulting force comparison is very close given the experimental scatter and the simplicity of the failure model. The simulation for large spot weld diameter in lap shear test is shown in [Figure 10](#). The simulation in [Figure 11](#) is again reasonably close to the experimentally measured force and stiffness of the assembly.



[Figure 9](#). Comparison of the resulting force for experiments and simulations for DP780 steel, small spot weld diameter (4.3 mm).



[Figure 10](#). Lap shear test simulation for large spot weld diameter (5.9 mm).

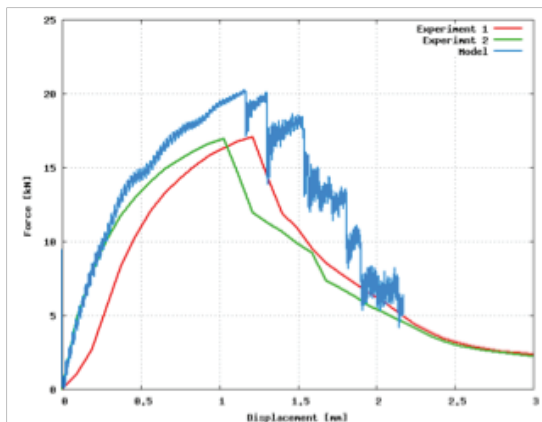


[Figure 11](#). Comparison of the resulting force for experiments and simulations for DP780 steel, large spot weld diameter (5.9 mm).

The spot weld model accurately recovers geometry effect based on intrinsic material properties and a very simple failure condition, without a need for accounting of any extrinsic joint properties such as nugget diameter.

Cross-Tension simulations

Model geometry configuration for the cross-tension test is shown in [Figure 12](#). The clamped boundary conditions are imposed on the nodes emerging from the fixture.

Simulation of the cross-tension test of DP780 steel with large nugget diameter ($D=5.9$ mm) is shown in Figure 13.

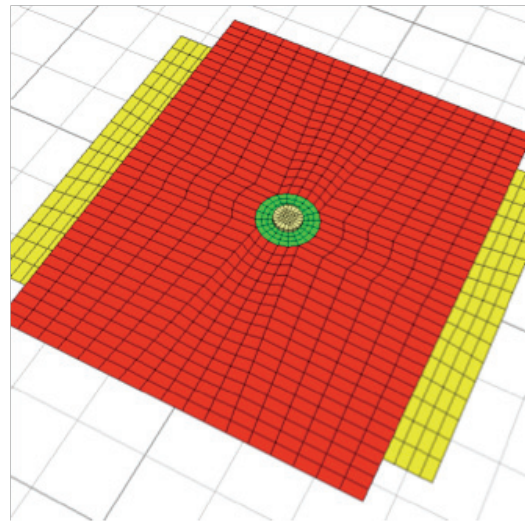


Figure 12. Geometry configuration of the cross-tension specimen. Detailed FEM discretization.

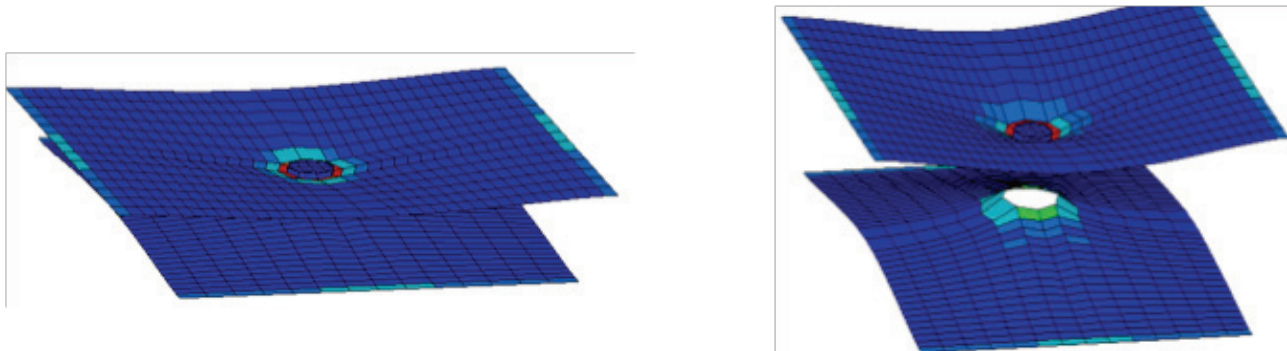


Figure 13. Cross-tension specimen deformation before and after the joint failure. DP780 steel, large spot weld diameter (5.9 mm).

When the model is compared with impact experiments, Figure 14, a relatively large scatter of the results can be noted. The origin of this disparity may be in incomplete clamping in experiments, as the post-test specimen analysis showed traces of slipping in the clamps.

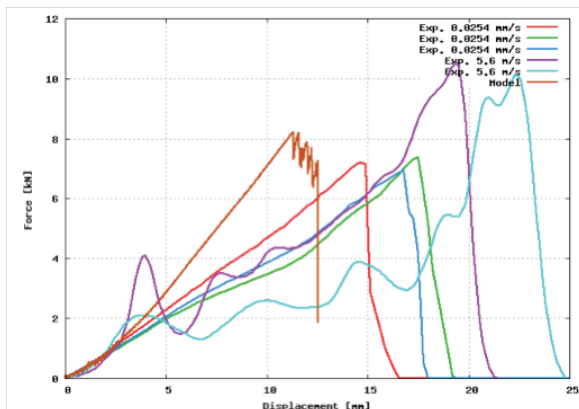


Figure 14. Comparison of the model with experiments for quasi-static and impact tests. DP780 steel, large spot weld diameter (5.9mm).

The origin of stiffer behavior may also be in the size of the shell elements in the HAZ zone. The elements in that zone are responsible for the overall failure. The actual strain localization zone is very small and we need to scale the plastic strain to failure with respect to the size of the finite elements in order to conserve the energy to failure. Normalization procedures and viscous regularization based on strain rate effects can be employed for this purpose. Overall, maximum force in the simulation corresponds very well to the tests.

Conclusions

Phase I (concept feasibility) of the project successfully carried out the initial development of the Spot Weld Element (SWE) modeling framework and demonstration of the effectiveness of such a modeling approach. Specifically,

- The initial version of SWE has been developed with the following capabilities:
 1. Capable of handling weld geometry and weld property gradient, and
 2. Capable of predicting different fracture modes and fracture load limit experimentally observed in impact tests.
- The initial version of integrated electrical-thermal-mechanical-metallurgical resistance spot weld model has been developed with the following capabilities:
 1. Capable of predicting weld geometry, microstructure and microhardness distributions, and
 2. Friendly user input interface for welding parameters, sheet thickness and steel chemistry.
- Baseline spot weld impact test data on DP780 and DQSK steels have been collected and analyzed to characterize the effects of impact speeds and loading modes, and
- A web-based database has been set-up for user-friendly interactive data analysis and retrieval.

Acknowledgement

The authors acknowledge with gratitude the technical guidance of the Auto/Steel Partnership Strain Rate Characterization Project Team, especially of the technical contributions of the following members: Dr. Kathy Wang (Chair, General Motors), Dr. Dave Muelemen (past Chair, General Motors), Omar Farugue (Ford), Tau Tyan (Ford), J. Z. Cao (Chrysler), Ilaria Accorsi (Chrysler), Vinod Makam (Chrysler), Ming Chen (U.S. Steel), Min Kou (ArcelorMittal), Raj Mohan Iyengar (Severstal N.A.) and Pat Villano (Auto/Steel Partnership). Experimental data were provided by Dr. Y.J. (Bill) Chao and Y. Kim of University of South Carolina under a companion project sponsored by the Auto/Steel Partnership.

Presentations/Publications/Patents

Feng, Z., Simunovic, S. Chao. B, Wang, K., Belwafa, J. and Chen, M.; "Impact Modeling and Characterization of Spot Welds," International Auto Body Congress (IABC) 2009, Nov 4-5, 2009, Troy, MI.

E. High Rate Damage and Fracture, Experimentation, Simulation and Visualization in the Southern Regional Center for Lightweight Innovative Designs (SRCLID)

Principal Investigator: Philip Gullett
Assistant Professor, Civil and Environmental Engineering
Mississippi State University (MSST)
Walker Bldg., Rm 235 M
Mississippi State, MS 39762
(662) 325-5486; e-mail: pmgullett@engr.msstate.edu

Participants: M.F. Horstemeyer, M. Tucker, D. Ward, T.N. Williams, and S. Simunovic (ORNL)

Technology Area Development Manager: Dr. Carol Schutte
(202) 287-5371; e-mail: carol.schutte@ee.doe.gov

Project Manager: Magda Rivera
e-mail: magda.rivera@netl.doe.gov

Contractor: Mississippi State University
Contract No.: DE-FC-26-06NT42755

Objective

- Evaluate the strain rate failure of AZ31 magnesium (Mg) for various stress states.
- Develop a damage model for stress-state dependence of dynamic damage evolution.
- Evaluate numerical procedures for the modeling of monotonic fracture of Mg.

Approach

- Characterize material behavior using Split Hopkinson Bar experiments in compression, tension, and torsion.
- Characterize damage nucleation using molecular dynamics.
- Develop damage evolution based fracture criteria.

Accomplishments

- Examined anisotropic, high strain-rate compression, and associated metallurgical evaluation of Mg AZ31.
- Evaluated the effects of grain orientation and stress states on void nucleation at triple junctions in Al using molecular dynamics.
- Implemented the MSST material model into a fracture simulation code.

Future Direction

- High strain-rate testing of Mg AM60, AZ91 control arm specimens
- Implementation of microstructure-property damage-based fracture criteria in fracture-simulation code.

Introduction

This report summarizes the state of the experimental and numerical simulation study of failure mechanisms in AZ31 Mg. The aim is an enhanced, multiscale microstructure-property model that can be implemented into commercial codes and that can be used in high-fidelity crash simulations for the design and optimization of structural Mg components. The development effort will focus on the AZ31 Mg alloy, and a complementary experimental effort will provide experimental data for other Mg alloys that can be utilized for the development of microstructure-property model parameters.

One of the design aspects integral to the development of highly fuel-efficient vehicles is the reduction of overall vehicle weight. Mg has become a central focus in this effort due to its high strength-to-weight ratio, castability, machinability, and damping. On a component basis, Mg can potentially result in 30 to 75% weight savings over conventional iron-, steel-, aluminum-, and plastic-based designs (Osborn (2005)).

The mechanical performance of structural components under service loads is well understood, as component design is based on well-established principles of linear elastic solid mechanics. Under safety-critical, extreme loading conditions such as crash, the mechanical behavior depends on a complex relationship between component geometry, loading, and material microstructure. In particular, component failure is controlled by microstructural (or smaller scale) phenomena that vary according to deformation history, temperature, strain rate, and stress state.

The DOE and the United States Council for Automotive Research's (USCAR's) United States Automotive Materials Partnership (USAMP) funded the Structural Cast Magnesium Development (SCMD) project, a broad, multi-faceted effort to address concerns related to the use of structural Mg. One outcome of the SCMD project was the effort led by Horstemeyer et al. (Horstemeyer, Oglesby et al. (2007)) to develop a microstructure-property model that included microstructural details that act as the source of damage progression. Horstemeyer's work included detailed multiscale analysis and model development for several Mg alloys targeted for application in structural automotive components.

This current effort attempts to build on the experimental and computational work of Horstemeyer et al. (Horstemeyer, Oglesby et al. (2007)) by extending the investigation of dynamic failure mechanisms and energy-absorption characteristics of Mg through experiment and simulation, as well as provide experimental data for additional Mg alloys.

Anisotropic effects on the strain rate dependence of magnesium alloy AZ31B

To fully quantify the effect of the loading orientation and strain rate on the stress-strain behavior of AZ31B, compression tests at quasi-static and high strain rates were performed in all three directions as indicated by [Figure 1](#). All of the specimens were tested to fracture. The specimens were obtained from an as-received 19.05 mm thick plate in the H24 condition. Tests under quasi-static conditions were performed using an Instron 5882 electromechanical machine under constant strain rate controlled at 0.001/s. The high strain rate tests were conducted using a

maraging steel Split Hopkinson Pressure Bar (SHPB) apparatus. The analysis of the high strain rate data was conducted using the DAVID software package (Gary (2005)).

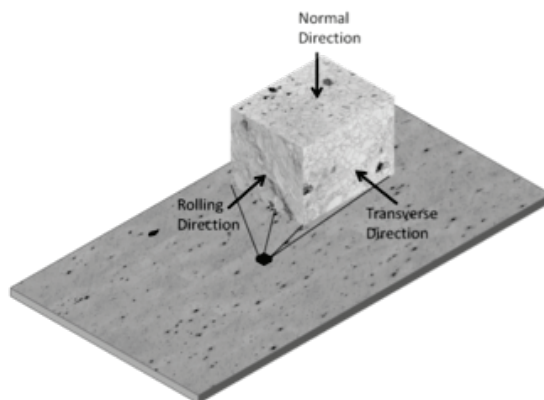


Figure 1. Orientations of testing and microstructural analysis relative to the as-received AZ31B plate.

Figure 2 shows the results of tests performed at quasi-static ($10^{-3}/\text{s}$) and high strain rates ($3400/\text{s} - 4300/\text{s}$). When tested in the normal or short transverse direction, a strong rate dependence on the yield strength was evident. The initial hardening rate at high strain rate was similar to that at quasi-static rates, but the high strain rate specimen began to exhibit softening at a strain of approximately 0.08 that continued until the specimen fractured at a strain of approximately 0.18. This constituted a significant increase in the strain-to-failure compared to the quasi-static conditions and is likely due to either thermal softening or the onset of dynamic recrystallization during the adiabatic conditions of the high rate test.

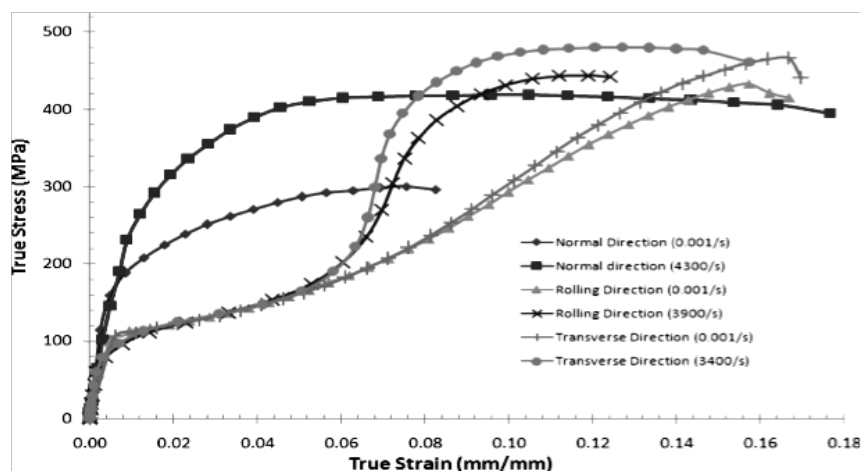


Figure 2. Compressive stress-strain behavior of AZ31B-H24 showing the anisotropic effects on the strain rate dependence.

The total energy absorbed during deformation is an important factor under impact conditions. As Figure 3 illustrates, the AZ31B experimental results show that as the applied strain rate increased, the energy absorption increased in the normal direction but remained the same in the rolling and transverse directions.

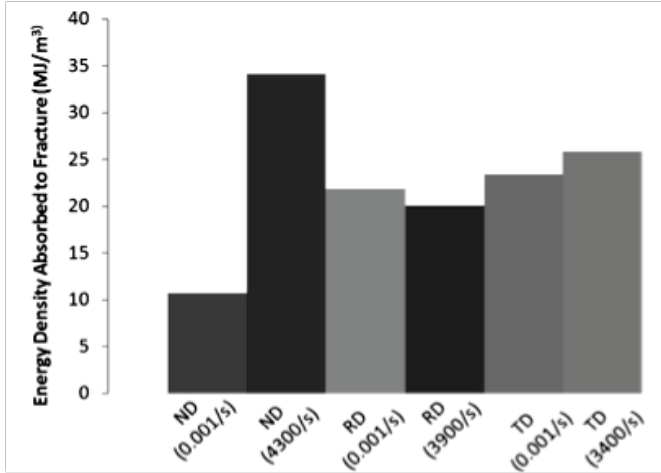


Figure 3. Energy density absorbed (energy absorbed per unit volume) to fracture as a function of orientation (ND=normal direction, TD=transverse direction, RD=rolling direction) and strain rate showing strong strain rate effect in the normal direction, and insignificant effect in the rolling and transverse directions.

Void nucleation at triple junctions in Al: An atomistic study

Understanding material failure is critical for improving the performance and safety of mechanical components. Ductile failure occurs due to several factors, including accumulation of damage (Garrison and Moody (1987)). Damage is primarily associated with the nucleation of microcracks, growth of cracks and voids, and coalescence of cracks/microvoids as a material is deformed (Rice and Tracey (1969); Gurson (1977); Tvergaard (1982); Hirth and Nix (1985); Tvergaard and Van Der Giessen (1991); Lubarda and Krajcinovic (1993); Van der Giessen, Van der Burg et al. (1995); Horstemeyer and Gokhale (1999); Horstemeyer, Lathrop et al. (2000)), including damage in continuum models for modeling the failure of parts requires a physical understanding of the nucleation of defects. For example, microstructure influences void nucleation at the micro-level (Querin (2005); Querin, Schneider et al. (2007)). The microstructure contains many defects that lead to void nucleation, such as triple junctions. The meeting point of three grains in polycrystalline materials, also referred to as a triple junction, introduces stress concentrations and discontinuities in the microstructure (see Figure 4). Our study examines the conditions necessary for void nucleation of an atomic level triple junction.

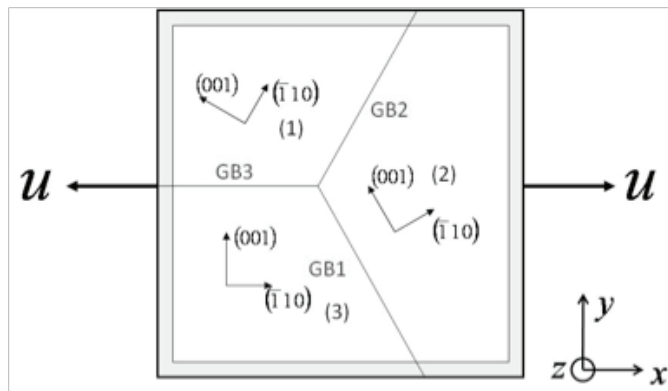


Figure 4. Schematic of initial grain structure for a simulation with a (110) texture under uniaxial straining. The grey region represents the fixed atoms for maintaining a square structure.

To elucidate the nucleation of voids at triple junctions, MD simulation results are shown in this writing over a range of configurations of isolated Al triple junctions. We will focus on two main features: the stress state and the triple junction microstructure.

Void nucleation ranged from $E_e=4.8\text{-}13.0\%$ and $\sigma_{vm}=2.5\text{-}3.4$ GPa (see Figure 5). Interestingly, void nucleation did not necessarily occur at the maximum stress but occurred generally near the peak stress of the global stress-strain curve. Each simulation had a different location of void

nucleation but always on a grain boundary. Further, the voids never nucleated more than 10 nm away from the center of the triple junction. This was an expected outcome since the triple junction acts as a stress concentrator.

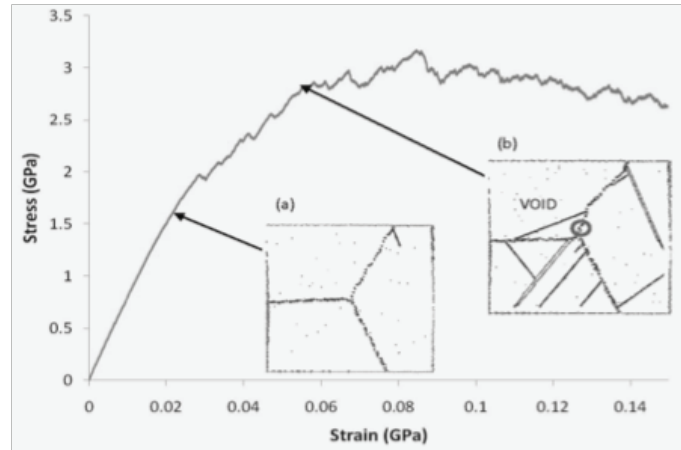


Figure 5. Stress-strain behavior for the 0° , 15° , 30° high angle grain boundary simulations. The response was elastic up to the first dislocation nucleation at (a) and the first void nucleated at (b). The insets show the atomic positions of the atoms with centrosymmetry [54] values over 4.0, or non-FCC atoms, at points (a) and (b).

Biaxially straining compared the effects of having a different stress state. **Figure 6** shows the Von Mises stress versus effective strain. Clearly, just from the strain at which the stress-strain deviates from linearity the uniaxial and biaxial response had differences. The nonlinear response of the uniaxial straining suggested a significant amount of plasticity relative to the biaxial straining. Comparing the insets of Figure 5 and Figure 6 show just how little dislocation activity the biaxial straining had relative to uniaxial straining just before void nucleation. For the case of biaxial straining, the slip-planes had no resolved shear stress, while, in uniaxial straining, the stress induces a shear on the slip planes driving nucleation. The responses for all of the other biaxial simulations exhibited a linear increase in Von Mises stress to a peak followed by catastrophic failure. The peak Von Mises stresses range from 2.7-4.1 GPa at effective strains to failure of 6.4-7.4%. The effect of increasing the stress triaxiality decreases the strain-to-failure. The next section further discusses the effect of triaxiality.

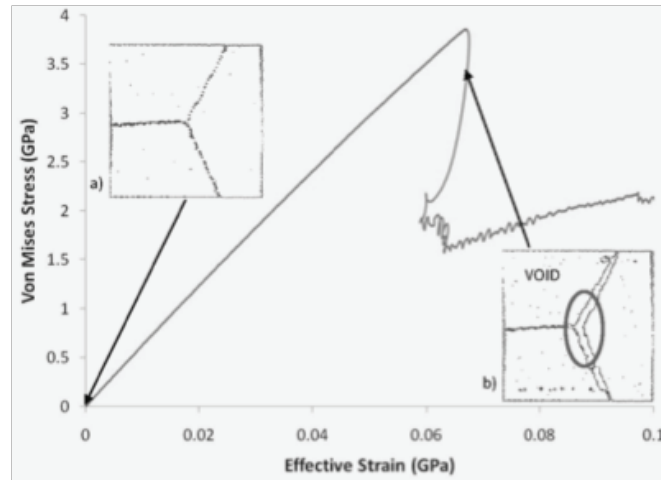


Figure 6. Von Mises stress-effective strain behavior for the biaxially strained 0° , 15° , 30° simulation. Inset a) and b) show the non-FCC atoms [54] just after relaxation and void nucleation, respectively.

Macroscale Fracture & Modeling

Ductile fracture initiates from a critical state of void nucleation growth and coalescence. Modeling of localization requires introduction of a length scale to make energy dissipation well defined. The approach taken here utilizes a finite-element framework (Rashid (1997); Rashid (1998)) capable of incorporating material-specific ductile fracture mechanisms into the failure model and that is independent of mesh topology.

Figure 7 shows an example simulation of fracture of a magnesium alloy AM60 specimen under tensile loading. The initial set-up and of a crack tip patch are shown. The patch moves with the crack tip and allows the predicted path to follow a mesh independant trajectory.

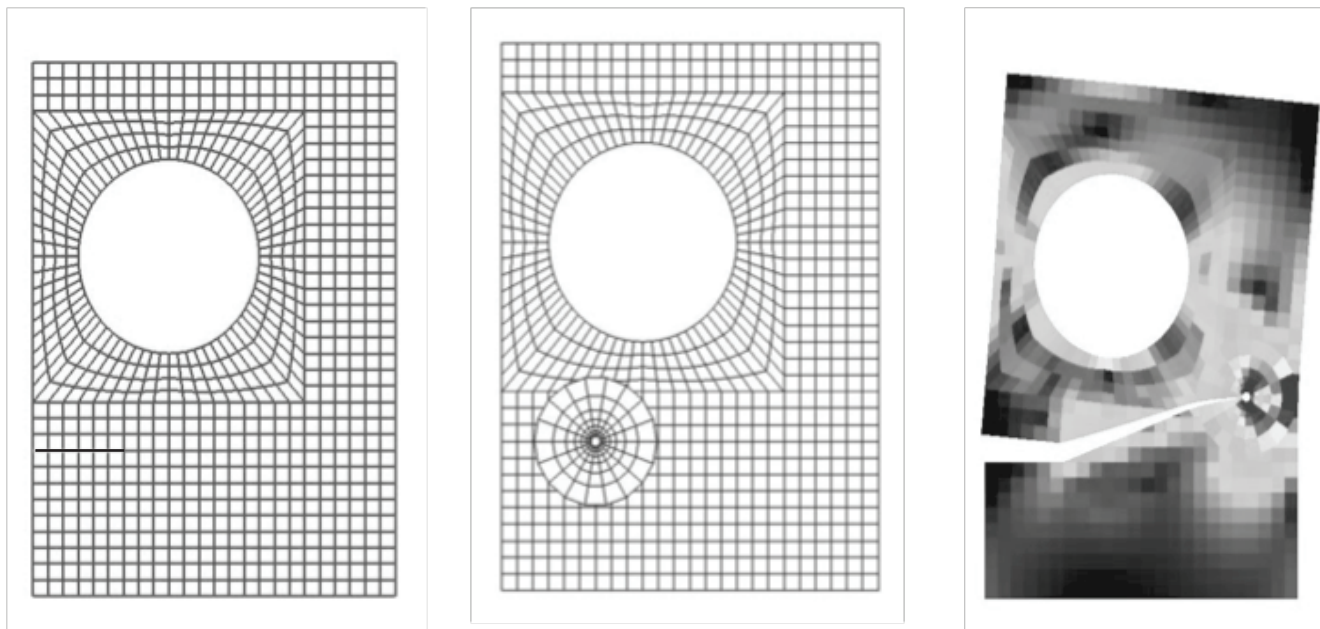


Figure 7. The dark line in the specimen on the left is the initial. The middle image shows the patch mesh at the crack tip. The right image shows the predicted, mesh independant path.

The Mississippi State University Microstructure-Property Model (Bammann, Chiesa et al. (1993); Horstemeyer (1995); Horstemeyer and Gokhale (1999)) has been implemented. The model incorporates nonlinear isotropic and kinematic hardening, temperature, damage, and rate dependence of the material. Because the material model incorporates damage, the crack advance should take into account the damage present. Our current efforts are focused on development of a damage aware crack growth criteria.

Conclusions

This report summarizes the state of the experimental and numerical simulation study of failure mechanisms in AZ31 Mg. The aim is an enhanced, multiscale microstructure-property model that can be implemented into commercial codes and that can be used in high-fidelity crash simulations for the design and optimization of structural Mg components.

The key findings for this study are the following:

- Deformation induced anisotropy observed in Mg alloys due to the effect of twinning as shown in the experimental work of AZ31.
- Biaxial straining reduces the plastic deformation, induces quicker dislocation nucleation and void nucleation, and produces lower failure strains all relative to uniaxial straining.

- Increasing the stress triaxiality decreases the effective strain-to-failure.
- Low angle grain boundaries allow greater plastic deformation than high angle grain boundaries in the form of dislocation nucleation and/or motion.
- High angle grain boundaries increased grain boundary sliding and grain rotation relative to low angle grain boundaries.
- Stress concentrations at high angle grain boundaries result in lower failure strains relative to low angle grain boundaries.
- (110) textures nucleate Shockley partial dislocations to accommodate deformation while the (100)textures comprise glissile (001) dislocations, resulting in higher failure strains.
- Molecular dynamics simulations performed with different potentials reveal that the stress necessary for void nucleation is proportional to the average surface energy of the potential.

This atomistic study is an important first step in understanding the conditions necessary for void nucleation at the atomistic level, primarily at triple junction. It lays the foundation for continuum level material modeling of damage formation and growth.

References

- D. Bammann D, M. Chiesa, et al. 1993. *Failure in Ductile Metals Using Finite Element Methods*. Third International Symposium on Structural Crashworthiness. University of Liverpool, Liverpool, UK. London : Elsevier Science Publishers, c1993.
- W. Garrison and N. Moody. 1987. *Ductile Fracture*. J Phys Chem Solids 48(11):1035-74.
- G. Gary. (2005). DAVID manual. From:
http://www.lms.polytechnique.fr/dynamique/greef/web4034_david.html.
- A. Gurson. 1977. *Continuum Theory of Ductile Rupture by Void Nucleation and Growth, Part 1: Yield Criteria and Flow Rules for Porous Ductile Media*. J Eng Mater Tech 99(1):2-15.
- J. Hirth and W. Nix. 1985. *Analysis of Cavity Nucleation in Solids Subjected to External and Internal Stresses*. Acta Metallurgica 33(3):359-68.
- M. Horstemeyer. 1995. *Physically-Motivated Modeling of Deformation-Induced Anisotropy*. Mechanical engineering. Atlanta: Georgia Institute of Technology. p. 291.
- M. Horstemeyer and A. Gokhale. 1999. *A Void-Crack Nucleation Model for Ductile Metals*. Int J Solids Struct 36(33):5029-55.
- M. Horstemeyer, J. Lathrop, et al. 2000. *Modeling Stress State Dependent Damage Evolution in a Cast Al-Si-Mg Aluminum Alloy*. Theor Appl Fract Mech 33(1):31-47.
- M. Horstemeyer, D. Oglesby, et al. 2007. *From Atoms to Autos: Designing a Mg Alloy Corvette Cradle by Employing Hierarchical Multiscale Microstructure-Property Models for Monotonic and Cyclic Loads*. Mississippi State: Center for Advanced Vehicular Systems.
- V. Lubarda and D. Krajcinovic. 1993. *Damage Tensors and the Crack Density Distribution*. Int J Solids Struct 30:2859.
- R. Osborn. 2005. A joint USCAR-USAMP material project with DaimlerChrysler, Ford, General Motors and Industry. Southfield, Detroit.

J. Querin, J. Schneider, et al. 2007. *Analysis of Micro Void Formation at Grain Boundary Triple Points in Monotonically Strained AA6022-T43 Sheet Metal*. Mater Sci Eng A 463(1-2): 101-06.

J. Querin. 2005. *Microstructural Characterization of AA6022-T43 Aluminum Alloy Sheet During Monotonic Loading*. Mechanical Engineering. Mississippi State, Mississippi State University. Master of Science.

M. Rashid. 1997a. *A New Theory for Free-Surface Formation in Solid Continua*. Int J Solids Struct 34:2303-20.

M. Rashid. 1998. *The Arbitrary Local Mesh Replacement Method: An Alternative to Remeshing for Crack Propagation Analysis*. Compu Meth Appl Mech Eng 154(1):133-150.

J. Rice and D. Tracey. 1969. *On the Ductile Enlargement of Void in Triaxial Stress Fields*. Journal of the Mechanics and Physics of Solids 17(3): 201-217.

V. Tvergaard. 1982. *Ductile Fracture by Cavity Nucleation between Larger Voids*. J Mech Phys Solids 30(4):265-86.

V. Tvergaard and E. Van Der Giessen. 1991. *Effect of Plastic Spin on Localization Predictions for a Porous Ductile Material*. J Mech Phys Solids 39(6):763-81.

E. Van der Giessen, M. Van der Burg, et al. 1995. *Void Growth Due to Creep and Grain Boundary Diffusion at High Triaxialities*. J Mech Phys Solids 43(1):123-65.

F. Integrated Computational Materials Engineering for Magnesium in Body Applications (Mg ICME)

Principal Investigator: John E. Allison
Ford Motor Company Research and Innovation Center
Mail Drop 3182
2101 Village Road
Dearborn, MI 48124
(313) 845-7224; e-mail: jalliso2@ford.com

Program Technical Administrator: Robert C. McCune
Robert C. McCune and Associates, LLC
5451 S. Piccadilly Cir.
West Bloomfield, MI, 48322-1446
(248) 661-0085; e-mail: robert.mccune@sbcglobal.net

Technology Area Development Manager: William Joost
(202) 287-6020; e-mail: william.joost@ee.doe.gov

Field Project Officer: Magda A. Rivera
(304) 285-1359; email: magda.rivera@netl.doe.gov

Contractor: United States Automotive Materials Partnership¹
Contract No.: FC26-02OR22910 through the National Energy Technology Laboratory

Objectives

The goal of this project is the development of an Integrated Computational Materials Engineering (ICME) capability for optimization of magnesium (Mg) alloys and their manufacturing processes as directed toward production of automotive body components. This is a key enabling technology for future Mg applications, including the Mg front-end architectures of the companion programs AMD 603 – Magnesium Front End Design and Development (MFEDD) and AMD 604 – Magnesium Front End Research and Development (MFERD). The following are specific objectives:

- Establishment of an international ICME infrastructure (including contributor network, knowledge-base, and cyberinfrastructure) for Mg alloys in automotive structural body applications, specifically:
 1. Product and manufacturing process optimization (processes include extrusion, sheet forming, and high-pressure die casting)
 2. Microstructural engineering
 3. Future alloy development
- Development of a web-based cyberinfrastructure to serve as a hub for exchanging high quality data and models between global collaborators in academia and industry.
- Use the aforementioned Mg ICME infrastructure for AMD904 (MFERD Phase II) product and process optimization.
- Attract materials researchers to the Mg field and permit leveraging of their efforts through a collaborative, virtual workplace for sharing and coupling high-quality data and models.

- Advance the scientific understanding of cast and wrought Mg alloys of interest for structural body applications including development of quantitative processing-structure-property relationships for crash energy management and fatigue performance as well as design optimization.
- Incorporate the contributions of high-quality professionals and students educated in materials science and engineering in the U.S., Canada, and China.

Approach

This work is divided into two projects: AMD 702 and AMD 703, within the Automotive Metals Division of USAMP. AMD 703 is organized as a typical USAMP project, funded by the Automotive Lightweighting Materials technology area of DOE, and subject to the cooperative agreement between the two organizations. In AMD 702, however, work conducted by USAMP Original Equipment Manufacturer (OEM) companies (e.g. Chrysler, Ford and GM) is provided on an “in-kind” basis in support of a separate DOE cooperative agreement with Mississippi State University (MSST), wherein ICME is one part of a broader program. The overall ICME for Mg in Body Applications (Mg ICME) project was structurally linked to AMD 604 which had a Phase I duration of three years, concluding at the end of 2009. The projected duration of the Mg ICME Project, however, is five years commencing from its launch in 2007 and concluding in 2012. The USAMP Mg ICME project is an integral component (Task 1.9) of the Three Countries (USA, China, Canada) Mg Front End Research and Development (MFERD) enabling technologies project and is expected to continue as Task 2.9 in the follow-on MFERD Phase II. The plan of work is outlined as follows:

- Implement a worldwide web-based electronic “community of practice” allowing development and integration of multi-scale, physics-based, open-source materials models for selected properties and processes, as well as supporting theoretical and experimental data.
- Establish and verify a web-accessible, “first principles” and calculated phase diagram (CALPHAD)/diffusion database and computational infrastructure. Develop a user-friendly extensible, self-optimizing phase-equilibrium program and graphical user interface (GUI) for a wide range of wrought and cast Mg alloys.
- Establish physics-based and/or empirical relationships for microstructural evolution and similarly-based relationships between microstructures and mechanical response of materials under stress in tension, compression (at varying strain rates), and fatigue loading. This formalism would apply to:
 1. Extruded Mg components
 2. Sheet Mg components
 3. High-integrity, high-pressure die-cast (HPDC) Mg components
- Establish and demonstrate the capability for multi-attribute optimization.
- Coordinate information dissemination and reporting. Establish the overall coordinated work structure between AMD 702, AMD 703, AMD 604 and Canadian and Chinese suppliers involved in the Three Countries MFERD Program.

Accomplishments

Accomplishments for the included time period of this report (Oct. 1, 2008 – September 30, 2009) are summarized as follows:

- Utilization of Mg ICME Cyberinfrastructure as a repository for data from various participants and for fitting the MSST-developed (DGM 1.0) constitutive model.
- Completion of design and testing for an extensible, self-optimizing phase equilibrium software package (ESPEI) and calculation of binary and ternary enthalpies of mixing for incorporation in EPSEI.
- Completed comprehensive characterization of microstructural evolution during extrusion of complex shapes. Completed major enhancement to constitutive model framework by inclusion of twinning. Made substantial progress on FEA simulation of extrusion process.
- Completed calibration of DGM 1.0 model for the Mg sheet alloy AZ31 and used to model warm forming of pan geometry. A significant model enhancement was development of an approach that accounts for and eliminates significant differences in behavior observed between experiment and polycrystalline behavior and an approach for accounting for grain size effects.
- A preliminary model for predicting the influence of microstructure on yield strength in heat treated HPDC Mg alloys was developed.
- Completed a comprehensive characterization of microstructural influences on fatigue response of extruded AM30. These results were captured in a multi-scale fatigue model.
- Project Review meetings were held on April 27-28 and October 1-2, 2009 at USCAR. Progress reports from these reviews are posted on Vroom and SharePoint web sites.
- Coordination with international teams via the 3-Country MFERD meeting in Ontario, Canada, May 11-13, 2009.

Future Direction

- Continue to define and populate the SharePoint web-based “cyberinfrastructure” platform at MSST.
- Demonstrate linkage between first-principles calculations, calculated phase diagrams, and microstructural evolution.
- Continue development of quantitative processing-structure-property relationships for Mg extrusions, sheet formed parts, and super vacuum die casting (SVDC) castings.
- Convene two review meetings of project participants: one at the TMS Annual Meeting in Seattle in February, 2010 and the other at USCAR in the fall of 2010.
- Strengthen international collaboration via careful planning, frequent electronic networking, and next 3-Country annual meeting in Southeast Michigan (October 2010).

Introduction

The background and rationale for the Mg ICME project have been discussed in the first annual report to DOE [1]. The focus of this progress report is on the accomplishments of USAMP Projects AMD 702 and AMD 703 during the federal 2009 fiscal year. Individual reports from

meetings held during 2008 and 2009 are now recorded on both Vroom (USCAR) and SharePoint (Mississippi State) [2]. An ICME project is also part of the U.S.-Canada-China MFERD project as international Task 1.9, and results of that work have been reported in the most recently published project annual review [3].

Task 1 Cyberinfrastructure

The objective of the cyberinfrastructure effort is the development of a community of practice web portal that allows development and integration of multiscale physics-based materials models for selected properties and processes.” The portal is comprised of three parts:

1. *Collaboration management tools* are a web space to gather project-related documents, such as tasks descriptions, annual reports and presentations, as well as broadcasting information about events to all members of the collaboration. Microsoft’s SharePoint server is used to implement the collaboration management.
2. *The repository of material properties (RMP)* integrates three independent web applications: Repository of experimental data, Repository of material constants, and online model calibration tools. The database of the repository supports stress-strain data, microstructural images, and strain-life (fatigue) data. A user can upload data to the repository, search for a particular data set, or retrieve data for further analysis – typically to derive material constants. “Model Calibration” involves solving an optimization problem to fit model parameters using experimental data and fixed constants for the material of interest. The RMP provides online tools, implemented as MATLAB® applications to perform the processes. Currently, three applications are implemented: Damage Model, Image Analyzer, and Multistep Fatigue Fit.
3. *Repository of computational modules*. In addition to the repository of the material properties, the development of the repository of the computational modules has been initiated. The repository is being built using a popular, robust, open source revision control system “Subversion” (a.k.a. SVN) with the ViewVC as the Web client. The candidate codes are being selected and optimized for running on high-performance platforms.

When fully developed and released for public use, the Mg ICME Cyberinfrastructure will be linked to the TMS Materials Technology@TMS site. TMS continues to maintain and update the TMS Materials Technology@TMS website which includes communities focused on magnesium and ICME. Both community sites can be found at <http://materialstechnology.tms.org/TEChome.aspx>.

TMS has supported the development of Integrated Computational Materials Engineering and Magnesium technologies through its involvement in and assistance to these communities. In the past year, TMS has provided support through information dissemination and convening the ICME and magnesium communities. TMS continues to provide venues for the community to meet. In particular, the USAMP project team will meet in Seattle, Washington in February 2010 at the 2010 TMS Annual Meeting. In addition, discussions are underway for participation of the USAMP AMD 703 project team in a specialty conference on ICME planned for 2011. TMS has established a formal ICME Technical Committee, including a cyberinfrastructure subcommittee that includes representation from the USAMP AMD 703 project team.

Task 2 Calculated Phase Diagrams (CALPHAD), Diffusion Infrastructures and Database

Thermochemical data for solid solution phases are crucial for successful CALPHAD thermodynamic modeling; however, they are difficult to measure accurately from experiments due to sluggish

kinetics at low temperatures and the existence of intermetallic compounds, limiting solid solubilities. First-principles calculations treat solution phase thermodynamics by specially-designed small supercells, via the Special Quasirandom Structures (SQS) approach. SQSs are structures with lattice sites occupied by constituent atoms so as to mimic the short-range atomic correlations that exist in a completely random solution. Binary SQSs for cubic and hexagonal crystal phases have been developed and used in recent CALPHAD thermodynamic models to evaluate the mixing parameters for binary solid solution phases. The ternary interaction parameters for solid solutions are often assumed to be zero in many current CALPHAD models due to the scarcity of thermochemical experimental data. Ternary hexagonal close-packed (hcp) SQSs were constructed and first-principles calculations of these structures were used to test the approximation of null ternary interaction parameters in ternary hcp solid solution phases for Mg alloys.

Figure 1 shows the calculated mixing enthalpies for the hcp phase in Mg-Al-Zn from two different binary extrapolations (i.e., assuming that the ternary interaction parameter is zero) and compares these extrapolations with mixing enthalpies directly calculated from ternary SQSs, involving no approximation about ternary mixing parameters. One of the binary extrapolations is based on a CALPHAD assessment and the other is given by first-principles calculations of binary hcp SQSs. The ternary hcp SQSs calculations are performed for four different compositions: $Mg_2Al_3Zn_3$, $MgAlZn$, Mg_2AlZn , and Mg_6AlZn . For the binary extrapolated results from the previous CALPHAD assessments, interaction parameters for binary mixing are taken from [5] for Mg-Al and from the COST 507 database [6] for Mg-Zn and Al-Zn, respectively. By comparing the results of the CALPHAD assessment with the extrapolated first-principles binary SQSs, we see that the first-principles results predict a more negative mixing enthalpy surface in Mg-Al-Zn. However, the comparison with the direct ternary SQS calculations gives us a direct test of the assumption of a zero ternary interaction parameter. This comparison indicates that a true ternary interaction parameter is significant in this system, and future CALPHAD assessments in this system should introduce this ternary interaction parameter to make the mixing behavior of hcp to be more negative on Al/Zn side in Figure 1.

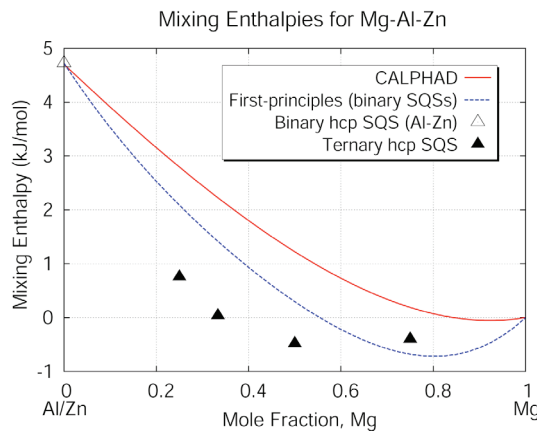


Figure 1. Calculated mixing enthalpies for the hcp phase in Mg-Al-Zn from two different binary extrapolations (CALPHAD assessments (top line) and hcp SQSs (bottom line) and ternary hcp SQSs calculations.

A major goal of this task is the development and implementation of a user-friendly, extensible, self-optimizing phase equilibrium software package: ESPEI. This software will be used for a range of wrought and cast Mg-based alloys permitting integration of databases (crystallographic, phase equilibrium, thermochemical, and modeled Gibbs energy, etc.) and database development (automation of thermodynamic modeling) with a GUI (graphical user interface). The infrastructure of experimental data storage as well as the automation of database development is unique for ESPEI. It will be linked with the first principles database developed by Northwestern University

(as inputs) and with microstructural evolution models developed at Mississippi State University, the University of Michigan, the University of Virginia and elsewhere (as outputs). All of these university contributions are a part of this project.

The blueprint of the data infrastructure of ESPEI for storing input data used for thermodynamic modeling and output data for thermodynamic analyses has been updated. The GUI for data inputs was designed and the automation for thermodynamic modeling was tested.

The updated overall infrastructure of ESPEI includes three parts:

1. The GUI on the client side. It provides interfaces to manage the databases, analyze and collect the databases, communicate with internal and external CALPHAD codes, perform automation of database development, and save the modeled data.
2. The database on the server side. It includes the target data to store input data for thermodynamic modeling and the model data to store output data for thermodynamic analyses.
3. The database development module in connection with the third party code (Thermo-Calc® software is mainly used in ESPEI) in order to generate or model new thermodynamic data for the system of interest. During this reporting period, the main focus was on the GUI and database. Tests were conducted on the database development module. Full functions will be available in next version of ESPEI (version 1.2).

Task 3 Processing-Structure–Property Relationships for Extruded Magnesium Components

The team selected alloys AM30 and AZ61 as the model alloys for this task. Extrusions are being supplied by the AMD 604 extrusion task team in the form of crush columns.

MSST continues to develop the fundamental knowledge of the extrusion process of Mg alloys to better understand their processing –structure – property relations. The research activities during this reporting period have been focused on: (1) performing lab-scale indirect extrusion experiments to characterize the evolution of microstructure during the process, (2) extending the capability of the extrusion fixture to experimentally study weld seam formation, (3) enhancing the current constitutive frameworks to increase the fidelity of the predictive response of Mg alloys with twinning, and (4) carrying out finite element simulation of the extrusion process using Lagrangian (ABAQUS®) and Eulerian (HyperXtrude®) finite element codes.

Figure 2 shows a montage of the experimental results of the microstructure characterization study being performed on a partially extruded Mg AZ61 billet. The extrusion was performed using a lab-scale fixture developed to quantify the processing-structure-property aspects of Mg alloys. The grain structure and texture information obtained in these studies will form part of a material database for extruded Mg alloys that can be used for model calibration and validation.

Additionally, both material testing and constitutive modeling were performed for Mg alloys (AM30, AZ61, and pure Mg). Simple compression tests were performed at temperatures ranging from room temperature to 400°C under three true strain rates of 10⁻³/s, 10⁻¹/s, and 1/s.

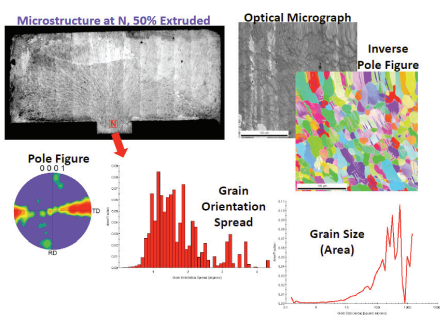


Figure 2. Microstructure characterization study at thecenter of the bearing area of a 50% partially extruded billet.

Samples with extrusion (ED) and radial directions (EN) were tested and texture evolution characterized. Texture measurements were performed using electron back scatter diffraction (EBSD) and X-ray diffraction (XRD) techniques at MSST, and Neutron Diffraction at LANL. The Voce hardening model in the VPSC code was used to fit the stress strain curves at 25C with two orientations. Current efforts focus on using this model to fit the stress-strain curves obtained at various temperatures and strain rates. One major contribution of the MSST team was the development of a novel theory explaining the hardening behavior due to twinning. It is based on the dislocation transmutation mechanisms and the accommodation effects by twinning. Such theory will be implemented in the VPSC code.

Task 4 Processing-Structure–Property Relationships for Sheet Magnesium Components.

The team selected alloy AZ31 as the model alloy for this task. The alloy was in the form of a formed box sample provided by the USAMP AMD 602 Warm Forming of Mg project team.

A central objective for the sheet-forming task is to develop a physically-based material model and an experimental-validated sheet forming model with corresponding design methodologies to enhance the formability of Mg alloys, in particular AZ31. The current work involves establishing material anisotropy relationships to understand the effects of microstructure state, product geometry and processing parameters on the resulting mechanical properties and distortion of Mg sheets.

The MSST team is developing appropriate constitutive models which cover critical features including viscoplasticity, anisotropy, damage, strain sensitivity, temperature dependence, grain size and twinning. Currently, an existing MSST DMG 1.0 microstructure-plasticity model was calibrated with the material responses of Mg AZ31 from uniaxial tensile tests at various strain rates and temperatures (see Figure 3). This model will be enhanced to include the aforementioned critical features such as twinning.

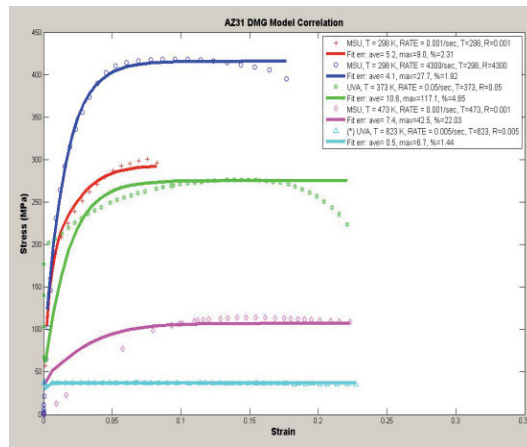


Figure 3. Material fitting of Mg AZ31-O with DMG Model(solid lines are models, symbol points are experimental data)

To take advantage of shell elements that have significantly improved numerical run time when compared with 3D elements, the stress integration algorithm was efficiently reformulated in order to take into account plane stress conditions and implemented in a general finite element code, i.e. ABAQUS. In this formulation, only the plasticity part of the DMG 1.0 was considered.

The creep plasticity model used by the University of Virginia was also implemented as a special case of the DMG plasticity model (no hardening). This model is predicated on use of the Zener-Holloman parameter in conjunction with the Sellars-Tegart Equation to generate a plastic flow rule.

The forming limit diagram (FLD) provides the maximum strains of sheet metals that can be sustained prior to the onset of localized necking, a common failure mode in metal forming. This failure process is controlled not only by external loading but also by the state of microstructure. To evaluate the mechanical properties of Mg AZ31 alloy including formability, Finite Element (FE) simulations of warm-forming of magnesium sheets were performed at various conditions (temperature, tool speed, friction, binding pressure, etc.) using the MSST DMG 1.0 model.

The punch was assumed stationary, while the die moved down after the sheet was clamped with a given binder force and the sheet was then formed around the stationary punch. A careful set of friction calibration tests were conducted and the coefficient of friction was set in a range of 0.16 to 0.20. The sheet and die temperatures were kept to be the same, starting at 250°C with an incremental increase of 25°C to 350°C. A representative pan from a simulation where wrinkling occurred is shown in Figure 4. Careful quantitative comparisons with measurements from formed pans are underway. However, preliminary results for the Mg AZ31 material designated as “O” are available based upon the measured minimum pan thickness in the pan wall corners. Results from the two material models are nearly identical in that both predict an insensitivity of the minimum thickness to temperature, and both suggest smaller thinning at the wall corners than what is measured from pans formed under the same conditions.

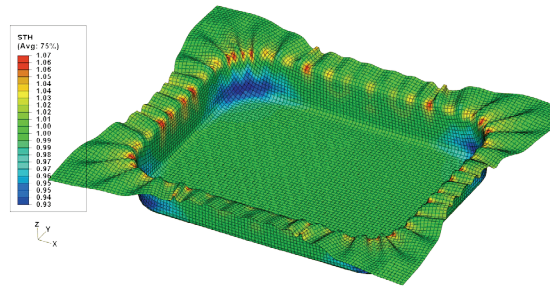


Figure 4. Predicted thickness distribution after warm forming of a pan. Mesh contours are sheet thickness in the formed pan (darker areas in corners are thinner than flat section).

UVA is also a participant in the USAMP AMD602 (Warm Forming of Magnesium) project, and its tasks under AMD703 are coordinated with efforts to develop constitutive equations to model the warm-forming of magnesium sheet alloys (usually AZ31). Two basic approaches are being examined:

- *Phenomenological approach* - Experimental constitutive data, collected under the auspices of the AMD 602 project, has been uploaded to the ICME web-portal. Curiously, the constitutive response of the most formable alloys is not exceptional. They are within the range of behaviors observed for the others. Colleagues at MSST have made use of the uploaded data to parameterize the constitutive models that they are developing. In turn, UVA has down-loaded the latest versions of MSST modeling programs, including the GUI, DMGfit, for developing its own parameter set for the internal state variable model [7].
- *Crystal plasticity/mechanistic approach* - This approach addresses the fact that the polycrystalline response is a result of individual grain-level deformation mechanisms of dislocation slip and deformation twinning. A model for nucleation and growth-type dynamic recrystallization was incorporated within the viscoplastic self-consistent (VPSC) code. The model correctly predicts two characteristic features of DRX in Mg alloys, strain softening as well as saturation of the texture evolution.

Another aspect addressed is the reconciliation of previously-reported differences between single-crystal experimental data and polycrystal modeling parameters (i.e. the critical resolved shear stress (CRSS) values of individual slip mechanisms.) It was found that the stiffness of the

interaction between individual grains and the surrounding polycrystal has a strong impact upon the model parameters. The affine (?) model is shown to provide the best overall description and was used to determine the grain-size dependence of the individual slip systems and to extract the intrinsic friction stress. When these friction stresses are compared with single crystal CRSS values, corrected for the effects of solid solution strengthening/softening, the differences between experiment and model are eliminated.

Task 5 Processing-Structure-Property Relationships for Die-cast Magnesium Components

The team selected AZ91D as the model alloy for this task. Super Vacuum Die Cast (SVDC) shock towers from the AMD604 casting task team have been provided for use in this project Task.

The goal of this task is the development of experimentally-validated models that account for the influence of microstructure on monotonic tensile properties and low-cycle fatigue response of high-pressure die-cast (HPDC) magnesium alloys.

The first version of a yield strength model was developed for SVDC AZ91. The model accounts for initial solute distribution due to solidification and accounts for the following mechanisms of strengthening as shown in [Figure 5](#):

- Solute strengthening of the α -Mg, due to interactions of misfitting solute with $< a >$ type dislocations
- Strengthening within the α -Mg, due to the β - phase precipitation
- “Composite” strengthening due to the interdendritic eutectic with intermetallic phases
- Grain / cell size strengthening
- Dislocation hardening

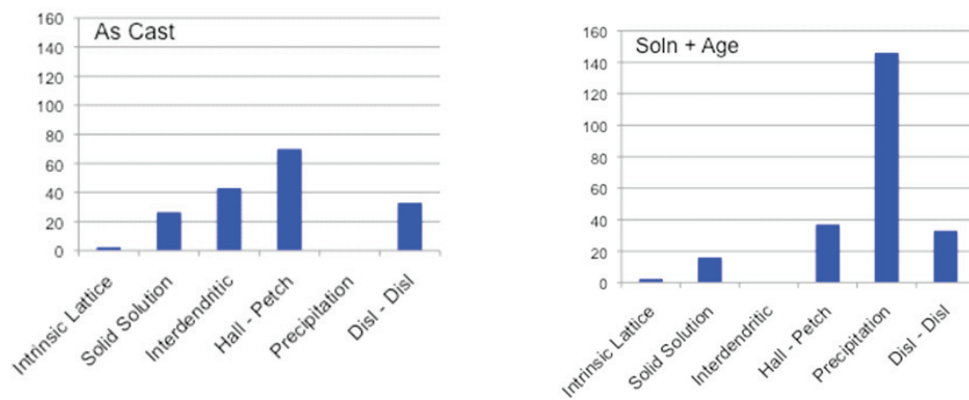


Figure 5. Comparison of contributions to strengthening, by specific mechanism, for as-cast and solution plus (peak) aged AZ91D(NOTE: Vertical axes are “Strength Increment in MPa units”).

Grain/cell size strengthening and the interdendritic composite strengthening effect are predicted to be important for the as-cast material. Conversely, precipitation strengthening most strongly influences the strength of the solution treated plus aged material. The model predicts the yield strengths of the as-cast and aged materials to be 170 MPa and 234 MPa, respectively. In both cases the strength is over-predicted. The source of this discrepancy is not yet clear, however, it is likely to be in part due to the fact that microstructural and physical parameters within the models are not yet fully determined. Additionally, features of the model, such as the assumption

that solute primarily interacts with $\langle a \rangle$ dislocations at yielding, may not be representative of the actual deformation mechanisms. Future characterization experiments will address the primary unknown parameters in the models and the models will be refined, as appropriate.

The investigation of low-cycle fatigue behavior using samples from 70 SVDC AZ91D “shock tower” castings is continuing, with a focus of building a statistically-significant baseline at several locations. Eighty fatigue specimens have been machined from the shock towers and heat treatments are now being conducted. Strain-controlled fatigue tests on heat-treated materials will begin in this quarter with the objective of developing a fatigue life database for comparison with the fatigue behavior of the as-cast material.

The model employs analytical expressions for each of the mechanisms and assumes linear superposition of contribution from each mechanism. A Taylor factor of 4.5, suggested by the work of Caceres and Lukas, was employed. The preliminary model was tested with comparison to the tensile properties of the SVDC shock tower material.

Task 6 Multi-Attribute Design Optimization

This task involves multilevel optimization of product-material systems. Many complex engineering systems are more readily optimized when they are decomposed into separate system and subsystems with partitioned design variables and design constraints. The solution to the multilevel optimization problem is iterative and requires careful coordination among connected elements to ensure proper convergence.

The analytical target cascading (ATC) method [9,10] was applied to a two-level product-material optimization of a 400-mm long prismatic multi-cell, multi-corner thin-walled tube. The system-level (product) design variables consist of dimensions D_o , D_i , and wall thickness, t along with exponent b in Smith-Watson-Topper fatigue model, whereas the subsystem-level (material) design variables describe material microstructure parameters (i.e., the initial radius of a spherical void, r_o , average size of inclusion particles, d_n , particle volume fraction, f_n , grain size, DCS, and initial void volume fraction, $volF$) as defined by the ISV-based plasticity damage model. At the system level, the objective function is the tube weight with constraints on fatigue life and the mean crush force. At the subsystem level, the objective function is formulated as the deviation between the yield and ultimate stresses evaluated at the subsystem level and the corresponding target values as specified at the system level. The only constraint at the subsystem level is the lower bound limit on material toughness as measured by the area under the stress-strain curve. The two-level optimization problem is solved for a minimum weight tube that gives 25% greater mean crush force and 50% higher toughness than the baseline model made of A356 aluminum alloy.

Task 7 Multi-Stage Fatigue Model

The MSST fatigue team continues model development of the MultiStage fatigue (MSF) model by characterizing the fatigue properties of an extruded AM30 magnesium alloy. Fully-reversed, strain control fatigue tests were performed on specimens extracted from regions having varying microstructural features. Using scanning electron microscopy, the fracture surfaces of each failed specimen were analyzed in order to establish structure-property relationships between microstructure and fatigue behavior.

In addition to characterizing microstructural features such as particle size and grain size, Taylor factor as a measure of average grain orientation and the number of cycles to failure were correlated. As such, these structure-properties were implemented into the MSF model to capture the microstructure effect on fatigue life. [Figure 6](#) presents the mean predictions of

the MSF model along with the upper and lower bounds compared to the experimental fatigue results.

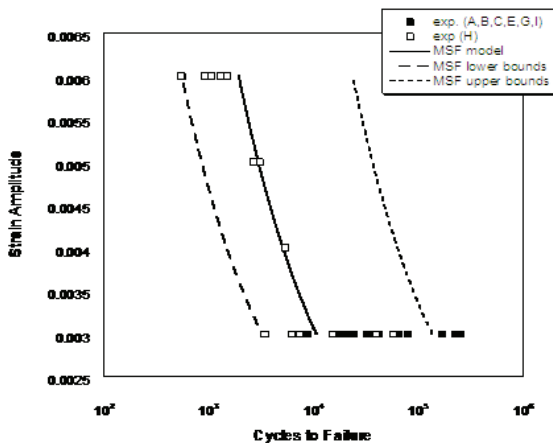


Figure 6. The Multistage fatigue model predictions of experimental fatigue results of extruded magnesium AM30 alloy.

In addition to the model development for base materials, work has begun to adapt the MSF model to the friction stir spot welds (FSSW) of magnesium alloys. Load control fatigue tests for three R-ratios were conducted on single weld lap-shear coupons to determine fatigue-life properties. The fractured coupons were examined under optical and scanning electron microscopes to determine the fatigue crack characteristics. To predict the fatigue life of the lap-joint coupons, initial model development has focused on developing the long crack growth portion of the model. This crack growth approach is based on a modified Paris law and employs a stress intensity factor solution for kinked cracks. The predictions for long crack growth model compared well to the experimental fatigue life results.

Conclusions

The Integrated Computational Materials Engineering for Mg in Body Applications project was launched in 2007 and interfaces with the Magesium Front-End Research and Development ('MFERD') projects (AMD604 and its proposed Phase II continuation). Substantial progress has been made in all task areas. The Task Teams and project leadership meet semi-annually to discuss progress and future plans. The TMS "Magnesium" and "ICME" web portals are operational and acquiring depositions of information.

References

Integrated Computational Materials Engineering, Annual Report to DOE, J.E. Allison, Principal Investigator, USAMP, 2007. http://www1.eere.energy.gov/vehiclesandfuels/pdfs/lm_07/lightweighting_matls_07.pdf, http://mferd.hpc.msstate.edu/_layouts/login.aspx

A Canada-China-USA Collaborative Research and Development Project: "Magnesium Front End Research and Development (MFERD)" 2008 Annual Progress Reports, Project Technical Committee, Alan A. Luo, Eric A. Nyberg, Kumar Sadayappan and Wenfang Shi, Niagara-on-the-Lake, Canada, May 2009.

Y. Zhong, M. Yang, Z.-K. Liu, CALPHAD, 29(4): 303-11, 2005.

Ansara, A. T. Dinsdale, M. H. Rand, Thermochemical Database for Light Metal Alloys, European Cooperation in the Field of Scientific and Technical Research, 1998; <http://iweb.tms.org/forum/default.aspx?forumid=15>

Bammann, D.J., Chiesa, M.L., and Johnson, G.C., "Modeling large deformation and failure in manufacturing processes," pp. 359-376 in Tatsumi, T., E. Watanabe and T. Kambe, eds., *Theoretical and Applied Mechanics*, London: Elsevier (1996).

Sellars, C.M., Tegart, W.J., 1967. "Relationship between strength and structure in de-formation at elevated temperature", Mem. Sci. Rev. Metall. 63, 731-745.

Michelena, N.F., Kim, H.M., and Papalambros, P.Y., "A System Partitioning and Optimization Approach to Target Cascading," *Proceedings of the 12th International Conference on Engineering Design*, Munich, Germany, 1999.

Kim, M.K., Michelena, N.F., Papalambros, P.Y., and Jiang, T., "Target Cascading in Optimal System Design," *Journal of Mechanical Design*, Vol. 125, 2003, pp. 474-480.

Acknowledgments

The success of this project is due to the dedicated efforts of team members at Ford and General Motors, as well as The University of Michigan, The University of Virginia, Northwestern University, MaterialsInformatics, LLC, Magma Foundry Technologies, Inc., ThermoCalc Software, Inc., Oak Ridge National Laboratory, Pacific Northwestern Laboratory and The Minerals, Metals and Materials Society (TMS). The project leadership also acknowledges the ongoing collaboration with colleagues at Mississippi State University. The USAMP ICME project management team is comprised of Lou Hector, GM; John Allison, Ford; and Robert McCune, Project Administrator. The continuing support of our respective organizations and the US Department of Energy is gratefully acknowledged.

Endnotes

Denotes projects 702 and 703 of the Automotive Materials Division (AMD) of the United States Automotive Materials Partnership (USAMP), one of the formal consortia of the United States Council for Automotive Research (USCAR), set up by Chrysler, Ford and General Motors (GM) to conduct joint, pre-competitive research and development. See www.uscar.org.

G. Multiscale Microstructure-Property Plasticity Considering Uncertainty in the Southern Regional Center for Lightweight Innovative Designs (SRCLID)

Principal Investigator: K.N. Solanki
Professor, Mechanical Engineering
Center for Advanced Vehicle Systems (CAVS)
Mississippi State University
PO Box 5405, Mississippi State, MS 39762
(662) 325-8822; e-mail: bammann@cavs.msstate.edu

Participants: D.J. Bammann, E.B. Marin, M.F. Horstemeyer, P.T. Wang, H. El Kadiri, Y. Hamm

Technology Area Development Manager: Dr. Carol Schutte
(202) 586-1022; e-mail: carol.schutte@ee.doe.gov

Project Manager: Magda Rivera
(304) 285-1359; e-mail: magda.rivera@netl.doe.gov

Contractor: Mississippi State University
Contract No.: DE-FC-26-06NT42755

Objective

Develop physically-based and experimental-validated material models, extrusion and sheet process models, and corresponding design methodologies to enhance the workability of Mg alloys (extrusion: AM30, AZ61; sheet: AZ31).

In particular, the work involves establishing material anisotropy relationships to understand the effect of material state (microstructure), product geometry and processing parameters on the mechanical properties, and final geometry (distortion) of formed Mg components.

Approach

We developed a material database, internal state variables (ISV) material models, and process models for extruded (AM30 and AZ61) and warm formed (AZ31) magnesium alloys. The database includes results from the mechanical and microstructure characterization studies performed using current experimental equipment at CAVS. The material model being developed is based on a multiscale modeling approach, where information from crystal plasticity, dislocation dynamics, and molecular dynamics simulations are to be used to provide insights into the functional form of the ISV's evolution equations and corresponding material parameters. The extrusion and forming process models being constructed are finite element codes that are suitable for problems with large mesh distortions (e.g., extrusion using flat dies). Specific sub-tasks to be performed are as follows:

- Quantify structure-property relations with consideration of uncertainty for AZ31 sheet metal.
- Quantify structure-property relations with consideration of uncertainty for pre-extruded and extruded AM30 and AZ61.
- Perform lab-scale extrusion experiments on Mg alloys AM30 and AZ61 to generate data for validation of simulation tools.

- Develop crystal plasticity and ISV macroscopic models to model microstructure evolution during extrusion processes.
- Construct finite element models and performing analysis of stamping for Mg alloys.
- Develop robust process models for lab-scale and industrial extrusion processes using Eulerian-ALE finite element formulations.
- Develop methodologies for the optimum design of extrusion/stamping processes considering uncertainty.

Accomplishments

- Completed implementation of plane stress case of the MSU DMG 1.0 Plasticity-Damage material model (ABAQUS VUMAT).
- Completed implementation of the Sellars-Tegart model (ABAQUS VUMAT).
- Performed sheet metal forming simulations at various temperatures and binding pressures with GM researchers.
- Developed PAMSTAMP 2g material cards based on MSU DMG 1.0.
- Designed lab-scale indirect extrusion fixture, performed experiments on Mg AZ61 billets, and characterized deformed microstructure of material. Data generated is being used for validation of numerical simulation tools.
- Identified numerical formulation (Eulerian) for FE analysis of extrusion process, selected a commercial code (HyperXtrude(HX)), and performed preliminary simulations of lab-scale extrusion process (flat die). The preliminary predicted results do not yet match the experimental data.
- Performed numerical simulations of extrusion process with streamline dies using ABAQUS and a crystal plasticity model. The predicted textures follows trends observed from lab-scale experiments.
- Wrote a number of peer reviewed journal publications (10).

Future Direction

- Enhanced numerical framework for ISV material model accounting for texture/isotropic damage: research version 1.4 (EMMI-TXT).
- Develop methodology to incorporate twinning and recrystallization.
- Enhanced numerical framework for ISV material model accounting for twinning/recrystallization: research version 1.5 (EMMI-REX).
- Finish parametric study of lab-scale extrusion experiments.
- Finish FE modeling of lab-scale experiments.
- Model industrial extrusion process (Timmisco's porthole die).
- Implement constitutive model frameworks in HyperXtrude.
- Carry out studies of recrystallization and seam weld formation.

Introduction

In this annual report, we present the current progress of material model development for extrusion, and sheet metal forming. Our goals are twofold: (1) an experimentally validated cradle-to-grave modeling and simulation effort to optimize automotive components (i.e., front end) for magnesium alloys with consideration of uncertainty in order to decrease weight and cost, and, yet, to increase the performance and safety in impact scenarios; (2) the multiscale (“From Atoms to Autos”) modeling approach in which we quantify the microstructure-property relations by evaluating various length scales, starting at the atomic level for each step of the manufacturing process (i.e., extrusion, sheet forming) for vehicles.

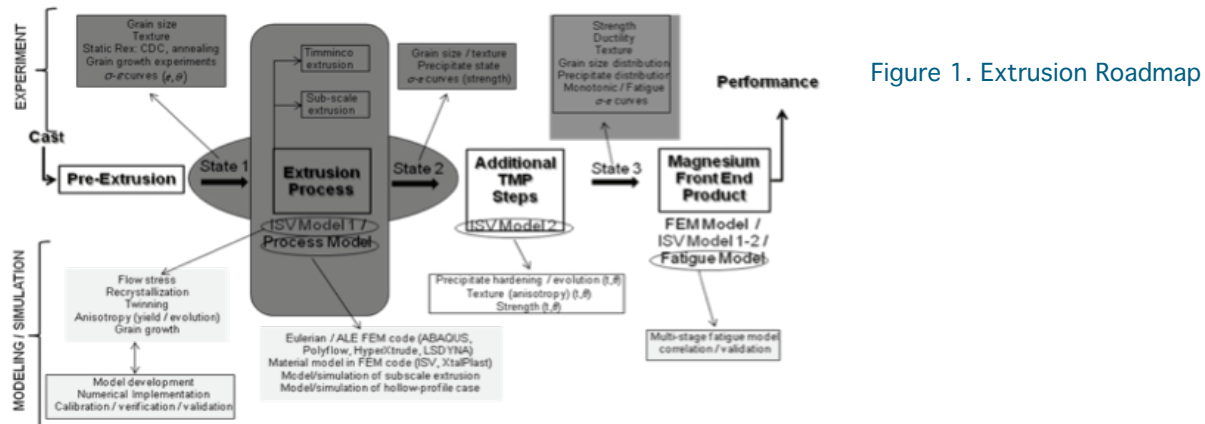


Figure 1. Extrusion Roadmap

At MsSt, we have formed several focused research groups (i.e., extrusion, sheet, fatigue, cyber) and established roadmaps. One example of the extrusion roadmap is depicted in the chart above, **Figure 1**, in which a microstructure /experimentation team, simulation team, constitutive material modeling team and performance team are working together to create a high impact technology portfolio.

Lab-Scale Extrusion Fixture and Extrusion Experiments

The lab-scale indirect extrusion fixture has been developed to quantify processing-structure-property relations of extruded Mg AZ61 and AM30. The main goals here are (i) to understand the influence of process parameters on the microstructure and mechanical properties of extruded material, and (ii) to generate experimental data for validation of the modeling tools (finite element and material models). The lab-scale extrusion fixture contains (i) a chamber, (ii) a replaceable die, and (iii) a base. The chamber is made of two parts (top – bottom), each part having an internal sleeve. A clamp holds these two parts together. The designed fixture and its set-up on the Instron machine for the extrusion experiments are shown in **Figure 2**.



Figure 2. Indirect extrusion fixture and set-up on the Instron machine.

This lab-scale extrusion process is defined by three processing parameters: extrusion ratio (ER), billet temperature, and ram speed. A parametric study of the process is being performed by varying these parameters one-at-a-time to see their effect on (i) the metal flow patterns, (ii) the microstructure evolution, and (iii) the mechanical properties of the Mg alloys.

A test matrix is given in **Table 1**. The sample size is 31.75 mm diameter x 304.8 mm length, the bearing length is 1.71 mm, and the orifice diameters are 6.35 mm (ER=25) and 3.1 mm (ER=100). The Mg alloy being studied currently is AZ61.

Table 1. Lab-scale Extrusion Parameters

Billet Temp.	Ram Speed	ER
454C/850F	5,10 mm/min	25,100
482C/900F	5,10 mm/min	25,100
510C/950F	5,10 mm/min	25,100

Interrupted extrusion experiments for selected cases of Table 1 have been performed to study the flow patterns and microstructure evolution of the material during the extrusion process. Flow patterns for Mg AZ61 samples extruded at 25%, 50%, and 75% of the length have been determined under specified processing conditions (ram speed = 5 mm / min, billet temperature = 454°C, and ER = 25). The microstructure evolution during extrusion has been characterized by performing EBSD studies on the partially extruded billets. In particular, microstructure features at material points along three streamlines have been determined. **Figure 3** shows the evolution of texture along one streamline (center) on the 25% extruded billet. Clearly, at the selected material point, the texture of the pre-extruded billet evolves towards a rod-type texture typical of extrusion. Shearing effects due to the die wall, which usually tend to weaken this texture, are not predominant at these points because indirect extrusion minimizes the frictional effect as compared to direct extrusion. **Figure 4** presents a number of microstructure aspects of a material point at the center of the bearing area. In particular, the grain structure is being fully characterized through inverse pole figures and plots for grain orientation spread and grain size. This material database is currently being used to enhance/validate internal state variable and crystal plasticity constitutive models for Mg alloys.

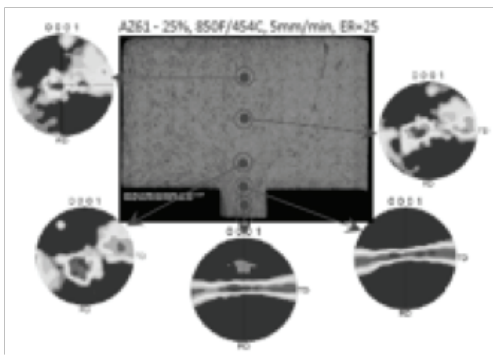


Figure 3. Evolution of texture at material points along a streamline through the center of the 25% partially extruded sample.

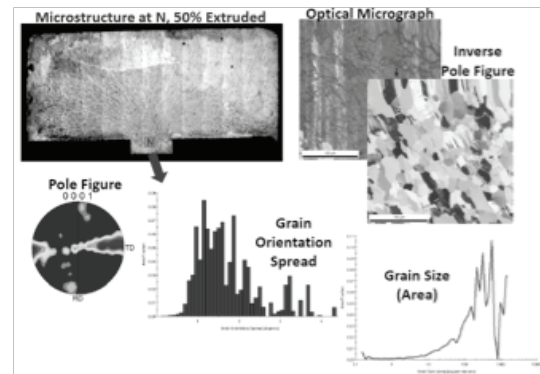


Figure 4: Microstructure characterization study (texture, grain structure) at a material point at the center of the bearing area.

A new research activity identified in this task is the experimental analysis of longitudinal weld or seam welds that are typically present in extruded hollow profiles. For robust structural applications, the mechanical properties of the extruded product at or near these welds should not be inferior to those of the rest of the extrudate. As such, understanding the formation of

weld seams in extruded Mg alloys and the processing parameters that affect their mechanical properties (strength, ductility) will contribute to the fundamental knowledge of extrusion process for magnesium alloys as well as will enhance the structural applications of Mg extruded components. Weld seams are usually produced using extrusion dies having webs/hollow channels and weld chambers (porthole dies). The weld seams form as the metal flowing through the die splits over each web and then rejoins and welds together at the rear side of the webs (weld chamber) before passing through the bearing zone. The quality of the solid state bond formed at these seams depends on a number of factors, including processing time, temperature, and pressure.

In this task, the solid-state bonding process that occurs in porthole dies of hollow Mg extrusions will be examined using a “splitter” placed between the chamber and the die. In essence the splitter is a disk with a web that divides the metal flow into two material streams. The material is joined again at the rear of the web forming a solid state bond. The rear end of the web has a butt-ended shape which is apart 1.71 mm from the bearing area. This very narrow cylindrical space constitutes the weld chamber. The extruded profile obtained in this die will be solid and will contain an extrusion seam in the middle corresponding to the location of the web. **Figure 5** presents the top and bottom parts of the preliminary design of the splitter, while **Figure 6** displays the set-up of the splitter in the lab-scale extrusion fixture. Preliminary extrusion weld seam experiments using the above splitter have been performed using 1100F Aluminum due to our limited material stock on Mg alloys. Processing conditions were: billet temperature 300°C, die speed 5mm/min, and ER of 25. **Figure 7a** shows the beginning of the extrudate where the two-welded metals streams are clearly observed. The extrudate shows a characteristic groove due to the particular splitter design. **Figure 7b** presents an optical micrograph at the center of the extrudate. At the magnification used (600X), traces of the weld seam can be observed.



Figure 5. (a) Top and (b) bottom of splitter.

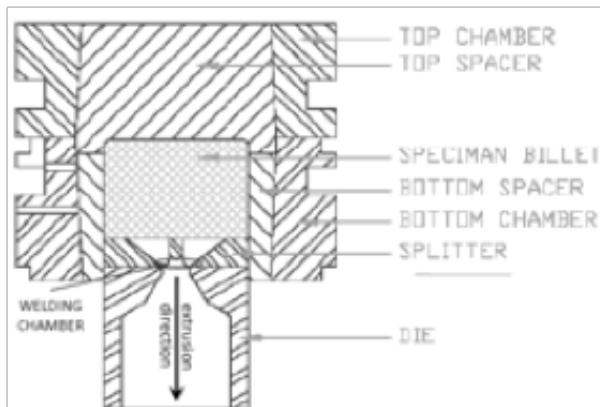


Figure 6. Splitter set-up in extrusion fixture.

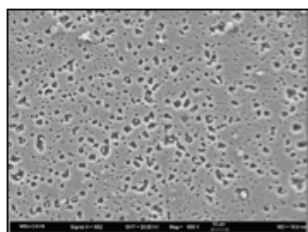


Figure 7. (a) Welded Al extrudate, and (b) weld seam at center of extrudate at 600X.

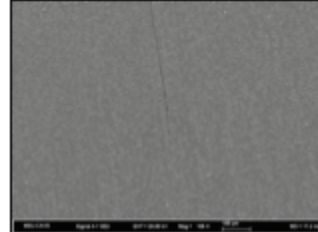
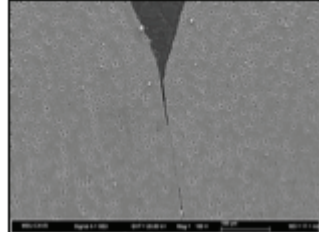


Figure 8. (a) Initiation of weld seam in welding chamber at 180X and (b) weld seam in the bearing area at 105X.

Figures 8 presents optical micrographs showing (i) the initiation of the solid state bonding just after the rear end of the web (welding chamber) and (ii) the weld in the bearing area. Note that in the welding chamber, just at the rear end of the web, Figure 8a, there is an incomplete filling of metal that induces the formation of a gas pocket. This usually indicates that sliding friction occurs at the rear-end portion of the web due to the small reduction step. Here, the free-surfaces sliding from the web surface will encounter each other at the rear end of the gas pocket, where they are pressed into each other, producing the solid state pressure-welding. Conditions that affect the quality of this weld are surface extension, contact pressure, and temperature. Note that traces of the weld seam are also observed in the bearing area, Figure 8b. Current work on weld seam formation is focused on improving some details of the present splitter design as well as modifying its design to extrude dog-bone profiles for tensile testing to determine the mechanical properties of the weld seam area. Experiments on Mg alloys will be performed after the preliminary testing on 1100F Aluminum is completed.

Modeling the Extrusion Process using the Finite Element Code ABAQUS

Extrusion is a metal forming process used to produce long complex profiles with high tolerance and surface quality. Unlike other material forming processes, such as forging and rolling, profile extrusion process usually has complex material flow patterns accompanied with extremely large and severe plastic deformation. Such a feature puts rigorous requirements on the numerical tools used to simulate the extrusion process. In this work, the Lagrangian capabilities of ABAQUS/Standard have been used to perform simulations of an axisymmetric direct extrusion process of AZ61. A crystal plasticity model based on a Taylor hypothesis and implemented in a user material routine has been used for this purpose. The goal here is to test the robustness of the numerical implementation of the model as well as to predict trends on texture evolution during extrusion. As Lagrangian codes have limitations to model the material flow in flat dies unless intensive remeshing is used, these simulations have used a 25° streamlined die. Also, the analysis assumed a constant temperature as this research version of the material model does not allow for temperature effects. For the simulations, the crystal plasticity model neglects twinning and considers three slip deformation modes: basal $\langle a \rangle$, $\{0002\} <110>$; prismatic $\langle a \rangle$ $\{100\} <110>$; and second order pyramidal $\langle c+a \rangle$, $\{112\} <113>$. The value of the critical resolved shear stress for basal, prismatic, and second pyramidal slips are assumed to be in the ratio of 1:1:5, respectively. The material parameters of the flow rule and hardening law have been calibrated by correlation with experimental stress-strain behavior determined at room temperature at a strain rate of 0.001 s^{-1} (see **Figure 9**). The initial texture (input to the extrusion model) used corresponds to the one determined using X-ray diffraction on the as-received pre-extruded AZ61 billet as shown in **Figure 10**. Note that this initial texture has a preferred c-axis orientation distribution perpendicular to the extrusion direction.

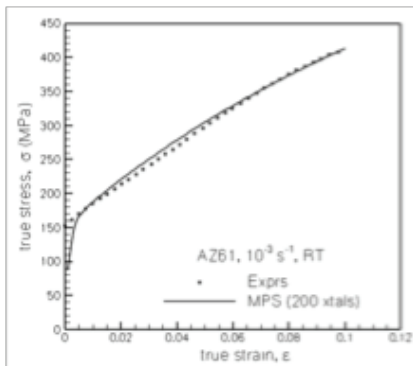


Figure 9. Stress-strain response of pre-extruded Mg alloy AZ61.

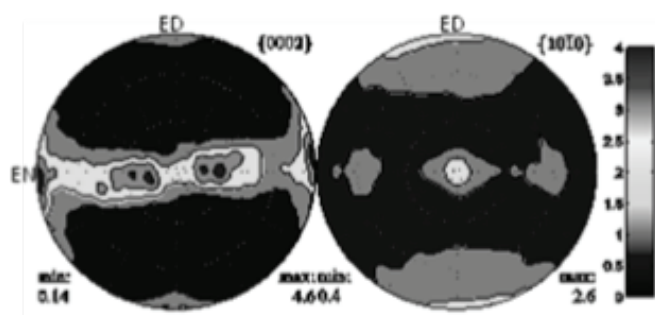
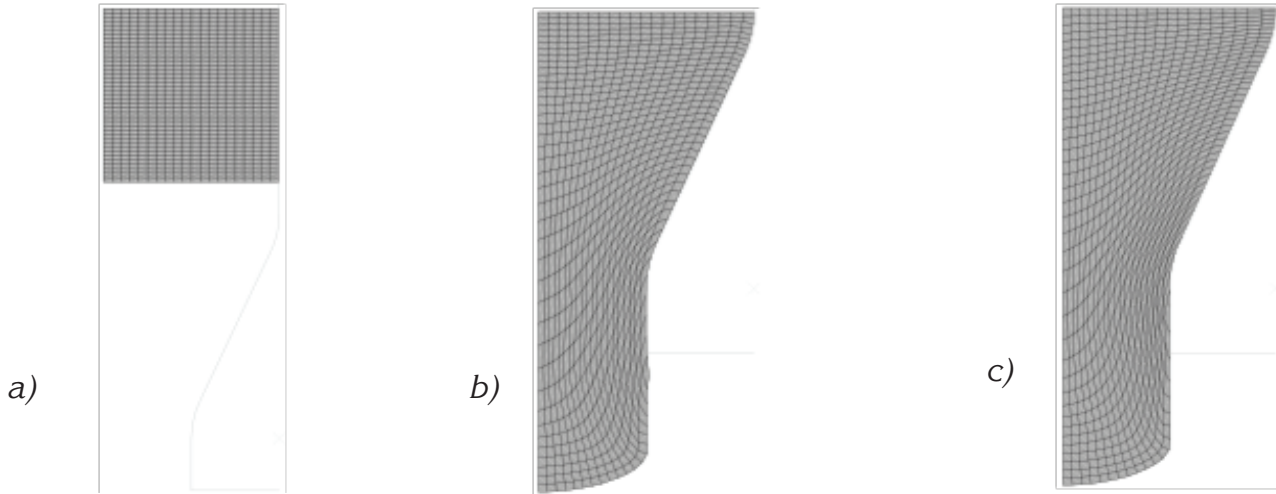


Figure 10. Initial texture of as received pre-extruded AZ61 billet. ED: extrusion direction, EN: extrusion normal.

The finite element mesh used here is given in [Figure 11a](#). It consists of 800 axisymmetric quadrilateral reduced integration elements, ABAQUS-type CAX4R. An aggregate of 172 HCP crystals is assigned to each of the integration points whose initial orientation distribution is given in [Figure 10](#). The constitutive response of each crystal is computed using the crystal plasticity framework of Marin (2006), while the average response of the aggregate is computed using the Taylor approach.



[Figure 11](#): (a) Finite element model used for ABAQUS simulations of extrusion process, (b) deformed mesh for zero friction, (c) deformed mesh for friction coefficient of 0.1.

The workpiece is a cylinder with dimensions of 20 mm diameter by 10 mm height. Processing conditions used are the following: ram speed 5mm/s, room temperature, and extrusion ratio of four (extrudate has a solid circular profile of 10 mm diameter). The workpiece is extruded about 100% of its height. Two friction conditions were used for the billet-tool interface: frictionless and a friction coefficient of 0.1. The deformed meshes obtained from the simulations are presented in Figures 11b-c, for the frictionless case and for a friction coefficient of 0.1, respectively. Note that friction intensifies the element distortions. The load-displacement curve for the process for the two friction conditions and for the ram speed of 5 mm/s is presented in [Figure 12](#). The same figure also presents the curve for the case of a ram speed of 1 mm/s. As noted, the load required to extrude a billet increases with the increase of friction and ram speed. Texture evolution at two different locations at the exit of the die are reported in [Figure 13](#) for the two friction conditions. The main effect of friction is to weaken the texture at the center and to sharpen the texture at the surface. Note that the texture at the center has similar trends but different intensity to that observed from the experiments using a flat die (see [Figure 3](#)). Improvements in the predicted intensity may be obtained by using, among other aspects, the right die geometry (die angle and extrusion ratio), a more realistic mean field hypothesis for low symmetry crystals, different strengths for each slip mode, and adding temperature effects. Current efforts on extrusion modeling using crystal plasticity are focused on these issues.

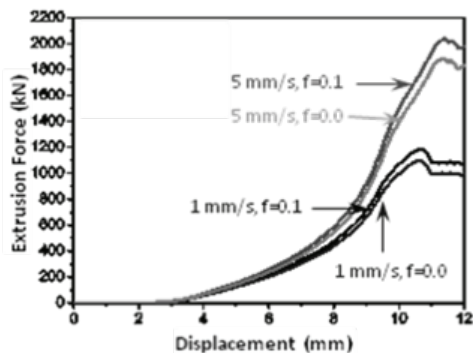


[Figure 12](#): Load-displacement curve for direct extrusion with a 25° streamline die.

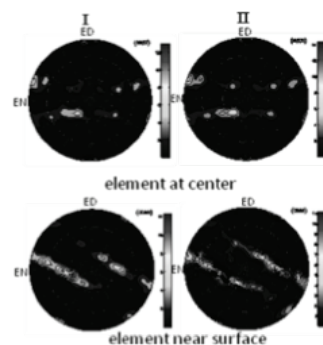


[Figure 13](#): Texture at different locations at the cross section of the extrudate.

Material Modeling and Sheet Forming Simulations of Magnesium Alloys

The objective of the sheet forming work is to develop a physically-based material model and an experimental-validated sheet forming model with corresponding design methodologies to enhance the formability of Mg alloys (AZ31). The current work involves establishing material anisotropy relationships to understand the effects of microstructure state, product geometry and processing parameters on the resulting mechanical properties and distortion of Mg sheets.

Material Model - DMG Production Version 1.0

We are developing an appropriate constitutive model which covers critical features including viscoplasticity, anisotropy, damage, strain sensitivity, temperature dependence, grain size and twinning. Currently, an existing MsSt DMG 1.0 microstructure-plasticity model was calibrated with the material responses of MgAZ31 from uniaxial tensile tests at various strain rates and temperatures (see [Figure 14](#)). This model will be enhanced to include the aforementioned critical features such as twinning. To take advantage of shell elements that have significantly improved numerical run time when compared with 3D elements, the stress integration algorithm was efficiently reformulated in order to take into account of the plane stress condition and implemented in a general finite element code such as ABAQUS.

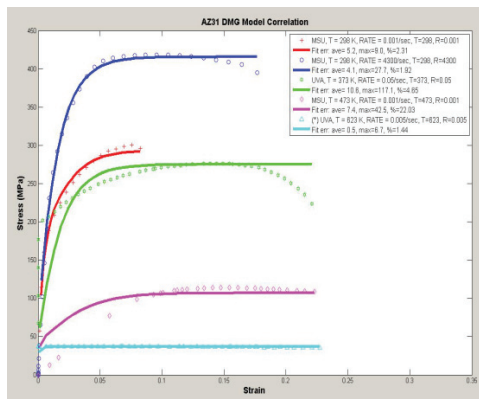


Figure 14: Material fitting of MgAZ31-O with DMG Model.

In this formulation, only the plasticity part of the DMG 1.0 was considered (Bammann et al. (1996), Horstemeyer et al. (2000)). The plasticity model is described by the flow rule

$$\dot{\varepsilon}^p = f(T) \sinh \left[\frac{|\underline{s} - \underline{\alpha}| - \kappa - Y(T)}{V(T)} \right] \text{ and by the kinematic and isotropy hardening evolution equations:}$$

$$\dot{\beta} = \dot{D}^p - [r_d(T) \dot{\varepsilon}^p + r_s(T)] \|\underline{\alpha}\| \underline{\beta} \quad \dot{\varepsilon}_{ss} = \dot{\varepsilon}^p - [R_d(T) \dot{\varepsilon}^p + R_s(T)] \kappa \varepsilon_{ss}$$

$$\text{with } \underline{\alpha} = \frac{2}{3} h(T) \underline{\beta} \quad \text{with } \kappa = H(T) \varepsilon_{ss}$$

where \underline{s} is the deviatoric part of the stress tensor, $\underline{\varepsilon}^p$ the plastic strain tensor, $\underline{\alpha}$ the kinematic hardening and κ the isotropic hardening, $\underline{\beta}$ and ε_{ss} the respective kinematic flux variables, and $f(T)$, $V(T)$, $h(T)$, $H(T)$, $r_d(T)$, $R_d(T)$, $r_s(T)$, and $R_s(T)$ material parameters. The creep plasticity model used by University of Virginia was also implemented as a special case of the DMG plasticity model (no hardening). In this creep-plasticity model, the Zener-Holloman parameter

$$Z = \dot{\varepsilon} \exp(Q/RT) \quad \text{and the Sellars-Tegart Equation} \quad Z = A[\sinh(\alpha\sigma)]^n$$

lead to the plastic flow rule $\dot{\varepsilon}^p = \frac{A}{\exp(Q/RT)} [\sinh \alpha |\underline{s}|]^n$

Sheet Forming Model using DMG 1.0

A forming limit diagram (FLD) provides the maximum strains of sheet metals that can be sustained prior to the onset of localized necking, which is a common failure mode in metal forming. Generally, this failure process is controlled not only by external loading but also by the state of microstructure. The major mechanical material properties controlling the formability of sheet metals are work hardening, rate sensitivity, and plastic anisotropy. To evaluate the mechanical properties of Mg AZ31 alloy including formability, warm forming Finite Element (FE) simulations of magnesium sheets (Figure 15) were performed at various conditions (temperature, tool speed, friction, binding pressure, etc.) using the MsSt DMG 1.0 model. The punch was assumed stationary, while the die moved down after the sheet was clamped with a given binder force, and the sheet was then formed around the stationary punch. The coefficient of friction was set in a range of 0.16 to 0.20. The sheet and die temperatures were kept to be the same, starting at 250°C with an incremental increase of 25°C to 350°C. Regarding the binder pressure, arbitrary values were chosen until actual experimental data will be made available from the forming tests recently conducted by GM. Numerical results will be post-processed (an example is shown in Figure 16), and the prediction of forming limit curves (FLCs) and post-formed stress/strain properties will be evaluated. To include the effect of texture, we used experimental data (Jain et al. (2007)) in conjunction with the Visco-Plastic Self-Consistent (VPSC) model (Lebensohn and Tome (1993)). Figure 17 presents results of AZ31 experimental and simulation stress-strain curves along RD and ND directions based on the Visco-Plastic Self-Consistent (VPSC) model. Using the VPSC code, we first generated the initial and evolving yield surfaces as shown in Figure 18. The next task is to establish a yield surface evolution model from these texture generated yield surface data. The yield surface model will be based on the updated MsSt DMG 1.0 continuum model of anisotropic plasticity.

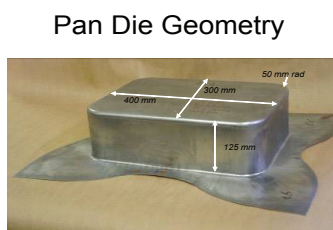


Figure 15: MgAZ31 Warm Forming Pan Geometry for FE Simulations.

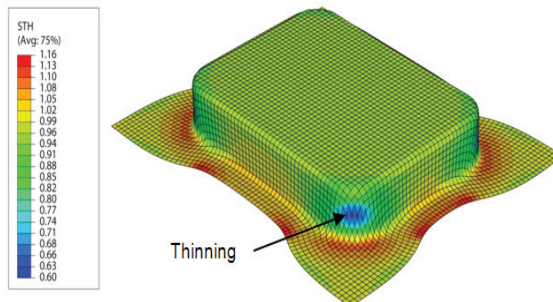


Figure 16: Thickness distribution after warm forming of a pan box

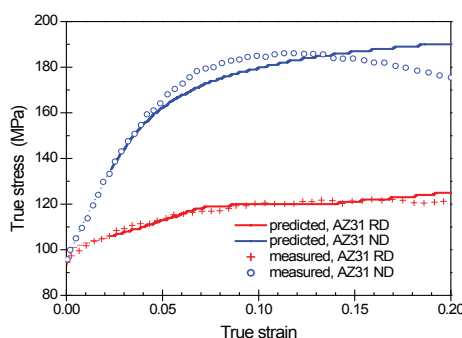


Figure 17: Measured and predicted stress-strain curves of AZ31 sheet compression along RD and ND.

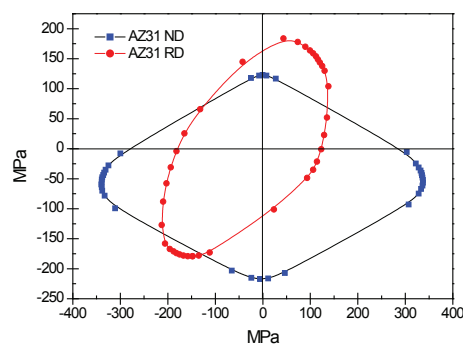


Figure 18: Polycrystal yield surface for AZ31 sheet.

Conclusions

Good progress has been made in both extrusion and sheet areas. Material testing of pre-extruded materials at high temperature and testing of sheet material under warm temperature are in progress and will be reported in the coming reports. In this report, we demonstrated the efforts in both extrusion and sheet processing modeling and experimentation. We have developed and implemented a plane stress form of the MSU DMG 1.0 Plasticity-Damage material model and the Sellars-Tegart material model as requested by customers. We have verified and implemented models by performing sheet metal forming simulations at various temperatures and comparing with available data. We have also designed and developed a lab-scale indirect extrusion fixture. This fixture helps us to perform experiments on Mg AZ61 billets and characterize the deformed microstructure of material. Data generated is being used for validation of numerical simulation tools. We are moving towards our goal of coupled multiscale modeling under uncertainty for design optimization. Predicted initial and evolving yield surfaces of various deformation modes and hardening parameters will be used as input data for large-scale processing models and finite element method (FEM) to predict the property of sheet formed work-piece of AZ31.

Publications

1. Solanki KN, Horstemeyer MF, Steele GW, Hammi Y, Jordon JB. Calibration, validation, and verification including uncertainty of a physically motivated internal state variable plasticity and damage model. *IJSS* 2009; 47(2), 186-203.
2. Bammann DJ, Solanki KN. On kinematic, thermodynamic and coupling of a damage theory for polycrystalline material. *IJP* 2009; DOI: 10.1016/j.ijplas.2009.10.005.
3. Solanki KN, Acar E, Rais-Rohani M, Horstemeyer M, Steele G. Product design optimization with microstructure-property modeling and associated uncertainties. *IJDE* 2009; 1(2):47-79.
4. Solanki KN, Bammann DJ. A thermodynamic framework for a gradient theory of continuum damage. *Acta Mechanica* 2009; DOI 10.1007/s00707-009-0200-5.
5. Acar E, Solanki KN, Rais-Rohani M., and Horstemeyer MF. Stochastic uncertainty analysis of damage evolution computed through microstructure-property relations. *PM*. Accepted (2009).
6. Jordon JB, Horstemeyer MF, Solanki KN, Bernard J, Berry J, Williams TN. Damage characterization and modeling of a 7075-T651 aluminum plate. *MSE A* 2009; 527(1-2):169-78.
7. Rais-Rohani M, Solanki KN, Acar E, Eamon C. Shape and sizing optimization of automotive structures with deterministic and probabilistic design donstraints. *IJVD*. Accepted (2009).
8. Solanki KN, Hammi Y, Bammann D, Horstemeyer MF. Physically motivated internal state variable theory for higher order damage anisotropic of engineering materials. *IJP*. Submitted (2009).
9. Yassar RS, Wang PT, Horstemeyer MF. History effect during sequential rolling process. *Mater Sci Eng A*. Accepted.
10. Yassar RS, Horstemeyer MF, Wang PT, Baird JC, Murphy J, Stolting K. Evolution of in-grain orientation gradient in plastically strained precipitation hardened polycrystals. *Metall Mater Trans A*.

References

1. Bammann DJ, Chiesa ML, Johnson GC. 1996. Modeling large deformation and failure in manufacturing processes. In: Tatsumi T, Watanabe E, Kambe T, eds., *Theoretical and applied mechanics*. London: Elsevier. P. 359-76.
2. CAVS internal report, MSU.CAVS.CMD.2009-R0032.
3. Horstemeyer MF, Lathrop J, Gokhale AM, Dighe M. 2000. Modeling stress state dependent damage evolution in a cast Al-Si-Mg aluminum alloy. *Theo Appl Frac Mech* 33:31-47.
4. Lebensohn RA, Tome CN. 1993. *Acta Materialia* 41:2611.
5. Marin EB. 2006. Sandia National Laboratories, CA; SAND2006-4170.
6. Sellars CM, Tegart WJ. 1967. Relationship between strength and structure in deformation at elevated temperature. *Mem Sci Rev Metall* 63:731-45.
7. Slooff FA, Zhou J, Duszczyk J, Katgerman L. 2008. Strain-dependent constitutive analysis of three wrought Mg-Al-Zn alloys. *J Mater Sci* 48:7165-70.

H. Materials Design for Mg Alloys

Principal Investigator: Seong-Gon Kim
Associate Professor
Department of Physics and Astronomy; Hilbun Hall, Rm 237
Mississippi State University, P.O. Box 5405
Mississippi State, MS 39762-5405
(662)325-8031; email: kimsg@hpc.msstate.edu

Principal Investigator: Mark F. Horstemeyer:
Center for Advanced Vehicular Systems (CAVS) Chair in Solid Mechanics & Professor
Department of Mechanical Engineering
Mississippi State University; 206 Carpenter Bldg., PO Box ME
Mississippi State, MS 39762
(662) 325-7308; email: mfhorst@me.msstate.edu

Co-Principal Investigator: Hongjoo Rhee
Postdoctoral Associate; CAVS
Mississippi State University, P.O. Box 5405
Mississippi State, MS 39762-5405
(662)325-9221; email: hrhee@cavs.msstate.edu

Co-Principal Investigator: Sungho Kim
Postdoctoral Associate; CAVS, CAVS 2182-C
Mississippi State University
Mississippi State, MS 39762-5405
(662) 325-9241; email: sk5@msstate.edu

Co-Principal Investigator: Greg Olson
Winson-Cook Chaired Professor in Engineering Design
The Steel Research Group at Northwestern
Northwestern University; Department of Mechanical Engineering
2145 Sheridan Road
Evanston, IL 60208-3111
(847) 491-2847; email: g-olson@northwestern.edu

Co-Principal Investigator: Shengjun (Dennis) Zhang:
Postdoctoral Associate; Department of Material Science and Engineering
Robert R. McCormick School of Engineering and Applied Science
Northwestern University
2220 Campus Dr.
Evanston, IL 60208-3108, USA
(847) 491-5887; email: shengjun-zhang@northwestern.edu

Co-Principal Investigator: Qingyou Han
Purdue University
Mechanical Engineering Technology Department
401 North Grant Street
Knoy Hall - Room 107
West Lafayette, IN 47907-2021
(765) 494-7528; email: hanq@purdue.edu

Technology Area Development Manager: William Joost
(202) 287-6020; e-mail: william.joost@ee.doe.gov

Contractor: Mississippi State University
Contract No.: 4000054701

Objective

Investigate the effect of nanoscale precipitates and novel additives to the overall strength and ductility in Mg alloy systems.

Approach

In support of the collaborative materials design effort proposed here aimed at lightweight components for automotive applications, a systems approach to materials design [Olso98] will be applied. Working within a multiscale hierarchy of microstructural subsystems governing desired property combinations for structural performance, key microstructural elements will be identified for the calibration, application, and validation of process/structure and structure/property design models defining key theoretical parameters and critical experiments enabling parametric design of novel alloy compositions.

At electronic level, quantum mechanical first-principles simulations based on Density Functional Theory (DFT) [Kres96] will be performed to elucidate the origin of the alloying effects. A fundamental understanding of solidification, dislocation, creep, fatigue, crack nucleation and failure of Mg-based alloy systems also requires accurate atomistic modeling of nanoscale systems containing up to hundreds of thousand atoms. We will perform large scale atomistic simulations using efficient and reliable empirical interatomic potential methods such as the Modified Embedded Atom Method (MEAM) [Bask92] and force-matching-embedded-atom-method (FMEAM) potentials.

Various state-of-the-art experimental techniques will also be employed in this project. Scanning electron microscopy (SEM) and transmission electron microscopy (TEM) will be used to obtain microscale as well as nanoscale structural information of Mg alloys. The structure and energies of dislocation cores and planar defects, including stacking faults and twin boundaries, determine the mechanical behavior of the Mg alloys. Electron backscatter diffraction (EBSD) and X-ray diffraction (XRD) measurements will be used to keep track of texture evolution during deformation. An in-situ chemical analysis and mapping of alloying elements can be used to keep track of these elements. Three-dimensional atom probe (3DAP) is capable of resolving the chemical identity and position of individual atoms in 3D with atomic resolution in the z-direction and sub-nanometer resolution in the lateral direction. Furthermore, fundamental thermo-mechanical experiments to measure creep resistance and ductility will be carried out under various loading conditions. Experimental failure analysis will be performed to understand the microstructure driven mechanism of plasticity and damage growth under monotonic and cyclic loadings. X-ray computed tomography (CT) will be used to quantify in three-dimension morphological and topological evolutions of voids and relevant microstructural features to material damage. Depth-sensoring microindenter, and nanoindenter will also be used to evaluate the micromechanical properties of each microstructural phase present in the Mg alloys. These measurements will be used to validate and, in turn, guide the computational material design of new Mg alloys.

Accomplishments

The objectives for the project were met by accomplishing the following:

- Mg alloys AM50B, AM60B, and AE44 have been cast at ORNL by Qingyou Han (now at Purdue) as the base alloys for the project.
- The nanostructure of an experimental, low-melting-point prototype ZA73 alloy (Mg-7Zn-3Al) was characterized by 3D atom-probe microanalysis in a local-electrode atom probe (LEAP). The strengthening phase composition was consistent with the ternary phase, including metastable compositions. The experimental results are available as a preprint: Shengjun Zhang and Gregory B. Olson, 3D-atom probe investigation of strengthening precipitates in a Mg-7Zn-3Al alloy, preprint.
- The MEAM potentials for Mg-Al alloys have been developed. The potential parameters and validation data have been published in: B. Jelinek, J. Houze, Sungho Kim, M. F. Horstemeyer, M. I. Baskes, Seong-Gon Kim, “Modified embedded-atom method interatomic potentials for the Mg-Al alloy system”, Phys. Rev. B, vol. 75, pp. 054106 (2007).
- A multi-objective optimization methodology to construct empirical interatomic potentials with minimal manual fitting has been developed and applied to construct a new MEAM interatomic potential for Mg. The new methodology and its application to Mg potential along with its validation data have been published in: Seong-Gon Kim, M. F. Horstemeyer, M. I. Baskes, Masoud Rais-Rohani, Sungho Kim, B. Jelinek, J. Houze, Amitava Moitra, and Laalitha Liyanage, “Semi-empirical Potential Methods for Atomistic Simulations of Metals and Their Construction Procedures,” J. Eng. Mater. Technol., 131 (4), 041210 [9 pages] (2009).
- A new Zn FMEAM potential has been developed using the multi-objective optimization method. The potential parameters and validation data have been compiled into a manuscript for publication: Amitava Moitra, J. Houze, Sungho Kim, B. Jelinek, Laalitha Liyanage, M. F. Horstemeyer, and Seong-Gon Kim, “Force-matching embedded-atom-method potential for Zinc”, to be submitted to Phys. Rev. B.
- A new Mg-Zn FMEAM potential has been developed using the multi-objective optimization method. The potential is being applied to study the adsorption of Mg atom on Zn surfaces and vice versa to be published in a peer-reviewed journal: Amitava Moitra, Sungho Kim, M. F. Horstemeyer, and Seong-Gon Kim, “Adsorption of Zn atoms on Mg (0001) surface”, in preparation.
- First-principles calculation of the crystal structure of phase in Mg-Zn-Al casting alloys has been performed. The results have been compiled into a manuscript for publication: J. Houze, Amitava Moitra, Sungho Kim, M. F. Horstemeyer, and Seong-Gon Kim, “First-principles calculation of the crystal structure of Phi-phase in Mg-Zn-Al casting alloys”, in preparation.
- Materials/mechanical properties characterization has been performed on the die-cast base-alloys (AZ91D, AM50A, AM60B, and AE44) to provide information for design and simulation efforts: Chemical analysis using a spectrometer; microstructure observation using optical & scanning electron microscopes; nano- & micro-indentation tests; room temperature tensile tests at different strain rates; elevated temperature tensile tests; creep tests by using ORNL facilities.
- Using 3D-atom probe, the strengthening precipitates in a Mg-7Zn-3Al alloy at peak hardness have been investigated. The chemical compositions of the matrix and precipitates were measured by local-electrode atom probe (LEAP) spectrometry and compared with the results calculated by the Thermo-Calc software based on the COST2 database. Ternary nano-sized precipitates have been found. The precipitates have compositions consistent with the ternary or phase including its metastable extension. The equivalent sphere

diameter of the precipitates at peak strengthening is measured as 20-50 nm, providing an important strength model calibration for materials design. The experimental results are available as a preprint: Shengjun Zhang and Gregory B. Olson, 3D-atom probe investigation of strengthening precipitates in an Mg-7Zn-3Al alloy, preprint.

Introduction

Magnesium alloys are currently used in relatively small quantities for automotive components, generally limited to die castings. Two main barriers to wider impact of Mg alloys to automotive industry are poor creep resistance at temperatures above 150 °C for power train applications and poor ductility for structural body parts, engine components, engine cradle and control arms.

To achieve the goal of improving the fuel efficiency of the cars built in the future, the automobile industry needs to have Mg-alloy, light-weight, high-strength materials with better materials properties. We need to perform compositional design of Mg-based alloys in a manner that increases creep resistance and ductility while keeping production cost low.

The future state of this technology will be the development of Mg-based alloys that have lower mass densities and increased strength compared to aluminum-based alloys, and have better creep resistance than that of AE44 grade Mg alloy and cost comparable to that of AZ19D grade Mg alloy. The new Mg-based alloys should also exhibit sufficiently high ductility to allow conventional fabrication process to be used, but generate adequate strength after the fabrication process.

Approach

In support of the collaborative materials design effort proposed here aimed at lightweight components for automotive applications, a systems approach to materials design [Olso00] will be applied. Working within a multiscale hierarchy of microstructural subsystems governing desired property combinations for structural performance, key microstructural elements will be identified for the calibration, application, and validation of process/structure and structure/property design models defining key theoretical parameters and critical experiments enabling parametric design of novel alloy compositions.

We use a hierarchical, multiscale methodology to investigate the effect of nanoscale precipitates and additives to the overall strength and ductility in Mg-based alloy design for automotive applications. In a hierarchical multiscale framework, numerical methods are run independently at disparate length scales. Then, a bridging methodology such as statistical analysis methods, homogenization techniques, or optimization methods are used to distinguish the pertinent cause-effect relations at the lower scale to determine the relevant effects for the next higher scale [E03]. One effective hierarchical method for multiscale bridging is the use of thermodynamically-constrained internal state variables (ISVs) that are physically based on microstructure-property relations [Espi01, Gail02]. We will adopt the strategy developed by Horstemeyer and his co-workers who used ISVs as a top-down hierarchical approach to bring the pertinent nanoscale, microscale, and mesoscale phenomena into the macroscale [Hors03, Olso00, Hao04].

At the electronic level, quantum-mechanical, first-principles total-energy calculations are performed within the Density Functional Theory (DFT) [Kres96] using Blöchl's all-electron projector augmented wave (PAW) method [Bloc94] as implemented by Kresse et al. [Kres99]. For the treatment of electron exchange and correlation, we use either the local density approximation (LDA) [Perd81] or the generalized gradient approximation (GGA) [Perd96] depending on the accuracy required.

At the atomistic level, accurate atomistic simulations are performed using efficient and reliable empirical interatomic potentials such as the embedded-atom method (EAM) [Daw84], the modified-embedded-atom-method (MEAM) [Bask92] or force-matching-embedded-atom-method (FMEAM) [Li03] potentials. The interatomic potentials are constructed by optimizing the potential parameters to reproduce various experimental materials properties and atomic force data from DFT calculations.

Various state-of-the-art experimental techniques are employed in this project. The chemical analysis is performed by using a spectrometer. Microstructures of the alloys are investigated by an optical microscope (OM) and a scanning electron microscope (SEM). SEM and transmission electron microscopy (TEM) are used to obtain microscale as well as nanoscale structural information of Mg alloys. Electron backscatter diffraction (EBSD) and X-ray diffraction (XRD) measurements are used to keep track of texture evolution during deformation. The quantitative as well as qualitative chemical compositions of each phase present in the alloys will be individually analyzed by an energy dispersive x-ray (EDX) spectroscopy technique. An *in-situ* chemical analysis and mapping of alloying elements can be used to keep track of these elements. Three-dimensional atom probe (3DAP) is capable of resolving the chemical identity and position of individual atoms in 3D with atomic resolution in the z-direction and sub-nanometer resolution in the lateral direction. Conventional hardness tests will be conducted to gain overall properties of the alloys, while depth-sensoring micro-indentation and nano-indentation tests (NITs) are performed to obtain micromechanical properties of each microstructural phase present in Mg alloys. Thermo-mechanical experiments to evaluate creep resistance and ductility are carried out under various conditions. An X-ray computed tomography (CT) will be used before and after the creep tests to quantify the three-dimensional morphological and topological evolutions of voids and microstructural features relevant to material damage. Experimental failure analysis will be performed to understand the microstructure-driven mechanism of plasticity and damage growth under monotonic and cyclic loadings.

Empirical Interatomic Potentials

To meet the industrial demand for high-strength, lightweight Mg alloys, it is essential to obtain detailed understanding of the effect of individual alloying elements on the properties of Mg alloys. The alloying elements can form interstitial or substitutional defects, or can precipitate into small particles creating complex interface structures. The interactions between these alloying elements need to be investigated using atomistic simulation techniques such as molecular dynamics (MD) or Monte Carlo simulations. These atomistic simulations require accurate atomic interaction potentials to compute the total energy of the system. First-principles calculations certainly can provide the most reliable interatomic potentials. However, realistic simulations of alloy systems often require a number of atoms that renders these methods impractical – they either require too much computer memory or take too long to be completed in a reasonable amount of time. One alternative is to use empirical interatomic potentials that can be evaluated efficiently, so that the atomistic approaches that use them can, in certain cases, handle systems with more than a million atoms.

There are two additional essential features that are expected from a useful empirical approach besides its efficiency: reliability and flexibility. A reliable interatomic potential would accurately reproduce various fundamental physical properties of the relevant element or alloy, such as elastic, structural, and thermal properties. Reliability also includes transferability. A transferable interatomic potential would perform reasonably well even under circumstances that were not used during its construction phase. A flexible empirical approach can represent interaction potentials among a wide variety of elements and their alloys using a common mathematical formalism.

Mg and Al Interatomic Potentials

The multi-objective optimization (MOO) procedure was applied to develop a new interatomic potential for Mg based on MEAM [Jelin07, Kim09]. To validate the transferability of our new MEAM potential, we calculated the cohesive energies of Mg atoms in three common configurations, namely, hcp, fcc, and bcc crystal structures, as a function of the atomic volume. The results are summarized in Figure 1(a). Our results show that the new MEAM potential for Mg atoms correctly predicts the order of stability among these common structures. In addition, the differences in equilibrium cohesive energies among these configurations are reasonably close to those of DFT calculations.

We also applied the MOO procedure to develop a new interatomic potential for Al based on the MEAM. We used the previously published Al MEAM potentials by Baskes [Bask92] as the initial set of the parameters for our MOO procedure. To test the validity of this new Al MEAM potential, we computed the atomic energy of Al atoms in four common configurations, namely fcc, hcp, bcc, and simple cubic (sc) crystal structures, as a function of the atomic volume. The results are summarized in Figure 1(b). As expected, the curve for the fcc structure produced by the MEAM potential retraces the results of DFT calculations nearly perfectly since fcc was used as the reference structure during the potential construction process. The agreement between the MEAM potential and DFT for the hcp structure is also remarkable. The most important result, however, is the fact that the new MEAM potential correctly identified fcc as the most stable structure for Al. Furthermore, the sequence of the structures is correctly predicted in the order of stability by the Al MEAM potential. The relative cohesive energies, with respect to the one for the fcc structure, are also in good agreement with the DFT calculations, although the result for the simple cubic structure is slightly underestimated. The relative equilibrium atomic volumes, with respect to the one for the fcc structure, are also well reproduced.

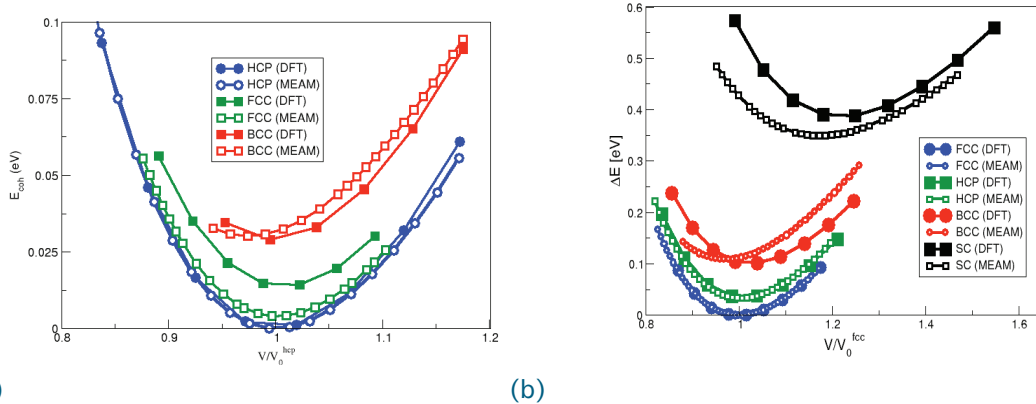


Fig. 1. The cohesive energies of Mg atoms in various crystal structures as a function of the atomic volume: (a) Mg, (b) Al atoms. The energies are measured from the equilibrium atomic energy of fcc structure.

Mg-Al Alloy Interatomic Potential

Based on interatomic potentials for Mg and Al atoms, we developed a new interatomic potential for Mg-Al alloy system based on the MEAM by applying the MOO procedure. We used the previously-published MEAM potentials for Mg-Al alloys by Baskes [Bask92] as the initial set of the parameters for our MOO procedure. To test the validity of this new MEAM potential for Mg-Al alloy system, we computed the heat of formation per atom for different configurations. Figure 2(a) shows the heat of formation per atom for the $B1$, $B2$, and $B3$ structures compared with the results from the DFT calculations. The $B1$ (cubic rocksalt) structure was used as the reference structure for the Mg-Al alloy MEAM potential. Fig. 2(a) shows that the sequence of the structures in the order of stability is predicted correctly by the MEAM potential for the Mg-Al alloy system. The relative cohesive energies, with respect to the one for the reference

structure, are also in good agreement with the DFT calculations. The equilibrium atomic volume and bulk modulus of Mg-Al in the *B1* structure are reproduced almost exactly.

To further demonstrate the validity of our potentials, we computed the heat of formation per atom for many intermetallic phases of Mg-Al alloys. The total energy values of $B1$, $B2$, $B3$, $C1$, $C3$, $C9$, $C15$, $D03$, $D09$, $A15$, $L12$, and $A12$ structures were evaluated at the optimal atomic volume for each structure. The results from the MEAM calculations, compared with the ones from the DFT calculations, are summarized in Figure 2(b). Although the Mg and Al atoms in these intermetallic phases are in a chemical environment very different from the one in the reference structure ($B1$), the agreement between MEAM and DFT is quite satisfactory. In most cases, MEAM preserves the order of stability predicted by DFT. The differences in the heat of formation per atom from MEAM and DFT are less than 0.5 eV at most. However, we note that the MEAM failed to predict that the formation of one of the experimentally-observed Mg-Al alloy structures [Sing03, Okam98], $\gamma(\text{Mg}_{17}\text{Al}_{12})$, denoted as the $A12$ structure in Figure 2(b), as an exothermic process. In comparison, our DFT calculation correctly predicted the H_f for this structure to be a negative value (-0.017 eV).

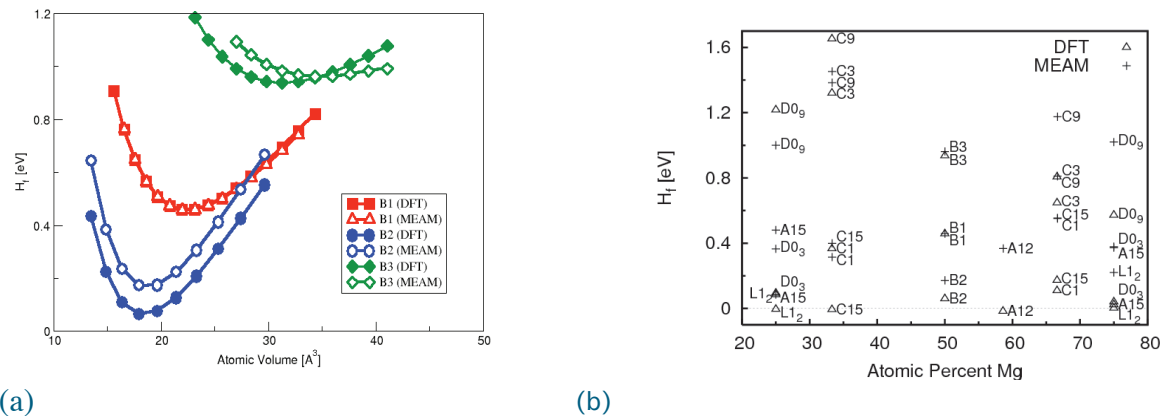


Fig. 2. (a) The heat of formation per atom for Mg-Al alloys in the B1, B2, and B3 crystal structures. (b) The heat of formation per atom for Mg-Al alloys in various intermetallic phases with different stoichiometric coefficients. The results obtained from the Mg-Al MEAM potentials are compared with the DFT calculations. The structure names are written next to the symbols (open triangles for DFT and crosses for MEAM).

Precipitates in ZA73 Mg alloy

While typical Mg-Al-Zn casting alloys such as AZ91 are Al-rich, Zn-rich alloys associated with the Zn-rich lower ternary eutectic can provide low-melting compositions with the potential for greater precipitation strengthening. A previous study demonstrated that a MgZnAl aged to peak hardness at 150°C for 100 hrs could reach a yield strength of 190 MPa [Shia06]. While details of precipitation strengthening in MgAlZn alloys are not well known, the precipitation strengthening in binary MgZn alloys has been well studied. The precipitation sequence in Mg-Zn is well documented starting from Guinier-Preston (GP) zone formation, followed by the formation of B₁ and B₂ metastable precipitates before reaching the formation of equilibrium β phase [Wei95]. In the present work, the precipitates in a Mg-7Zn-3Al (in wt. %) alloy aged to peak hardness at 150°C have been characterized by 3DAP microanalysis as the basis for calibration of precipitation-strengthening models for alloys design. A ZA73 alloy (Mg-7Zn-3Al) was induction-melted under an Ar atmosphere and cast into ingots. The samples were encapsulated together in a pyrex tube in vacuum to prevent oxidation of the Mg and then backfilled with argon to prevent vaporization of the Zn. These samples were heated in a furnace at a solution treatment temperature of 358 °C for 24 hours and then quenched in oil to retain a super-saturated solid solution. Samples were then encapsulated individually and aged in a furnace for 100 hours at 150 °C corresponding to the peak hardness conditions identified in a previous study [Shia06].

In order to analyze the microstructure of these nanoscale precipitates, 3DAP tomography was employed. Atom-probe tomography utilizes a combination of time-of-flight mass spectrometry and point-projection microscopy to chemically identify and locate individual atoms within a bulk sample. Atom-probe specimens are needles or tips sharpened to less than 100 nm in diameter. A positive voltage pulse is applied to the sharpened tip, causing field evaporation of positively-charged metal ions that are subsequently drawn to a detector plate along a voltage differential. The chemical identity of each ion is revealed through the mass-to-charge ratio as determined by the time-of-flight between the applied pulse and point of detection. The x and y coordinate of each ion within the sample is then determined from the point of impact on the two-dimensional (2D) detector, and the depth (or z coordinate) is determined by the sequence number or absolute time of impact.

For this research, a new generation atom probe is employed termed a local-electrode atom probe (LEAP™). Atom-probe tomography was performed using a LEAP™ 3000 tomograph manufactured by Imago Scientific Instruments Corporation in Madison, WI. Analyses were performed after cooling specimens to a temperature of 40 K to minimize atomic motion while under ultra-high vacuum (residual pressure $< 10^{-8}$ Pa). Field evaporation of atoms from the specimen tip was achieved through applied high-voltage pulses at a frequency of 200 kHz. Voltage is applied to the specimen tip through a standing direct-current (DC) voltage with voltage pulses applied through the extraction electrode at a pulse-to-DC voltage ratio of 15%. The voltage levels required for field evaporation are dependent on the radius of curvature of each specimen tip, with the standing DC voltage ranging from 500 V for very sharp tips (diameter < 10 nm) to 15,000 V for larger tips (~ 100 nm diameter). Steady field evaporation rates of 400-10,000 atoms/second were maintained through software-controlled manipulation of the voltage levels, with applied voltage steadily increased to account for tip blunting with continued specimen evaporation.

Figure 3(a) displays LEAP tomographic reconstructions for the ZA73 alloy aged at 423 K for 100 hours using the voltage mode. Compared with the bulk alloy composition, a good agreement has been obtained in the Zn content. A proximity histogram (proxigram) showing the concentration of Mg, Zn, Al and Ca as a function of radial distance from the precipitate interface is also presented in **Figure 3(b)**. It is apparent that both Zn and Al partition to the precipitates. The Zn and Al contents are very low in the matrix. The approximate chemical compositions of the matrix and the precipitates can be read in this proximity diagram.

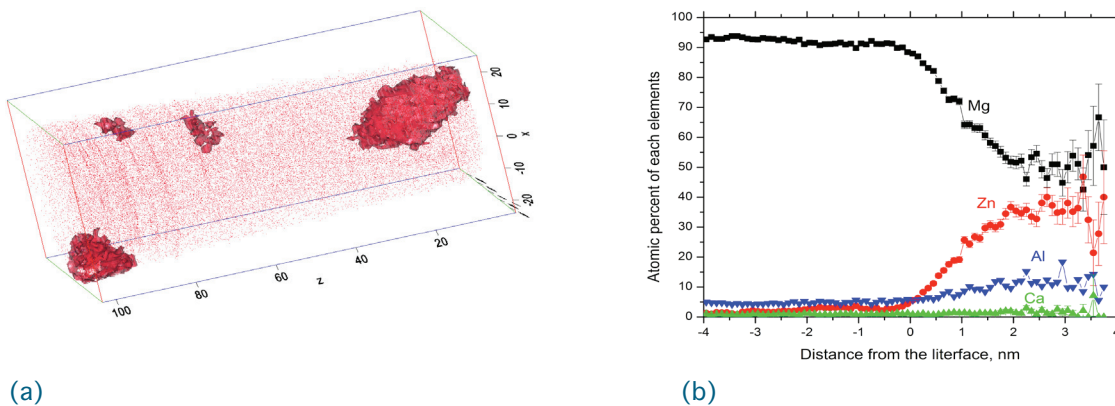


Fig. 3. (a) LEAP tomographic reconstructions of 5 % Zn isoconcentration surfaces for the ZA73 alloy aged at 423 K for 100 hours using the voltage mode. (b) Proximity histogram for the LEAP tomographic reconstructions of (a) showing the average concentration of Mg, Al, Zn and Ca as a function of distance from the Mg-Zn-Al ternary heterophase interface, as defined by a 5 at. % Zn isoconcentration surface.

Mg-Zn-Al ternary phase structure

The structure of $\text{Mg}_{84}(\text{Al}_x\text{Zn}_{1-x})_{68}$ alloy in ternary φ phase has been determined from the first-principles calculations. Bourgeois et al. characterized the crystal structure of the equilibrium intermetallic φ phase formed in a Mg-Zn-Al casting alloy from electron diffraction patterns obtained using transmission electron microscopy (TEM) [Bour01]. Despite these experiments and a few simulations to reproduce the diffraction patterns, the equilibrium structure of φ phase in a Mg-Zn-Al casting alloy is not fully determined and the identity of some of the ambiguous sites are yet to be determined [Lian98]. For the first time, we obtained the equilibrium structure and determined the identity of all atomic sites of φ phase based on DFT. The structure and identity of atoms are determined by minimizing the heat of formation of $\text{Mg}_{84}(\text{Al}_x\text{Zn}_{1-x})_{68}$ alloy as a function of x . There are 10 sites where Al and Zn atoms can occupy interchangeably. Figure 4(a) shows the heat of formation values obtained for all possible ($2^{10} = 1024$) combinations. Figure 4(b) shows the structure of $\text{Mg}_{84}(\text{Al}_x\text{Zn}_{1-x})_{68}$ alloy in φ phase with $x = 0.4725$ that has the lowest heat of formation in Figure 4(a).

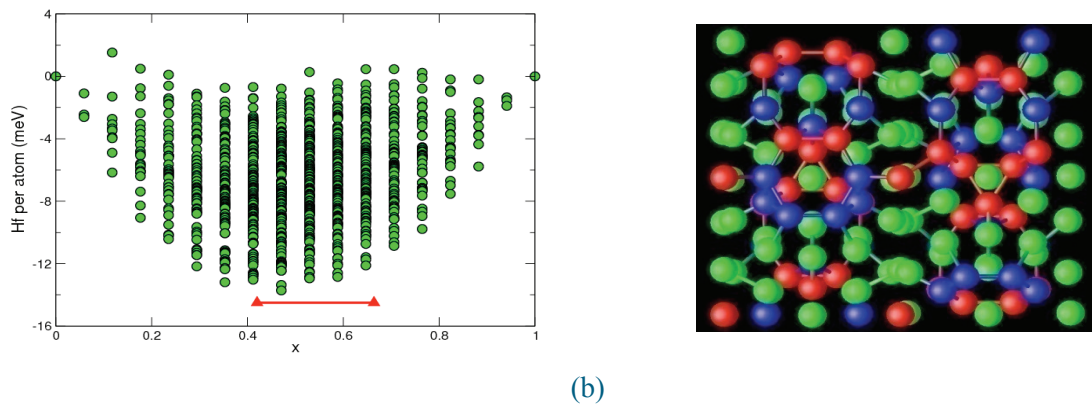


Fig. 4. (a) The heat of formation per atom of $\text{Mg}_{84}(\text{Al}_x\text{Zn}_{1-x})_{68}$ alloy as a function of x . The red line indicates the range of x values consistent with previous experiments [Bour01]. (b) The structure of $\text{Mg}_{84}(\text{Al}_x\text{Zn}_{1-x})_{68}$ alloy in φ phase with $x = 0.4705$. The green spheres represent Mg atoms, blue spheres Zn atoms, and red spheres Al atoms.

Mechanical Properties of Mg-based Alloys

In order to obtain fundamental mechanical properties and attain proper stress levels for creep tests, tensile tests were carried out in the quasi-static strain rate regime. The tensile tests were performed at various strain rates of 0.0001, 0.001, and 0.01/s with different testing temperatures: the room temperature and 150° C. The stress versus strain plots of the various base-alloys under such test conditions are shown in Figure 5. The ultimate tensile stress and the flow stress level of the alloys strongly depend on the alloy composition, testing temperature, and strain rate. Not surprisingly, AZ91D possessed the highest tensile strength and the worst ductility among tested alloys. AM series Mg alloys are developed for and characterized by slightly reduced strengths with higher ductility and impact strength compared to AZ91D grade [Sun07]; while AE series Mg alloys are developed for good ambient and elevated temperature properties and creep resistance [Anya04].

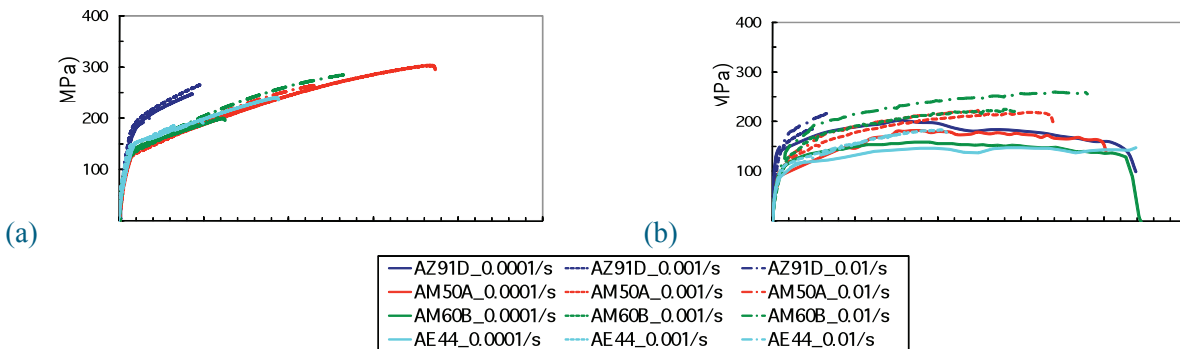


Fig. 5. Stress versus strain plots of the Mg-based alloys obtained from quasi-static tensile tests at (a) room temperature and (b) 150°C.

Figure 6 provides fracture surfaces of the tensile tested specimens observed by an SEM. The fractography reveals that fractures occurred in a brittle manner in all cases. The absence of shear lips on the edges of fracture surfaces, indicating a general lack of ductility, is noted. The features of the fracture surfaces are associated with shrinkage cavities. Fracture surfaces contained many pores ranging from a few tens of microns to hundred microns in size. These cavities could have resulted from entrapped air being carried into the mold by undue turbulence during casting. In addition, granular secondary arms of dendrites can be seen on the fracture surfaces.

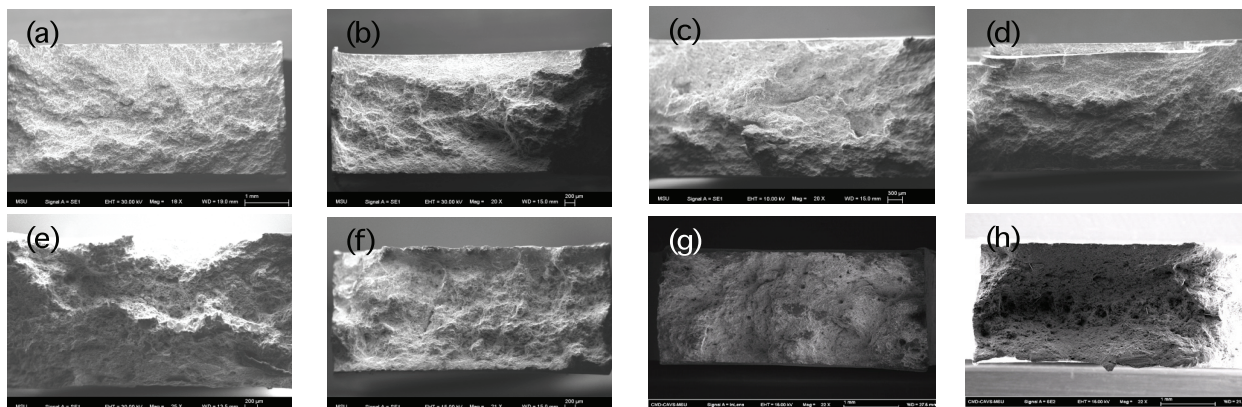


Figure 6. SEM fractography on the tensile tested specimens; (a) AZ91D, (b) AM50A, (c) AM60B, and (d) AE44 tested at room temperature; (e) AZ91D, (f) AM50A, (g) AM60B, and (h) AE44 tested at 150°C.

The creep behaviors of the base-alloys were investigated to determine better ways for developing novel Mg alloys with improved creep resistance. Two experimental approaches, stress relaxation and creep tests, were used to obtain creep properties of the base-alloys. The stress relaxation tests were carried out on an Instron machine at various temperatures (120, 150, and 200°C) after imposing pre-strain of 0.02 and pre-strain rate of 0.001/s prior to the stress relaxation process. Stress versus time plots of the base-alloys obtained from the stress relaxation tests are given in Figure 7. For a given test condition, the peak stress obtained from AZ91D prior to the stress relaxation tests is the highest among tested alloys and this result is comparable to tensile test results. The peak stress and residual stress levels decrease with increasing testing temperature for any given test conditions.

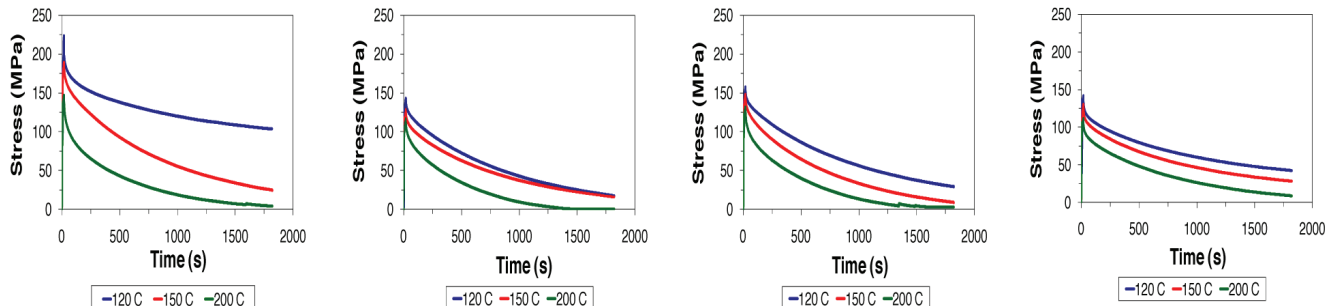


Figure 7. Stress versus time plots obtained from stress relaxation tests at various temperatures: (a) AZ91D, (b) AM50A, (c) AM60B, and (d) AE44.

Creep test results obtained from ORNL creep test facilities are shown in **Figure 8**. Creep tests were performed at three different temperatures of 120, 150, and 200 °C with three different stress levels of 20, 40, and 80 MPa. Four creep tests (two low stress tests at 120 and 150°C) for AZ91D were discontinued after 500 hours of testing since the apparent steady state condition were achieved; whereas six tests were discontinued for AE44 creep tests because no detectable creep deformation was observed under such test conditions.

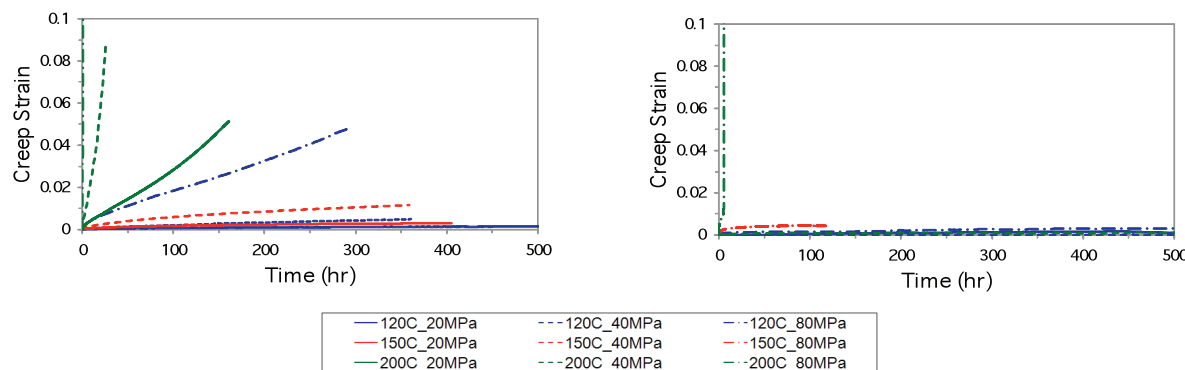


Figure 8. Creep curves obtained from ORNL creep test facilities under various test conditions: (a) AZ91D and (b) AE44.

Summary

The main goal of this project is to understand the effect of nanoscale precipitates and novel additives to the overall strength and ductility of Mg alloys. We developed a new multi-objective optimization (MOO) methodology as a robust procedure to construct reliable and transferable interatomic potentials for Mg-based alloy systems. This MOO procedure was applied to construct transferrable interatomic potentials for Mg and Al atoms using the Modified Embedded Atom Method (MEAM). We also applied the MOO procedure to develop new interatomic potentials for Mg-Zn alloys. We established a basic framework for the accelerated development of reliable and efficient interatomic potentials for other combinations of alloy systems to perform large-scale, realistic atomistic simulations.

The nanostructure of strengthening precipitates in a ZA73 Mg-alloy aged to peak hardness at 423 K for 100 hrs was investigated. The chemical compositions of the alloys as well as the matrix and the precipitates were measured by local-electrode atom probe (LEAP) spectrometry and compared with the results calculated by the Thermo-Calc software based on the COST2 database. Ternary nano-sized precipitates have been found to have the compositions consistent with the ternary φ phase including its metastable extension. The precipitate size at peak hardness corresponds to an equivalent sphere diameter of 20 – 50 nm. The structure of $Mg_{84}(Al_xZn_{1-x})_{68}$ alloy in ternary φ phase has been determined from the first-principles calculations. The creep

behavior of the Mg-based alloys was investigated using stress relaxation and long-time creep tests. We found that steady-state creep rate of AZ91D is much higher than that of AE44 and the rupture lifetime of AE44 is dramatically longer than that of AZ91D.

The strengthening mechanisms of the Mg-based alloy systems were investigated. The metastable phase diagrams with Guinier-Preston (GP) solvus and metastable precipitate solvus have been constructed. Preliminary time-temperature transformation (TTT) diagrams of Mg-based alloys have been estimated according to experimental information. These diagrams provide the basis for calibration of thermodynamic and kinetic modeling of precipitation strengthening in the Mg-based alloy systems.

Presentations/Publications/Patents

1. B. Jelinek, J. Houze, Sungho Kim, M. F. Horstemeyer, M. I. Baskes, and Seong-Gon Kim, “*Modified embedded-atom method interatomic potentials for the Mg-Al alloy system*”, Phys. Rev. B, **75**, 054106 (2007).
2. Seong-Gon Kim, M. F. Horstemeyer, M. I. Baskes, Masoud Rais-Rohani, Sungho Kim, B. Jelinek, J. Houze, Amitava Moitra, and Laalitha Liyanage, “*Semi-empirical Potential Methods for Atomistic Simulations of Metals and Their Construction Procedures*,” J. Eng. Mater. Technol., **131** (4), 041210 [9 pages] (2009).
3. Shengjun Zhang and Gregory B. Olson, “*3D-atom probe investigation of strengthening precipitates in a Mg-7Zn-3Al alloy*”, Preprint.
4. S. Groh, B. Jelinek, J. Houze, Seong-Gon Kim, M. F. Horstemeyer, “*Mobility of $\langle a \rangle$ dislocations in Mg and Mg/Al alloys by molecular dynamic simulations*”, submitted to Computational Materials Science.
5. Amitava Moitra, J. Houze, Sungho Kim, B. Jelinek, Laalitha Liyanage, M. F. Horstemeyer, and Seong-Gon Kim, “*Force-matching embedded-atom-method potential for Zinc*”, to be submitted to Phys. Rev. B.
6. Amitava Moitra, Sungho Kim, M. F. Horstemeyer, and Seong-Gon Kim, “*Adsorption of Zn atoms on Mg(0001) surface*”, in preparation.
7. J. Houze, Amitava Moitra, Sungho Kim, M. F. Horstemeyer, and Seong-Gon Kim, “*First-principles calculation of the crystal structure of Phi phase in Mg-Zn-Al casting alloys*”, in preparation.
8. Bohumir Jelinek, Sungho Kim, Jeffery Houze, Seong-Gon Kim, M. F. Horstemeyer, and M. I. Baskes, “*Development and testing of MEAM Potentials for Al-Mg Alloys*”, APS 2006 SESAPS Meeting, Williamsburg, VA, November 2006.
9. Shengjun Zhang and Gregory B. Olson, “*Local-Electrode Atom-Probe Tomographic Investigation of strengthening Precipitates in a Mg-7Zn-3Al Alloy at Peak Hardness*”, Mg Technology 2008 proceeding of TMS 2008.
10. Seong-Gon Kim, “*Materials Design for Mg alloys by Multiscale Modeling*”, Colloquium, Pusan National University, Pusan, KOREA, July 16, 2008.
11. Seong-Gon Kim, M. F. Horstemeyer, M. I. Baskes, Masoud Rais-Rohani, Sungho Kim, B. Jelinek, J. Houze, Amitava Moitra, and Laalitha Liyanage, “*Semi-empirical Potential Methods for Atomistic Simulations of Metals and Their Construction Procedures*,” accepted for publication in Journal of Engineering Materials and Technology.

- 12.Jeffrey Houze, Bohumir Jelinek, Sungho Kim, Seong-Gon Kim, Mark Horstemeyer, "Verification and refinement of the Al-Mg-Zn Φ phase crystal structure model," APS 2009 March meeting, Pittsburgh, PA, Mar. 16-20, 2009.
- 13.Laalitha Liyanage, Jeffrey Houze, Sungho Kim, Mark Horstemeyer, Seong-Gon Kim, "An *ab initio* study of the crystal structure of the Tau-phase in Al-Mg-Zn alloys," APS 2009 March meeting, Pittsburgh, PA, Mar. 16-20, 2009.

References

1. [Any04] I.A. Anyanwu, Y. Gokan, A. Suzuki, S. Kamado, Y. Kojima, S. Takeda, T. Ishida, "Effect of substituting cerium rich mischmetal with lanthanum on high temperature properties of die-cast Mg-Zn-Al-Ca-RE alloys", Mater. Sci. Eng., A **380**, 93 (2004).
2. [Bask92] M. I. Baskes, "Modified embedded-atom potentials for cubic materials and impurities", Phys. Rev. B **46**, 2727 (1992).
3. [Bour01] L. Bourgeois, B. C. Muddle and J. F. Nie, "The crystal structure of the equilibrium phase in Mg-Zn-Al casting alloys", Acta mater. **49** 2701-2711 (2001).
4. [Buch98] F. von Buch and B.L. Mordike, "Microstructure, mechanical properties and creep resistance of binary and more complex magnesium scandium alloys," Mg Alloys & their App. Conf. 1998, 145, Wolfsburg, Germany (1998).
5. [Daw84] M. S. Daw and M. I. Baskes, "Embedded-atom method: Derivation and application to impurities, surfaces, and other defects in metals", Phys. Rev. B **29**, 6443 (1984).
6. [E03] W. E and B. Engquist, "Multiscale Modeling and Computation", Notices of the AMS **50**, 1062 (2003).
7. [Espi01] H. D. Espinosa, H. -C. Lu, P. D. Zavattieri, and S. Dwivedi, "A 3-D Finite Deformation Anisotropic Visco-Plasticity Model for Fiber Composites," J. of Composite Materials **35**, 369 (2001).
8. [Gail02] B. A. Gailly and H. D. Espinosa. "Modelling of Failure Mode Transition in Ballistic Penetration with a Continuum Model Describing Microcracking and Flow of Pulverized Media", Int. J. for Numerical Methods in Engineering, **54**, 365 (2002).
9. [Hao04] Su Hao, Brian Moran, Wing Kam Liu, and Gregory B. Olson, "Multi-scale constitutive model and computational framework for the design of ultra-high strength", Computer Methods in Applied Mechanics and Engineering **193**, 1865 (2004).
- 10.[Hors03] M. F. Horstemeyer and P. Wang. "Cradle-to-grave simulation-based design incorporating multiscale microstructure-property modeling: Reinvigorating design with science", Journal of Computer-Aided Materials Design **10**, 13 (2003).
- 11.[Jeli07] B. Jelinek, J. Houze, Sungho Kim, M. F. Horstemeyer, M. I. Baskes, and Seong-Gon Kim, "Modified embedded-atom method interatomic potentials for the Mg-Al alloy system", Phys. Rev. B **75**, 054106 (2007).
- 12.[Kim05] I. Y. Kim and O. L. de Weck, Structural and Multidisciplinary Optimization **31**, 105 (2005).
- 13.[Kim07] Seong-Gon Kim, Mark F. Horstemeyer, Randall German, Hongjoo Rhee, Sungho Kim, Shengjun Zhang, Greg Olson, Qingyou Han, "Task 4: Materials Design for Mg Alloys," ORNL FY 2006-2007 Annual Report, Chap. 4, 28—45 (2007).

- 14.[Kim09] Seong-Gon Kim, M. F. Horstemeyer, M. I. Baskes, Masoud Rais-Rohani, Sungho Kim, B. Jelinek, J. Houze, Amitava Moitra, and Laalitha Liyanage, “Semi-empirical Potential Methods for Atomistic Simulations of Metals and Their Construction Procedures,” *J. Eng. Mater. Technol.*, 131 (4), 041210 [9 pages] (2009).
- 15.[Kres96] G. Kresse and J. Furthmüller, “*Efficient iterative schemes for ab initio total-energy calculations using a plane-wave basis set*”, *Phys. Rev. B* 54, 11169 (1996).
- 16.[Kres99] G. Kresse and D. Joubert, “*From ultrasoft pseudopotentials to the projector augmented-wave method*,” *Phys. Rev. B* 59, 1758 (1999).
- 17.[Li03] Youhong Li, Donald J. Siegel, James B. Adams, and Xiang-Yang Liu, “*Embedded-atom-method tantalum potential developed by the force-matching method*”, *Phys. Rev. B* 67, 125101 (2003).
- 18.[Lian98] P. Lianga, T. Tarfab, J.A. Robinsonc, S. Wagnera, P. Ochinb, M.G. Harmelinb, H.J. Seiferta, H.L. Lukasa, F. Aldinger, “*Experimental investigation and thermodynamic calculation of the Al-Mg-Zn system*,” *Thermochimica Acta* 314 87-110 (1998).
- 19.[Olso00] G. Olson. “**New age of design**”, *Journal of Computer-Aided Materials Design* 7, 143 (2000).
- 20.[Perd81] J. P. Perdew and A. Zunger, “*Self-interaction correction to density-functional approximations for many-electron systems*”, *Phys. Rev. B* 23, 5048 (1981).
- 21.[Perd96] J. P. Perdew, K. Burke, and M. Ernzerhof, “*Generalized Gradient Approximation Made Simple*”, *Phys. Rev. Lett.* 77, 3865 (1996).
- 22.[Shia06] C. Shiao, “*Design of a Self-Healing Alloy for the Application of Unmanned Aerial Vehicles*”, Senior Project Report, Northwestern University (2006).
- 23.[Sing03] D. Singh, C. Suryanarayana, L. Mertus, and Chen R.-H., “*Extended homogeneity range of intermetallic phases in mechanically alloyed Mg-Al alloys*,” *Intermetallics* 11, 373 (2003).
- 24.[Sun07] Z. Sun, M. Zhou, H. Hu, N. Li, “*Strain-hardening and fracture behavior of die cast magnesium alloy AM50*”, *Res. Letter. Mater. Sci.* (2007).
- 25.[Wei95] L. Y. Wei, G. L. Dunlop and H. Westengen, *Metall. Mater. Trans. A-Phys. Metall. Mater. Sci.* 26, 1705 (1995).

I. High Throughput Isotopic Diffusion Databases for Magnesium Integrated Computational Materials Engineering

Principal Investigator: Nagraj S. Kulkarni
Research Assistant Professor
Department of Materials Science & Engineering
Center for Materials Processing
University of Tennessee; Knoxville, TN 37996-0816

Monolithic Systems Development Group
Oak Ridge National Laboratory
Measurement Science & Systems Engineering Division
Oak Ridge, TN 37831-6006
(865)576-0592; e-mail: kulkarnins@ornl.gov

Participants:
Peter Todd
Oak Ridge National Laboratory
Professors Yongho Sohn and Kevin Coffey
University of Central Florida

Technology Area Development Manager: Dr. Carol Schutte
(202) 287-5371; e-mail: carol.schutte@ee.doe.gov

Field Technical Monitor: C. David Warren
(865) 574-9693; e-mail: warrend@ornl.gov

Contractor: Oak Ridge National Laboratory (ORNL)
Contract No.: DE-AC05-00OR22725

Objective

- Develop a tracer diffusion database for magnesium-rich phases in the magnesium-aluminum-zinc-manganese (Mg-Al-Zn-Mn) system using secondary ion mass spectrometry (SIMS) for measurements of diffusion depth profiles of isotopes.

Approach

- Establish procedures for high purity (oxygen-free) thin film isotope deposition and SIMS isotopic ratio measurements of diffusion depth profiles in a few select Mg alloy samples.
- Determine impurity diffusion coefficients of Al, Mn and Zn in pure Mg by analysis of SIMS diffusion depth profiles in pure Mg samples annealed at various temperatures.
- Prepare homogeneous single-phase compositions in the Mg-rich hexagonal close packed (hcp) phase of ternary subsystems such as Mg-Al-Zn and Mg-Al-Mn and a few in the quaternary Mg-Al-Zn-Mn. Deposit thin films of stable isotopes (Mg, Zn) of the primary elements and anneal at different temperatures and times. Analyze diffusion data using SIMS to obtain Mg and Zn tracer diffusion coefficients for various compositions as a function of temperature.

- Repeat the above procedure using radioisotopes of Al¹ and Mn (since both these elements are monoisotopic) in order to measure the Al and Mn tracer diffusion coefficients.
- Construct a tracer diffusion database in the quaternary hcp single phase Mg-Al-Zn-Mn system by fitting tracer diffusion data as a function of composition and temperature using polynomial or other suitable functions.

Milestone, Metrics and Accomplishments

- *Calibration of depth profiling and isotope ratio measurement.* A primary requirement of the project is the capability to quickly and accurately measure isotopic ratios in Mg samples using SIMS. The SIMS instrument at University of Central Florida (UCF) (Cameca IMS 3f) has been calibrated for depth profiling (using profilometry) and isotope ratio measurements at various depths using Mg alloys.
- *Measured Al impurity diffusion coefficient in pure Mg.* Thin films of pure Al with thicknesses in range of a few hundred nm were successfully deposited using physical vapor deposition on several disc specimens of pure Mg. These coated specimens were annealed at various temperatures below 500°C for appropriate time (few hours) and quenched. SIMS depth profile measurements of Al in pure Mg were carried out, and the Al impurity diffusion coefficient in Mg was determined to be $1.74 (\pm 0.4) \times 10^{-17} \text{ m}^2/\text{sec}$ and $2.38 (\pm 1.0) \times 10^{-15} \text{ m}^2/\text{sec}$ at 300°C and 400°C respectively, which were slightly lower compared to the Mg self-diffusion coefficients at these temperatures.
- *Prepared sputtering target foils of stable isotopes of Mg and Zn and performed preliminary sputter deposition experiments.* Isotopic target foils (1 inch diameter, 500 mm thickness) of the stable isotopes of magnesium (²⁵Mg) and zinc (⁶⁸Zn) were prepared at the ORNL Isotopic Processing Facility. An ion beam sputter deposition system was utilized to deposit thin films (100-200 nm) of these isotopes on pure Mg and Mg alloy samples.
- *Investigated causes of oxygen contamination during ion beam sputter deposition and recommended the design and construction of a specially-tailored ultra-high vacuum (UHV) deposition system to mitigate the problem.* X-ray Photoelectron Spectroscopy (XPS) and SIMS analyses of deposited Mg and Zn thin film isotope films revealed that oxygen was the major impurity in the thin films (200 nm) deposited using an ion beam sputter deposition tool at ORNL, or a commercial Automated Sample Preparation System (ASAP) manufactured by Fischione Incorporated. A special UHV deposition system that has the desired high levels of vacuum (10^{-9} Torr) and rapid deposition capability to prevent oxygen contamination during thin film deposition was recommended, and an initial design was proposed.

Future Direction

- Control instrumentation parameters and procedures to obtain constant sputtering rates (within 5-10% of the mean) with the SIMS system, so that the relationship between the sputtering depth and time is clearly quantified.
- Complete Mn and Zn impurity diffusion measurements in pure Mg.
- Complete the construction and testing of the proposed UHV deposition system at the University of Central Florida (UCF) for high purity thin film deposition of Mg and Zn isotopes.

¹ Work involving the radioactive isotopes is subject to plus-up funds requested in FY 2010 and FY 2011, and the availability of the radioactive isotope of Al (²⁶Al).

- Conduct Mg and Zn tracer diffusion studies in the Mg-rich single phase of the Mg-Al-Zn system. This will require diffusion annealing of thin film isotopic samples deposited using the UHV system followed by SIMS-based isotopic ratio depth profile measurements of Mg and Zn isotopes in various sample compositions.

Introduction

The objective of this project is to create an isotopic (tracer) diffusion database in the Mg-rich phase of the Mg-Al-Zn-Mn system. This database along with the thermodynamic database that is being continuously updated will be provided to participants involved in various tasks in the Mg-ICME [1] program. That program includes Phase Field simulation in Super Vacuum Die Casting (SVDC); sheet forming simulation; and application to models of properties, such as high-cycle fatigue and creep. The project report for FY 2008 provided the background and the rationale for developing a tracer diffusion database as opposed to a mobility database [2, 3] for the Mg-ICME program. A discussion of the phenomenological diffusion formalism that can utilize the tracer diffusion and thermodynamic database as input with the aid of the Manning [4] or Moleko et al. [5] theoretical formalisms was provided. Additionally, a case was made for the separation of diffusion databases from thermodynamic databases, which is not possible with the mobility approach. Finally, some advantages of using stable isotopes with SIMS measurement techniques for generating tracer diffusion databases was provided even though it was recognized that two of the four elements in the current system, i.e., Al and Mn, are monoisotopic (i.e., elements with only a single stable isotope), and hence require the use of radioisotopes.

The procedure for obtaining tracer diffusion data first requires the preparation of homogeneous single-phase samples in the desired Mg-Al-Zn-Mn system using conventional techniques. This is followed by deposition of the stable or radioisotopes of these elements in the form of thin films on the samples and the measurement of isotopic diffusion profiles in these samples after diffusion annealing using SIMS. Analysis of the diffusion depth profile data using the thin film solution [6] provides the tracer diffusivity for the selected sample composition at the annealing temperature. By repeating such measurements for different compositions and temperatures, a significant amount of tracer diffusion data for Mg, Al, Zn and Mn in the single phase Mg-Al-Mn-Zn system can be obtained. These data can then be fitted using suitable polynomial functions to generate the tracer diffusion database. That database is essentially a collection of model functions and parameters that are needed to obtain the tracer diffusivities of the four elements in this system as a function of composition and temperature. Using the Manning [4] or the more recent Moleko [5] relations, the tracer diffusion database can be used to obtain the complete matrix of phenomenological coefficients or alternatively the mobilities, either of which may be used in modeling efforts. For some applications, such as property models, the required interdiffusion information can be obtained by combining the tracer diffusion database with a thermodynamic database by employing the Manning or Moleko relations.

The objective in the first year of this study was to establish the isotopic ratio method for SIMS diffusion measurements, prepare stable isotopic foils and then conduct diffusion measurements in the Mg-Al-Zn system. That system is the base system for commercial AZ (i.e., Mg-Al-Zn) alloys. While the first two objectives were met, the third objective, i.e., tracer diffusion studies in Mg-Al-Zn alloys, could not be met due to the high levels of oxygen impurity in the isotopic films deposited using commercial ion beam sputtering systems. The causes of this problem were analyzed and a decision was made to design and construct an in-house UHV deposition system that would be capable of providing high-purity films of enriched isotopes (Mg, Zn) on Mg-alloy samples. As a subset to tracer diffusion measurements in concentrated Mg-alloys, impurity diffusion measurements of elements such as Al, Zn and Mn in pure Mg were initiated after establishing the procedures for such measurements. Al impurity diffusion coefficients in pure Mg were obtained at various temperatures below 500°C for the very first time. This was

compared to the data for the Mg self-diffusion data along with the impurity diffusion data for other elements in pure Mg that was available in the literature [7, 8].

Progress in Fiscal Year 2009

Isotope Ratio Measurement and the Effect of Profiling Depth

For accurate SIMS diffusion profile measurements involving an enriched Mg isotope, the use of isotopic ratios, rather than the absolute abundance, as the concentration variable is preferred due to the minimization of instrument variability. For pure Mg, the isotopic ratios of the minor (^{25}Mg and ^{26}Mg) to the major isotope of Mg (^{24}Mg) were examined using a Cameca IMS 3f SIMS system as a function of profiling depth. For this measurement, an O_2 primary beam with 10kV (5.5kV on the sample) primary voltage, 20nA beam current, circular detection area of 60 mm in diameter, and high mass resolution was used. As seen in [Figure 1](#), the ratios remained relatively constant as a function of sputtering depth for Mg and its alloys, except for surface artifacts (<200 nm). The measured stabilized isotope ratios for pure Mg and several Mg-based alloys are reported in [Table I](#). An excellent agreement was found when compared to standard reference data (e.g., NIST).

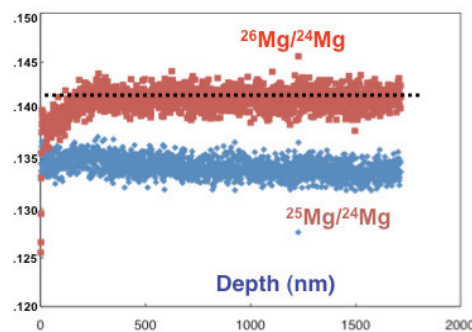


[Figure 1](#). SIMS depth profiling of Mg isotope ratios in Mg samples.

[Table 1](#). SIMS isotopic ratios in pure Mg and several Mg-based alloys

	$^{25}\text{Mg}/^{24}\text{Mg}$ Ratio (SD)	$^{26}\text{Mg}/^{24}\text{Mg}$ Ratio (SD)
Refer- ence value (NIST)	0.127	0.139
Mg	0.129 (<0.001)	0.138 (<0.001)
Mg-Al-Zn	0.130 (<0.001)	0.139 (<0.001)
AZ31B-2	0.129 (<0.001)	0.138 (<0.001)
AM60B-2	0.130 (<0.001)	0.139 (<0.001)

Impurity Diffusion of Al in pure Mg

Thin Film Deposition of Al-impurity on Pure Mg. Five pure Mg disc specimens were coated with a thin film of Al for diffusion experiments to extract impurity diffusion coefficients via SIMS depth profiling. Approximately 500 nm thick layer of Al was deposited on each Mg disc. The Mg substrates were radio frequency (RF) plasma cleaned *in-situ* prior to deposition, and an Al layer was deposited by DC magnetron sputtering from pure Al targets. The depositions were performed in 4 mTorr of Ar and the deposition chamber pressure around 10^{-8} Torr was obtained prior to performing the depositions. Using SIMS, the concentration vs. depth profiles were obtained for as-deposited and diffusion annealed specimens as shown in [Figure 2](#). For

impurity diffusion profile measurements, Mg isotope ratio measurements were not applicable since Mg enriched isotopes were not utilized.

Diffusion Anneal. Based on the self-diffusion coefficient of Mg ($D_0 = 1.4 \text{ cm}^2/\text{s}$ and $Q = 135 \text{ kJ/mol}$ in the usual Arrhenius expression) reported by Fujikawa [7], the diffusion depth profile measured by SIMS was used to determine the time and temperature of diffusion anneal. From this calculation, it was determined that Al-coated Mg discs should be annealed at 400°, 350°, and 300°C for 0.5, 0.5 and 2 hours, respectively. The times chosen for these temperatures allow the measurement of dilute Al concentrations at a diffusion depth of few to several micrometers. The annealing procedure involved encapsulating specimens in quartz capsules with evacuation down to 10^{-7} Torr, then back-filling with argon to prevent oxidation. The sealed quartz capsules were placed in furnaces with an independent thermocouple reading. After the diffusion anneal, the quartz capsules were broken in ice water for rapid quenching. To the authors' knowledge, there is no available data on Al impurity diffusion coefficient in pure Mg [7, 8].

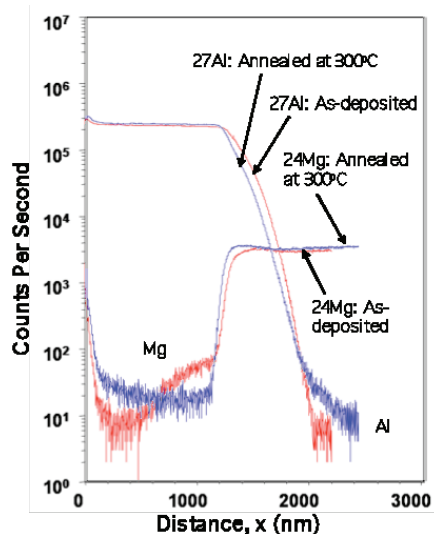


Figure 2. SIMS concentration profiles of Mg and Al from an as-deposited and annealed specimen.

Analysis of Diffusion Profiles. From a typical SIMS depth profile, the slope on a plot of the natural log of concentration as a function of the square of the penetration distance was obtained for the specimen annealed at 300°C for 2 hours as presented in Figure 3. Only the dilute Al concentration (10^2 counts/s) within the Mg-solid solution employed for the determination of impurity diffusion coefficient is presented, since the thin film solution [6] to extract the diffusion coefficient is only valid for a single phase. Based on six measurements using three different experimental runs, the impurity diffusion coefficient of Al in Mg at 300°C was determined as $D_{\text{Al}} = 1.74 (\pm 0.4) \times 10^{-17} \text{ m}^2/\text{sec}$.

The precision within an experimental run (e.g., one sample but three different regions) was determined to be $\pm 0.2 \times 10^{-17} \text{ m}^2/\text{sec}$. The impurity diffusion coefficient of Al in Mg is smaller than the self-diffusion coefficient of Mg at 300°C.

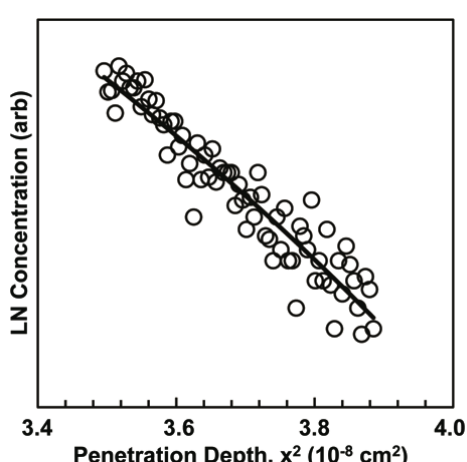


Figure 3. $\ln(\text{Al})$ concentration as a function of the square of its penetration depth in pure Mg after annealing for two hours at 300°C.

The Al impurity diffusion coefficient at 400°C was determined to be $2.38 (\pm 1.0) \times 10^{-15} \text{ m}^2/\text{sec}$. Again, the impurity diffusion coefficient of Al in Mg is smaller than the self-diffusion coefficient of Mg at 400°C. Figure 4 shows the Mg self-diffusion coefficient along with impurity diffusion coefficients of various elements as a function of temperature. The Al impurity diffusion has an activation energy that is similar to that of Mg self-diffusion.

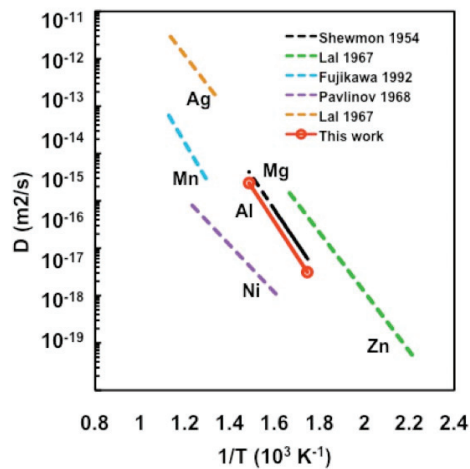
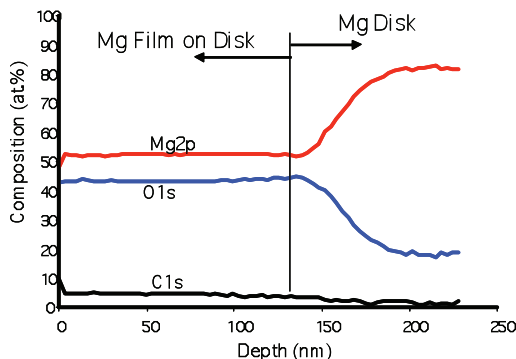


Figure 4. Impurity diffusion coefficient of Al in pure Mg (this work) compared to the Mg self-diffusion coefficient and other impurity diffusion coefficients [7, 8].

Ion Beam Sputter Deposition of Stable Isotopic Films

Stable isotopic target foils of Mg and Zn were prepared in the Isotope Processing Facility at ORNL. These were then used for ion beam sputtering thin films on pure Mg and Mg-Al-Zn samples from Alfa Aesar. XPS was used to determine the oxygen contents in the deposited Mg and Zn films (Figures 5 and 6). It is evident that there is significant oxygen in the films (about 40% for Mg and 30% for Zn). A list of factors responsible for the high oxygen levels include: (a) a very slow deposition rate (100 nm in approx. 80 min); (b) insufficient vacuum levels ($>10^{-8}$ Torr) prior to deposition; (c) lack of a load-lock to prevent air and moisture ingress during sample loading and unloading; (d) lack of a hot metal getter system to reduce oxygen levels in the Ar inert gas used as the sputter gas.

Figure 5. XPS sputter depth profile of Mg isotopic film on Mg sample (disk).



Attempts were made to address these issues, including the use of Xe as a replacement for Ar in order to increase the deposition rate. Additionally, a gas purifier was used to improve the purity of the inert gas. Some modest improvements both in the deposition rate (20% higher rate with Xe) and the purity of the Mg isotopic film were observed. In Figure 7, it is seen that the oxygen level reduced to about 10%.

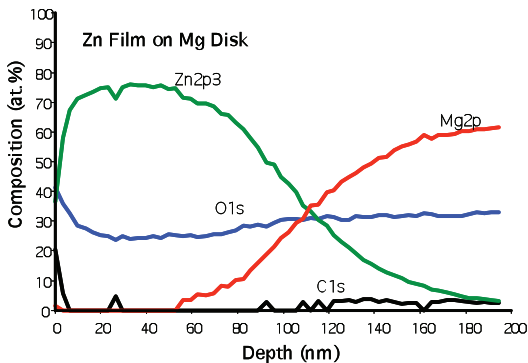


Figure 6. XPS sputter profile of Zn isotopic film on Mg sample (disk).

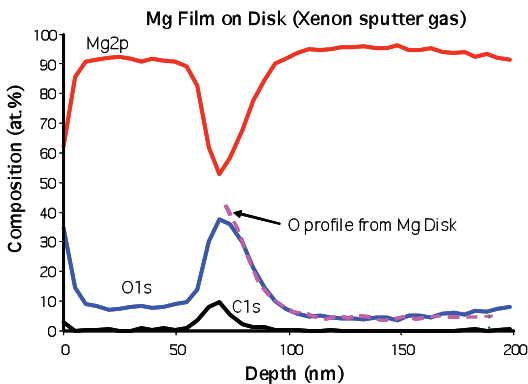


Figure 7. XPS sputter profile of Mg isotopic film on Mg sample (disk). Xe was used instead of Ar as the sputter gas, and a gas purifier was employed. The oxygen concentration in the film reduced to approximately 10 at. pct. compared to 40 at. pct. in Figure 5.

We also investigated deposition using a commercial Automated Sample Preparation System (ASAP) manufactured by Fischione Inc., since it did not appear that significant changes in the current ORNL ion beam sputter system were feasible (e.g., the vacuum level and load lock). Unfortunately, XPS and SIMS analysis of the films with the ASAP system also revealed a high level of oxygen. An XPS profile is shown in Figure 8.

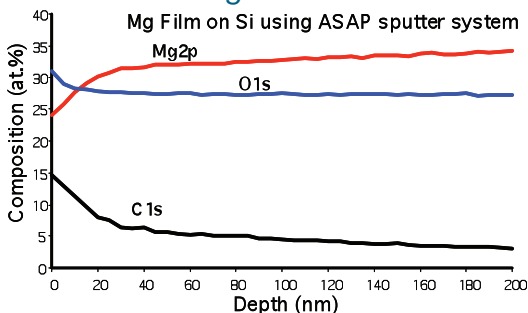


Figure 8. XPS sputter profile of Mg film on Si wafer with the ASAP system (Fischione).

Ultra-High Vacuum Deposition System for High-Purity Thin Films

It was found that current ion beam sputter deposition systems were unsuitable for high purity (oxygen-free) Mg isotopic film deposition. Hence, an ultra-high vacuum (UHV) sputter deposition system (Figure 9) is being designed and constructed to allow the deposition of oxide-free thin films (as diffusion sources) from the isotopic target foils of Mg and Zn. Several design features are included that will allow the deposition of these reactive films without oxidation:

1. The films will be deposited by high rate magnetron sputter deposition (compared to ion beam sputter deposition). The thin target foils (one inch in diameter) will be bonded to a water-cooled copper disk to allow a maximum sputtering power density to be used and deposition rates of ~ 10 nm per minute are expected.
2. The substrates will be mounted on water-cooled, magnesium, RF-powered holder that enables sputter etching of the substrate surface to remove the native oxide film prior to metal film deposition.
3. The background water vapor partial pressure will be below 10^{-9} Torr during film deposition. This UHV condition will be obtained by heating the vacuum chamber to ~150°C for 24 hours while continually pumping away the residual water from the chamber surfaces, and then cooling the chamber to room temperature to obtain a low water vapor out-gassing rate prior to metal film deposition.
4. Chamber UHV conditions will be initially established by use of a mass spectrometer to determine both the composition and the pressure of the residual gas. For the subsequent routine usage, the residual gas pressure only will be monitored prior to metal deposition by a bare ionization gauge.
5. Both turbo-molecular and titanium sublimation (getter) pumping will be used to obtain the UHV conditions. The sputter process gas (argon) is pumped only by the 240 liter/second turbo-molecular pump (is not gettered by titanium) and the pumping speed of the turbo-molecular pump will be modified by a conductance restriction (butterfly valve) to control chamber argon partial pressure. This conductance restriction is positioned as not to modify the pumping speed of the titanium sublimation pump (~600 liters/sec).
6. The argon introduced into the vacuum chamber as the sputter process gas (at 4 mTorr) will be from a 99.999% purity source gas and be further purified by a hot metal reactive getter installed in the system enclosure to parts-per-billion levels. Downstream of the purifier the argon gas will be plumbed to the system in all-metal-sealed pipes and valves to prevent re-contamination in transport.

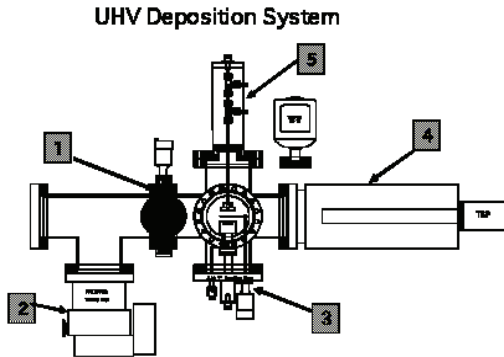


Figure 9. UHV deposition system: 1=Variable conductance for Ar pressure control; 2=Turbomolecular pump for Ar; 3=1" magnetron sputter deposition (or evaporation source) with shutter; 4=Ti sublimation pump for water vapor; 5=Substrate manipulator with RF power and water cooling (in situ cleaning of sample surface).

The above design features are expected to reduce the oxygen contamination of the Mg films by at least three orders of magnitude, when compared to the ion beam sputter deposited films. The initial qualification efforts for this system will be to confirm the oxygen-free deposition of high purity Mg films from low-cost Mg foil targets using Rutherford backscattering and XPS depth profiling. Once purity is demonstrated, high purity isotopic films will be deposited.

Conclusions

The SIMS instrument at UCF (Cameca IMS 3f) was used for depth profiling and isotope ratio measurements at various depths using Mg and Mg-base alloys.

- Isotopic thin film target foils of Mg and Zn were prepared for sputter deposition.
- The impurity diffusion coefficient for Al in pure Mg at various temperatures was determined.
- The processing conditions for the existing and commercial ion beam sputter systems used to deposit isotopic thin films of Mg and Zn resulted in significant oxygen levels in these films.
- The design and construction of a new UHV deposition system for high-purity deposition of isotopic films was initiated.

Presentations/Publications/Patents

P. Todd, N. Kulkarni, Y. Sohn, M. Klimov, L. Zevenbergen, and J. Henry “Isotopic Diffusion Studies in Mg-rich Light Metal Alloy Systems,” presented at the *2009 The Minerals, Metals & Materials Society (TMS) Annual Meeting*, San Francisco, CA, Feb. 15-19, 2009.

N. Kulkarni, “Challenges in Creating a Pure Element Tracer Diffusion Database,” presented at the *NIST Diffusion Workshop*, Gaithersburg, MD, March 25-26, 2009.

N. Kulkarni, P. Todd, Y. Sohn, S. Brennan and K. Coffey, “Isotopic Diffusion Database for Mg ICME,” presented at the *USAMP ICME for Magnesium Workshop*, USCAR, Southfield, MI, April 26-27 and Oct. 1, 2009.

S. Brennan, M. Klimov, Y. Sohn, K. Coffey, N. Kulkarni, and P. Todd, “Tracer Diffusion Studies in Magnesium,” presented at the Gordon Research Conference on Physical Metallurgy - Integrating Computational Materials Science and Engineering, Andover, New Hampshire, Aug. 2-7, 2009.

S. Brennan, A. P. Warren, K. R. Coffey, N. S. Kulkarni, P. J. Todd, Y. Sohn, and M. Klimov, “Experimental Determination of Al, Zn and Mn Impurity Diffusion Coefficients in Magnesium,” presented at the MS&T ‘09, Phase Stability, Diffusion Kinetics and Their Applications (PSDK-IV) Symposium, Pittsburgh, Pennsylvania, October 25-29, 2009.

N. S. Kulkarni, P.J. Todd, Y. Sohn, K. Coffey, and S. Brennan, “High Throughput Isotopic Diffusion Databases for Integrated Computational Materials Engineering,” presented at the 2009 AMD Lightweight Metals and Enabling Technologies Symposium, Detroit, Michigan, Oct. 13, 2009.

References

1. J. Allison, D. Backman, and L. Christodoulou, *J. Met.*, p. 25 (Nov. 2006).
2. J.-O. Andersson, T. Helander, L. Höglund, S. Pingfang, B. Sundman, *Calphad* **26**, p. 273 (2002).
3. C. E. Campbell, W. J. Boettinger, and U. R. Kattner, *Acta Mat.* **50**, p. 775 (2002).
4. J. R. Manning, *Met. Trans.* **1**, p. 499 (1970).
5. L. K. Moleko, A. R. Allnatt, and E. L. Allnatt, *Phil. Mag. A* **59**, p. 141 (1989).

6. P. Shewmon, *Trans. Metall. Soc. AIME*, 250, p. 1021 (1954).
7. S. Fujikawa, *J. Jap. Inst. Light Metals* 42, p. 822 (1992).
8. *Diffusion in Solid Metals and Alloys*, Landolt-Börnstein Numerical Data & Functional Relationships in Science and Technology, Group III: Crystal & Solid State Physics, Volume 26, Ed. H. Mehrer, Springer-Verlag, 1990.

J. Cyberinfrastructure in the Southern Regional Center for Lightweight Innovative Designs (SRCLID)

Principal Investigator: Tomasz Haupt
Research Associate Professor
Center for Advanced Vehicular Systems (CAVS)
Mississippi State University
PO Box 5405, Mississippi State, MS 39762
(662)325-4524; email: haupt@cavs.msstate.edu

Participants: R. Carino, F. M. Ciorba

Technology Area Development Manager: Dr. Carol Schutte
(202) 287-5371; e-mail: carol.schutte@ee.doe.gov

Project Manager: Magda Rivera
(304) 285-1359; e-mail: magda.rivera@netl.doe.gov

Contractor: Mississippi State University
Contract No.: DE-FC-26-06NT42755

Objective

- The objective is to design and develop a cyberinfrastructure to exploit the recent transformative research in material science and mechanics involving multiscale physics-based predictive modeling, multiscale experiments, and design.
- More specifically, the creation of the cyberinfrastructure will result in the development of the “community of practice” portal that allows development and integration of multiscale physics-based materials models for selected properties and processes, in the context of United States Automotive Materials Partnership (USAMP) three-nation Magnesium Front-End Research and Development pilot project (MFERD), in particular Task 1.9: Cyberinfrastructure for Integrated Computational Material Engineering (ICME).

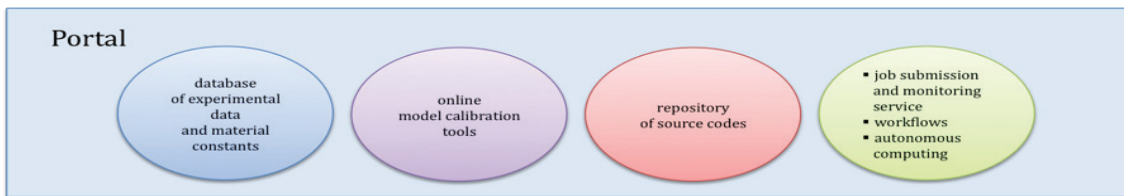


Figure 1. Cyberinfrastructure for SRCLID

Approach

- The development of the cyberinfrastructure for the computational materials engineering tools, technologies, and software approaches developed by other large-scale scientific cyberinfrastructure projects.
- The actual development and deployment of the cyberinfrastructure was driven by the requirements and early feedback generated by the engineering community, comprising Mississippi State University (MSST) researchers performing other tasks of this project, as well as researchers and engineers involved in the MFERD/ICME project.

- The experience developing the cyberinfrastructure for SRCLID (including MFERD/ICME) in Phases I and II indicates that the users' expected functionality is composed of four major components integrated through a single-access Web portal as shown in [Figure 1](#).
- The components are the following: database of experimental data and material constants, online model calibration tools, repository of codes, and a runtime environment for efficient and fault tolerant execution of multiscale simulations. Accordingly, the subtasks for the cyberinfrastructure development have evolved as follows. Subtask 1 addresses the need of MFED/ICME project for a web site devoted to disseminate project-related information to the project participants. Subtask 2 offers the development of the databases of experimental data and material constants. Subtasks 3 and 4 focus on the development of the model calibration tools. Subtask 5 is devoted to the optimization of high-performance codes for multiscale simulations, to be checked-in into the code repository area to be developed as Subtask 6. Subtask 7 aims to develop the autonomous runtime environment for executing complex workflows for multiscale simulations and design optimizations.

Accomplishments

- *Subtask 1:* The deployment, maintenance, and user support for MFERD and ICME SharePoint web servers; The MFERD portal assists in the management of the MFERD project and is restricted to MFERD project participants (currently 120 registered users from the U.S., Canada, and P.R. of China). The content of the site is moderated by Eric Nyberg (MFERD) and Robert McCune (ICME) with the help of the MSST team, and includes materials from annual MFERD meetings, semi-annual ICME workshops, and MFERD-wide announcements. The site has been accessed about 750 times by the authorized users.
- *Subtask 2:* The second release of the repository of experimental data and material constants. Currently the repository comprises stress-strain data and microstructural images, with preliminary support for fatigue strain-life data. A comprehensive testing and training has been conducted at CAVS/MSST. The repository is now being used to exchange magnesium-related data and models between researchers at MSST and the University of Virginia.
- *Subtask 3:* The development, validation, and documentation of stand-alone MATLAB-based model calibration tools. The validated tools are then released for the integration with the cyberinfrastructure (see Subtask 4), and the documentation is developed. All tools (integrated with the CI or not) require maintenance and upgrades according to the users feedback. In addition, the user support for the tools has been provided as a part of this task.
- *Subtask 4:* The integration of the tools developed in Task 3 with the cyberinfrastructure. The MSU ISV plasticity-damage tool is already integrated with the CI. The first target for the integration is the Microstructure Image Analyzer (an early prototype of it is already integrated, but an upgraded version with more functionality is now available). Other tools will be integrated as soon as made available as the result of performing Task 3.
- *Subtask 5:* The computational performance optimization of simulation codes for multiscale modeling. The goals of this task are to accelerate single-scale simulations and leverage the computational resources to execute simultaneously more simulations that are independent. A performance analysis environment (PAE) based on open-source performance profiling and tracing tools has been established and tailored to match the requirements of the simulation codes in use at CAVS/MSST.
- *Subtask 6:* Designed a repository of source codes of computational modules that will evolve into a platform for dissemination and collaborative development of all non-commercial, open-source simulation codes used by SCRLID and MFERD/ICME projects. The design is based on the open-source Subversion (a.k.a. SVN) revision control system and ViewVC web client for SVN that is used by a popular Source Forge open-source repository of codes.

- Subtask 7: Support for the autonomic computing will be initiated in Phase III.

Future Direction

During the first two years, the basic infrastructure has been created that forms a solid foundation for creating the cyberinfrastructure for engineering virtual organizations. Furthermore, preliminary implementation of vital components has been completed, in particular support for service-based repository of experimental data and material constants integrated with model calibration tools. In addition, we have started collecting and optimizing computational modules used in ICME processes, including multiscale simulations. During year three, the following activities have been planned:

The planned activities for year three include the following:

- Maintenance of all servers comprising the cyberinfrastructure, including MFERD/ICME portals.
- Repository of Experimental Data and Material Constants: Support the production mode, making it widely accessible to researchers within the MFERD/ICME project, in particular making it the project-wide platform for the exchange of magnesium data and material models. Populate the database with experimental data, generated at MSST and through collaborators and data taken from literature. Enhance access control mechanisms (group and/or project based) to support protection of intellectual properties, thus making it possible to open the database to the general public in the future, perhaps in collaboration with TMS. Collect the user feedback and enhance the repository by supporting more data types and more types of material models, as requested by the user community and the project objectives.
- Model Calibration Tools.
 1. First, the models are developed as stand-alone prototypes for testing and validation. The validated tools are then released for the integration with the cyberinfrastructure (see Subtask 4), and the documentation is developed. All tools (integrated with the CI or not) require maintenance and upgrades according to the users feedback. In addition, the user support for the tools will be provided as a part of this task. The following tools are planned:
 2. MSU ISV plasticity-damage (currently integrated with the CI but requiring the maintenance and user support) to be used in SRCLID program Tasks 1 and 5
 3. Microstructure Image Analyzer (currently developed but not yet fully integrated with the CI and requiring maintenance and user support) to be used in SRCLID Tasks 1 and 3
 4. Multistage Fatigue (developed but requiring validation and integration with the CI) to be used in SRCLID Task 3
 5. VEP Polymer (developed but requiring validation and integration with the CI) to be used in SRCLID Task 11
 6. VPSC Crystal Deformation (developed but requiring validation and integration with the CI) to be used in SRCLID Task 1.
 - The Integration of Tools within CI. The new tools will be integrated as soon as made available as the result of performing Subtask 3. The integration requires performing the following steps:
 1. Conversion of tools into a Web Service
 2. Development of Web browser-based Graphical User Interface (GUI)

- 3. Design of metadata format for the model results using the eXtensible Markup Language (XML)
- 4. Implementation of style sheets using the eXtensible Stylesheet Language (XSL) to display the XML result in the Web page
- 5. Providing a support in GUI for uploading the input data for the tool
- 6. Testing and validation
- 7. Maintenance and user support
- The Performance Optimization of Simulation Codes for Multiscale Modeling. The primary targets for these activities are:
 1. Grain Mapping module (meso scale) to be used in SRCLID Task 1
 2. Dislocation Dynamics module (micro scale) to be used in SRCLID Tasks 1,4
 3. Molecular Dynamics module (nano scale) to be used in SCRLID Tasks 1, 4, and 5
 4. Ab-initio Calculation module (quantum scale) to be used in SCRLID Task 6
- Repository of Computational Modules: The development of a repository of source codes of computational modules that will evolve into a platform for dissemination and collaborative development of all non-commercial, open-source simulation codes used by SCRLID and MFERD/ICME projects.
- Autonomic Computing: The design and prototype of a runtime environment for autonomic computing to execute workflows for multiscale simulations, which is a natural continuation of Subtask 5. The goals of this activity are the following:
 1. To simplify the submission and monitoring of high-performance codes for researchers and students at CAVS while providing fault-tolerance and achieving optimal utilization of computational resources.
 2. Demonstrate the system functionality and capabilities to the ICME community at large, and position us to request a community access and allocations to NSF and/or DOE supercomputing centers.

Introduction

The objective of this effort is to design and develop a cyberinfrastructure to exploit the recent transformative research in material science and mechanics involving multiscale physics-based predictive modeling, multiscale experiments, and design. More specifically, the creation of the cyberinfrastructure will result in the development of the “community of practice” portal that allows development and integration of multiscale physics-based materials models for selected properties and processes, in the context of United States Automotive Materials Partnership (USAMP) three-nation Magnesium Front-End Research and Development pilot project (MFERD), in particular Task 1.9: Cyberinfrastructure for Integrated Computational Material Engineering (ICME).

The development of the cyberinfrastructure for computational materials engineering will leverage tools, technologies, and software approaches developed by other large-scale scientific cyberinfrastructure projects supporting researchers and engineers, such as astronomy, medicine, biology, geophysics, earthquake engineering, and many more. Much of the foundation of the infrastructure is common across domains (security, grid integration, etc) and can serve to

bootstrap this project in delivering an initial working solution in a relatively short time frame. Some initial customization was needed to support the unique aspects of this project. After the initial system was developed, many of the advanced capabilities of the system required additional software development and customization and entirely new development to support additional features. Hence, we are proceeding with a two-stage development model: phase one was to leverage from existing software and tools to bring up a working software infrastructure, and phase two was to evaluate and further develop missing or insufficient software, as needed, to support the project requirements.

The actual development and deployment of the cyberinfrastructure is driven by the requirements and early feedback generated by the engineering community, comprising of Mississippi State University (MSST) researchers performing other tasks of this project, as well as researchers and engineers involved in the MFERD/ICME project. Frequent interactions between researchers and students developing the cyberinfrastructure with the community (as defined above) resulted in modifications of the initial plans, such as adding new elements to the cyberinfrastructure and changing the priorities of the development and deployment of the cyberinfrastructure components. The changes reflect a close collaboration between tasks and the pursuit to maximize the benefits of the cyberinfrastructure to end users.

Community of Practice Web Portal

The community of practice web portal that allows development and integration of multiscale physics-based materials models for selected properties and processes comprising four major components: database of experimental data and material constants, online model calibration tools, repository of codes, and a runtime environment for efficient and fault tolerant execution of multiscale simulations (c.f., Figure 1). In addition, the collaboration management tools are used to gather project-related documents, such as tasks descriptions, annual reports and presentations. In Phase II, we focused on the development of repositories to collect and disseminate through Web data, models, and codes pertaining to computational materials engineering. The remaining sections of this report provide the details of the design and implementation of these repositories. In Phase III we will also address the need for a runtime environment for running complex multistep design optimizations that involve multiscale materials and process simulations with uncertainty. As preparatory steps in this direction, we are developing an online repository of the computational codes that will be used in multiscale simulations and design optimizations, and in parallel, we are optimizing codes used in multiscale material modeling to be run efficiently on high-performance platforms.

The Repository of Material Properties

The repository of material properties (RMP) integrates three independent web applications: repository of experimental data, repository of material constants, and online model calibration tools.

Experimental data: The experimental data come from physical measurements of materials' properties. Currently, the repository supports stress-strain data, images of the microstructure, and strain-life (fatigue) data. The repository of experimental data is a database of the results of measurements (often requiring a transformation of raw data, such as deriving true stress-strain curves from force-displacement curves), or data taken from the literature. The user can upload the data to the repository, search for a particular data set, and retrieve the data for further analysis – typically to derive material constants.

Material constants: For the purpose of numerical simulations, a material is represented by mathematical models, such as the MSST DMG 1.0 plasticity-damage model, that provides the prediction of a material behavior subjected to certain conditions. The material model is

parameterized by a model-specific number of constants, referred to as material constants. The repository of material constants is a database of these constants. The constants are derived from the experimental data through model calibration. The user can upload the constants to the repository, search for the constants of a particular model of a particular material, and retrieve the constants for further analysis – typically to use them in numerical simulations, such as finite element analysis using ABAQUS, LS-Dyna, or other software codes.

Model calibration: Model calibration is the process of determining the material constants from the experimental data. The process usually involves solving an optimization problem to fit model parameters using experimental data and determine material constants for the material. The RMP provides online tools to perform the process.

Integration: Although each of the aforementioned web applications can be used independently, the advantage of RMP is that it integrates all three applications into one, thus allowing the complete cycle of analysis: upload experimental data, apply calibration tools to extract the material constants, save the constant to the database, and retrieve them in a form suitable to perform numerical simulations.

Architecture of RMP

RMP is implemented on top of two web services: Data Service and Compute Service

Data service: Data Service aggregates three independent sub-services: storage service, metadata service, and replica locator.

- Each experimental data set in the repository is stored in a file system. The **storage service** manages the part of the file system designated to store the data sets. When a file is submitted to the storage service, the service determines the location at which the file is to be stored, and returns its Universal Resource Identifier (URI) to the caller. GridFTP is used as the transport mechanism for moving the files to and from the storage.
- The metadata service collects the information about data sets maintained by the storage service. The information comprises the file identification (a name assigned by the user, project, material, etc.), the data provenance (owner, date submitted, etc.), tags enabling querying the metadata repository to find particular data sets matching search criteria, and some additional information necessary to process the data (such as transformation from raw force-displacement measurement to stress-strain relationship). When a new metadata record is created, the service returns its URI, so that, it can be referred to at a later time. The metadata repository is implemented as a DBMS application.
- The replica locator provides mappings between the metadata records and data files.

Because of this complexity, the Data Services are implemented as a façade. A facade is a service that provides a simplified interface to a larger body of codes, such as a class library, or a collection of independent services. The use of the facade pattern has several advantages:

- It makes the system easier to use and provides understanding of underlying services, since the facade has convenient methods for common tasks;
- It makes the code that uses the services more readable, for the same reason;
- It reduces the dependence of outside codes on the inner working element of the collection of services. Most codes use the facade, thus allowing more flexibility in developing the system;
- It wraps a complicated collection of Application Programming Interfaces (API) with a single well-designed API.

Other data items are stored only as a metadata. More details on the implementation of the data service have been provided in the last year's progress report and presented in several conferences [Haupt 2006a, Haupt 2006b Haupt 2007a, Haupt 2007b, Haupt 2008, and Haupt 2009].

Compute Service: The model calibration tools are implemented as MATLAB applications. In order to utilize them in the Web environment, a web service referred to as Compute Service has been developed. The service allows an interactive remote access to the pool of MATLAB instances running in the back-end. A pool of MATLAB instances is necessary to serve multiple users concurrently. Similarly to Data Service, the complexity of the Compute Service is hidden by a façade. Currently, three MATLAB applications (model calibration tools) are implemented:

MSST DMG Plasticity-Damage Model, Image Analyzer, and Multistage Fatigue Fit.

- **Damage Model:** The Mississippi State University internal state variable (ISV) plasticity-damage model (DMG) production version 1.0 [Horstemeyer 2009] is based on the ISV plasticity formulation of Bammann [Bammann 1990] with the additions of porosity [Bammann 1993] and from the work of Horstemeyer who added the void nucleation, growth, and coalescence rate equations that admit heterogeneous microstructures [Carino 2007]. The model is implemented as an ABAQUS user material subroutine (UMAT). The model calibration routine DMGfit was developed by Carino [Carino 2007], which updated the original BFIT routine by Lathrop [Lathrop 1993, Horstemeyer 2000]. The calibrated model constants can be directly merged into the “USER MATERIAL, CONSTANTS” section of an existing ABAQUS input deck. The stress-strain curves can also be exported as PamStamp2G material card format.
- **Image Analyzer:** ImageAnalyzer [Williams 2007] is a utility for calculating some material parameters from an optical image of a material. Groups of pixels in the image that satisfy user-specified criteria are interpreted to be objects of interest (i.e., particles, grains, voids). Associated with each object are the following quantities: area, centroid, first nearest neighbor distance, the length along a major axis, the length along a minor axis, and orientation. From these objects a number of material constants are derived such as particle size, particle volume (or area) fraction, coalescence factor, grain size or dendrite cell size, and initial void volume (or area) fraction.
- **Multistage Fatigue Fit:** This is a high fidelity MultiStage Fatigue (MSF) model to predict the amount of fatigue cycles required causing the appearance of a measurable crack. The crack size is a function of loading cycles. The model incorporates microstructural features to the fatigue life predictions for incubation, microstructurally small crack growth, and long crack growth stages in both high cycle and low cycle regimes.

Mashing-up Data Service and Compute Service: In web development, a mashing-up is a web page or application that combines data or functionality from two or more external sources to create a new service. The term mashing-up implies easy, fast integration, frequently using open APIs and data sources to produce results that were not the original reason for producing the raw source data. The RMP is a mashing-up of two independent services: data service and compute service, allowing to launch the model calibration tools in the context of selected data sets in the repository, and to automatically store the material contexts back to the database.

Front End of RMP

The front-end of the repository of experimental data and the repository of material constants is implemented as a single web page. In addition, the front end of each tool is a separate single page. Each of those pages serves as a Graphical User Interface (GUI). **Figures 2 and 3** show examples of the repository GUI.

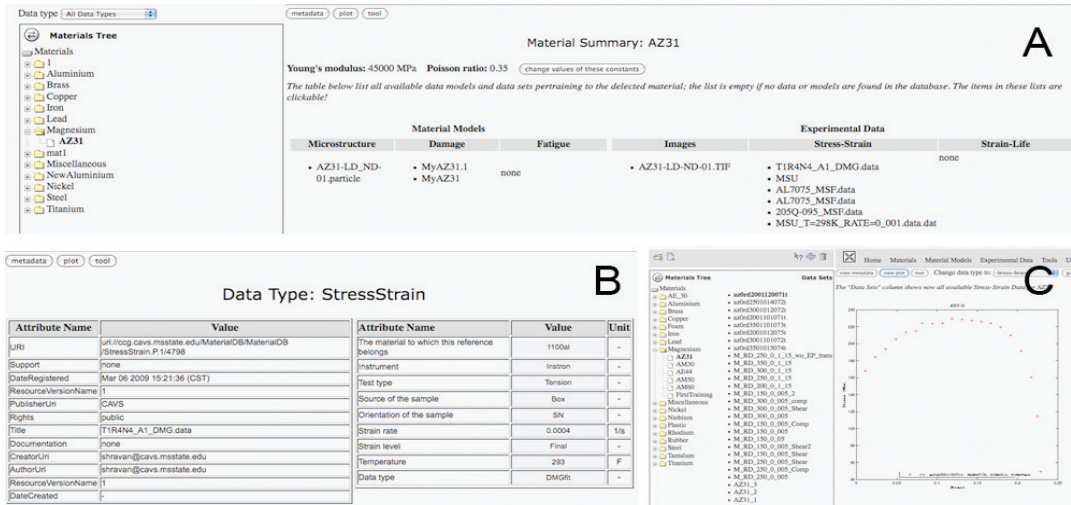


Figure 2. Example screenshots of the GUI of the repository: (A) material summary - for a selected alloy of Magnesium (AZ31).The repository has several sets of stress-strain data and microstructure image, as well as two damage models and a result of microstructure analyses; (B) the metadata for Aluminum 1100Al stress-strain data; (C) the stress-strain curve example displayed in the GUI.

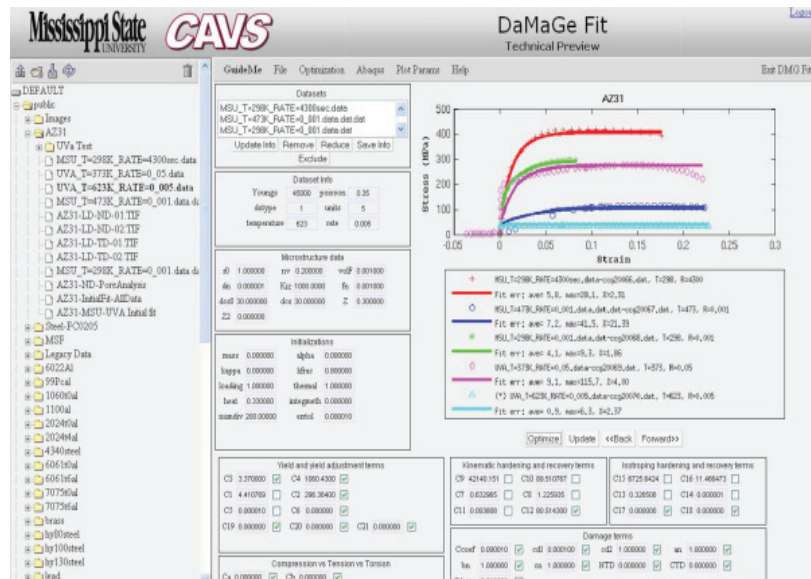


Figure 3. An example screenshot of the GUI of the repository: Damage fit interface.

The GUIs allow the user to interactively perform all actions supported by RMP by utilizing web widgets on the pages. GUIs are implemented using Asynchronous JavaScript and XML [AJAX]. The processing of the actions associated with GUI widgets is performed either locally using JavaScript, or delegated to the server side through AJAX calls. Regardless whether the processing is local or remote, only a relevant fragment of the web page hosting GUI is updated. Indeed, there is never a need to reload the whole page, unless a model calibration tool is invoked. By employing AJAX, the GUI has a look and feel of a stand-alone application with a very rich interface.

Repository of the Computational Modules

This activity has just been started. The research and development work is focused on three directions: infrastructure for the repository, web interface for the repository, and validation and optimization of computational performance of selected codes.

- *Infrastructure*: the repository is built using a popular, robust, open source revision control system “Subversion” (a.k.a. SVN) [Tigris.org]. The policies and the structure of the repository have been designed to address specific issues such as access control, non-repudiation, and maintenance of the production version of codes while it also enables concurrent development of research versions.
- *Web Interface*: The contents of repository will be available online for browsing and downloading codes, documentations, and installation instructions. For security reasons, submitting new codes and updates will be restricted to a small group of authorized users. Several existing implementations of the SVN web client have been evaluated. The ViewVC package (used by a popular SourceForge.com open source repository) [ViewVC] has been selected and installed at MSST, and it will be soon made available for general public.
- *Validation and Optimization of Codes*: Simulation codes used for multiscale modeling are generally written by researchers who have limited knowledge about computational performance issues. Some of the codes have been written 10 to 20 years ago and do not necessarily perform at its optimum levels on the latest bigger and faster computers. This effort aims at optimizing the computational performance of existing simulation codes by employing multi-core computers as well as on high performance parallel computer clusters. To achieve this goal, a Performance Analysis Environment (PAE) has been established and tailored to match the requirements of simulation codes in use at CAVS/MSST. PAE is based on open-source performance profiling and tracing tools. A first success of this effort is the optimization of a Microstructure Mapping Code, with an improvement factor of 100x [Carino 2009].

Presentations and Publications

- T. Haupt, “Cyberinfrastructure for the Integrated Computational Material Engineering”, 2009 *TMS Annual Meeting*, San Francisco, CA, February 15-19, 2009.
- M. Horstemeyer, R. Carino, Y. Hammi, and K.N. Solanki (Jun 2009) “MSU Internal State Variable Plasticity-Damage Model 1.0 Calibration, DMGfit Production Version Users Manual”. CAVS report MSU.CAVS.CMD.2009-R0010, *Mississippi State University: Center for Advanced Vehicular Systems*.
- R. Cariño, M. Horstemeyer, and C. Burton (Dec 2007) “Re-engineering DMGFit – Fitting Material Constants to Internal State Variable Models”. CAVS report MSU.CAVS.CMD.2007-R0040, *Mississippi State University: Center for Advanced Vehicular Systems*.
- T.N. Williams and R. Carino (Nov 2007) “ImageAnalyzer - A Software Tool for Calculating Certain Material Model Constants from Optical Images”, CAVS report MSU.CAVS.CMD.2007-R0039, *Mississippi State University: Center for Advanced Vehicular Systems*.
- R. Carino, F. M. Ciorba, Q. Ma, E. Marin “Improving the Performance and Usability of a Microstructure Mapping Code”, CAVS report MSU.CAVS.CMD.2009-R0023, *Mississippi State University: Center for Advanced Vehicular Systems*.

References

- AJAX: Asynchronous JavaScript and XML, an article in Wikipedia: http://en.wikipedia.org/wiki/Ajax_%28programming%29
- D.J. Bammann. 1990. “Modeling Temperature and Strain Rate Dependent Large of Metals.” *Appl Mech Rev* 43(5): Part 2.

- D.J. Bammann, M.L. Chiesa, M.F. Horstemeyer, and L.I. Weingarten. 1993. “Failure in Ductile Materials Using Finite Element Methods.” Structural Crashworthiness and Failure; Wierzbicki T, Jones N, eds. Elsevier Applied Science, the Universities Press (Belfast) Ltd.
- R. Cariño, F.M. Cioba, Q. Ma, and E. Marin. Improving the Performance and Usability of a Microstructure Mapping Code. MSU.CAVS.CMD.2009-R0023, Mississippi State University: Center for Advanced Vehicular Systems
- R. Cariño, M. Horstemeyer, C. Burton. 2007. Re-engineering DMGFit – Fitting Material Constants to Internal State Variable Models. MSU.CAVS.CMD.2007-R0040, Mississippi State University: Center for Advanced Vehicular Systems.
- Eclipse Ganymede <http://www.eclipse.org/ganymede/>
- T. Haupt. “Cyberinfrastructure for the Integrated Computational Material Engineering.” 2009 TMS Annual Meeting; San Francisco, CA; 2009 February 15-19.
- T. Haupt. (2007a) “Cyberinfrastructure for Multiscale Simulations.” 2007 TMS Annual Meeting; Orlando, FL; 2007 Feb 25-March 1.
- T. Haupt, M. Horstemeyer. “Cyberinfrastructure for Design Optimizations.” 2008 TMS Annual Meeting; New Orleans, LA; 2008 March 9-13.
- T. Haupt, A. Voruganti, A. Kalyanasundaram, and I. Zhuk, (2006a) “Grid-based System for Product Design Optimization.” 2nd IEEE International Conference on e-Science and Grid Computing; Amsterdam, the Netherlands; 2006 Dec 4-6.
- T. Haupt, A. Kalyanasundaram, G. Singh, and I. Zhuk. (2007b) “Data Repository for Ad-hoc Collaborations Horizontally Integrated with Transformation Services.” The 2007 International Conference on Grid Computing and Applications; Las Vegas, NV; 2007 June 25-28.
- T. Haupt, A. Kalyanasundaram, and I. Zhuk. (2006b) “Architecture for a Secure Distributed Repository.” 7th IEEE/ACM International Conference on Grid Computing; Barcelona, Spain; 2006 Sept-27-28: IEEE/ACM Press, 170-177.
- M. Horstemeyer, R. Cariño, Y. Hammi, and K.N. Solanki. 2009. MSU Internal State Variable Plasticity-Damage Model 1.0 Calibration, DMGfit Production Version Users Manual. CAVS REPORT MSU.CAVS.CMD.2009-R0010, Mississippi State University: Center for Advanced Vehicular Systems.
- M. Horstemeyer, J. Lathrop, A.M. Gokhale, and M. Dighe. 2000. “Modeling Stress State Dependent Damage Evolution in a Cast Al-Si-Mg Aluminum Alloy.” Theoretical Appl Fract Mech 33:31-47.
- J. Lathrop. (Dec 1996). BFIT—A Program to Analyze and Fit the BCJ Model Parameters to Experimental Data Tutorial and User’s Guide. SANDIA REPORT SAND97-8218. UC-405, Unlimited Release, Printed December 1996.
- Tigris.org, Subversion, home page : <http://subversion.tigris.org/>
- T. Williams and R. Cariño. 2007. ImageAnalyzer - A Software Tool for Calculating Certain Material Model Constants from Optical Images. MSU.CAVS.CMD.2007-R0039, Mississippi State University: Center for Advanced Vehicular Systems.
- ViewVC home page: <http://www.viewvc.org/>

K. Simulation-Based Design Optimization

Principal Investigator: Masoud Rais-Rohani
Professor, Aerospace Engineering
Mississippi State University (MSST)
318C Walker Engineering Bldg.
Mississippi State, MS 39762
(662) 325-7294; e-mail: masoud@ae.msstate.edu

Technology Area Development Manager: Dr. Carol Schutte
(202) 287-5371; e-mail: carol.schutte@ee.doe.gov

Project Manager: Magda Rivera
(304) 285-1359; e-mail: magda.rivera@netl.doe.gov

Contractor: Mississippi State University
Contract No.: DE-FC-26-06NT42755

Objective

- The objective of this task is to develop modeling, simulation, and optimization approaches to enhance the engineering design of automotive structures made of lightweight materials.

Approach

- Perform a theoretical study of plastic collapse and energy absorption in metallic multi-corner tubes. Using finite element simulations, investigate the influences of cross-sectional geometry and material system on energy absorption of metallic and composite crush tubes.
- Perform integrated material-product and process-product simulation and design optimization studies using the available ISV-based material models considering multiple design criteria such as damage and fatigue strength.
- Conduct a structural design optimization study for lightweighting and crashworthiness using full-vehicle crash simulations with ISV-based material models.
- Investigate the influence of micromechanical variables (i.e., reinforcement features and mechanical properties of constituent materials) on macromechanical response characteristics of automotive components made of fiber reinforced polymer composite materials.

Accomplishments

- Developed an analytical model for prediction of mean crush force in multi-cell, multi-corner metallic tubes with non-rectangular cell geometry.
- Applied a multilevel decomposition and optimization approach to product-material design optimization of a structural component using an ISV-based material model.
- Investigated the coupling of sheet forming and crush simulations using explicit/implicit nonlinear finite-element analysis.
- Developed a framework for coupled process simulation and optimization.

- Investigated two different modeling approaches to study the stiffness and strength properties of polymer matrix materials with nano-inclusions.
- Investigated the crush performance of composite crush tubes using coupled progressive failure analysis and nonlinear finite element simulation.
- Completed a number of conference and journal papers as listed at the end of this report.

Future Direction

- Conduct an optimization study using full-vehicle simulations with multi-scale material models under multiple design criteria, such as damage and fatigue.
- Investigate multilevel optimization of integrated material-product / process-product systems, using multiscale material models.
- Investigate the influence of nano-inclusions in polymer matrix on energy-absorption characteristics of crush tubes made of fiber-reinforced polymer composite materials.

Introduction

This annual report provides a summary of activities conducted under the simulation-based design optimization task of the DOE/SRCLID project. The areas of emphasis include the following: multilevel decomposition and optimization of product-material systems, sheet forming process simulation and optimization, stiffness modeling of inclusion enhanced polymer matrix materials, and crush simulation of fiber-reinforced polymer composite tubes. A summary of activities in each emphasis areas is presented.

Optimization of Product-Material Systems

Many complex engineering systems are more readily optimized when decomposed into separate system and subsystems with partitioned design variables and constraints.

Multilevel decomposition and optimization is particularly suitable for product-material systems. A simple example of such a system is shown in [Figure 1](#). At the first subsystem level, the product is decomposed into two elements, each focused on optimizing a particular structural member. For member 1, the hierarchy extends down to the material (e.g., aluminum) and a two-stage manufacturing process (e.g., *casting* followed by *rolling*, or *rolling* followed by *stamping*) with the opportunity to tailor the material microstructure and optimize a desirable property at each level, whereas for member 2, material (e.g., steel) is confined to a single element and characterized by a manufacturing process such as *extrusion*.

Modern approaches for the solution of hierarchical systems include analytical target cascading (ATC).^{1,2} Through level-by-level cascading in ATC, the upper-level design targets are propagated down to lower-level elements while outputs of individual elements are transferred upward as inputs to the connecting higher-level element (parent). A coordination strategy is used to ensure that the separately optimized subsystems satisfy the optimality conditions at the system level in the iterative solution process.

Application Problem

We applied the ATC method to product-material optimization of a multi-cell, multi-corner thin-walled tube. The FE model of the tube and its cross-sectional geometry are shown in Fig. 2. The

400-mm long prismatic tube consists of an outer square tube of size D_o and an inner square tube of size D_i that are connected together using four corner-to-corner web elements. All interior and exterior walls have the same thickness, t and material properties. The tube is free at the top end and fixed at the bottom.

We developed an analytical equation for the mean crush force under quasi-static loading using the super folding element theory³. By dividing the cross-section into a collection of multi-flange corner elements and considering the energy absorbed by each element, the mean crush force is estimated as⁴

$$P_m = \frac{1}{2\zeta H} \sum_{j=1}^{n_e} N_j E_{int}^j \quad (1)$$

where N_j represents the number of distinct corner elements with energy absorption contribution E_{int}^j , n_e represents the number of corner types present in the cross-section (there are two types in Figure 2), ζ is the effective crush distance coefficient that varies in the range of 0.68 to 0.75 for the multi-cell tubes considered, and H is the equivalent projected fold length. Since Eq. (1) is based on a single value for H , some error is introduced in the estimated value of P_m for the models with non-uniform fold geometries.

With a nonzero mean stress ($\sigma_m \neq 0$), the Smith-Watson-Topper formula is used to estimate the fatigue life of the tube as

$$\sqrt{(\sigma_m + \sigma_a)\sigma_a} = \sigma'_f (2N_f)^b \quad (2)$$

when σ_a is the stress amplitude, N_f is the number of cycles to failure, σ'_f is the fatigue strength coefficient, and b is the fatigue strength exponent. Although σ'_f is somewhat higher than σ_U , for relatively low ductility metals, σ'_f approaches σ_U .⁵ Here, for simplicity, we assume $\sigma'_f = \sigma_U$, which leads to the estimation of fatigue life as

$$N_f = \frac{1}{2} \left(\sqrt{(\sigma_m + \sigma_a)\sigma_a} / \sigma_U \right)^{1/b} \quad (3)$$

where the amplitude and the mean value of stress are calculated using

$$\sigma_a = \frac{F_a D_o}{2I} \quad (4)$$

$$\sigma_m = \frac{F_m D_o}{2I} \quad (5)$$

where I is the area moment of inertia, with F_a and F_m representing the amplitude and the mean value of the cyclical force, respectively, applied at the tip of the tube in the x direction. In equations (4) and (5), we let $F_a = 400$ N and $F_m = 0.25F_a$. Also, the exponent b in Eq. (3) is treated as a design variable.

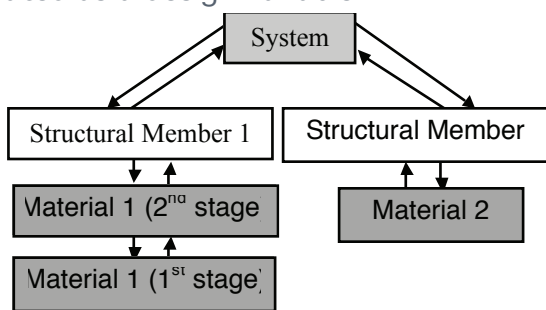


Fig. 1. A hierarchical product-material system.

Figure1. A hierarchical product-material system.

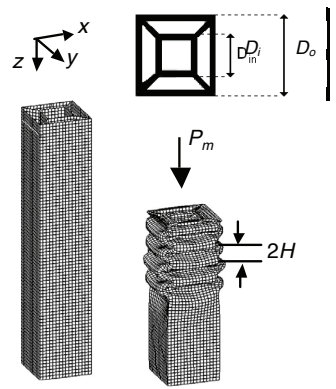


Figure 2. Multi-cell, multi-corner tube geometry and crush response.

The optimization problem seeks to minimize the weight of the crush tube subject to constraints on energy absorption (measured in terms of mean crush force and material toughness) and durability (measured in terms of fatigue life). For comparison purposes, the optimization problem is formulated and solved using both all-at-once and ATC approaches using an ISV-damage material model⁶.

For ATC solution, the tube is decomposed into two levels, structure on top and material at the bottom. At the top (system) level, the cross-sectional area (surrogate of weight) is minimized while maintaining consistency of the yield and ultimate strength targets with the values found below at the subsystem level.

The system-level optimization problem is stated as: Given σ_Y^L and σ_U^L , find the value of design variable vector $\mathbf{x}_{sys} = (t, D_i, D_o, b)$, target response variables $\mathbf{R}_{sub} = (\sigma_Y, \sigma_U)$, and tolerances ε_Y and ε_U to

$$\begin{aligned} & \min \quad A(\mathbf{x}_{sys}) + \varepsilon_Y + \varepsilon_U && (6) \\ \text{s.t. } & (\sigma_Y - \sigma_Y^L)^2 \leq \varepsilon_Y, \quad (\sigma_U - \sigma_U^L)^2 \leq \varepsilon_U, \quad P_m(\mathbf{x}_{sys}, \sigma_Y, \sigma_U) \geq 1.25 P_{m_{base}}, \quad N_f(\mathbf{x}_{sys}, \sigma_U) \geq N_{f_{base}}, \quad \mathbf{x}_{sys}^{\min} \leq \mathbf{x}_{sys} \leq \mathbf{x}_{sys}^{\max} \end{aligned}$$

The constraint on the mean crush force P_m requires a 25% improvement over the baseline value, $P_{m_{base}}$ whereas the fatigue life is required to be no shorter than that of the baseline model, $N_{f_{base}}$.

The material design variables selected for the ISV-damage model are the microstructural parameters such as the initial void radius, r_0 , average size of inclusion particles, d_n , particle volume fraction, f_n , grain size, DCS , and initial void volume fraction, $volF$. These variables represent some of the physical parameters that affect the damage mechanisms, and, hence, the stress-strain response and toughness of the material.

The subsystem-level optimization problem is stated as: Given target responses σ_Y^U and σ_U^U , find the value of design variable vector $\mathbf{x}_{sub} = (r_o, d_n, f_n, DCS, volF)$ and response variable vector $\mathbf{R}_{sub} = (\sigma_Y, \sigma_U)$ to

$$\begin{aligned} & \min \quad (\sigma_Y - \sigma_Y^U)^2 + (\sigma_U - \sigma_U^U)^2 && (7) \\ \text{s.t. } & T_o(\sigma_Y, \sigma_U) \geq 1.5 T_{o_{base}}, \quad \mathbf{x}_{sub}^{\min} \leq \mathbf{x}_{sub} \leq \mathbf{x}_{sub}^{\max} \end{aligned}$$

where material toughness measured as the area under the stress-strain curve with $\sigma_Y = \sigma_Y(\mathbf{x}_{sub})$ and $\sigma_U = \sigma_U(\mathbf{x}_{sub})$. The optimum design is required to have 50% higher toughness than the baseline model. The baseline values for the material design variables are taken from Horstemeyer (2001) for an aluminum alloy, and an in-house program is used to estimate the values of σ_Y and σ_U in terms of the selected material design variables. Both system- and subsystem-level optimization problems in equations (6) and (7) are solved using the sequential quadratic programming method (*fmincon* function in MATLAB).

The results are presented in [Table 1](#). The wall thickness is increased by approximately 20% while D_i and D_o are decreased by 50% and 43%, respectively, resulting in a reduction of 32% in cross-sectional area and weight. The stress-strain curve for the optimum design is compared to that of the baseline material in [Figure 3](#). The higher ultimate strength and toughness in the optimum material are visible in this figure.

Table 1. Comparison of the baseline and optimum designs

<i>Design Variables</i>	<i>Baseline Design</i>	<i>ATC Design</i>
t (mm)	2.0	2.40
D_i (mm)	30	15
D_o (mm)	50	28.6
b	-	-
	0.09	0.04
	4	7
r_0 (mm)	0.00 0.02	0.00 0.01
d_n (mm)	0.00 0.008	0.00 0.004
f_n	0.07	0.10
		5
DCS (μm)	20	10
volF	0.00	0.00
	1	5
<i>Responses</i>		
A (mm^2)	753.	512.
	1	1
P_m (kN)	95.3	119.
	3	2
N_f ($x 10^6$ cycles)	1.54	1.54
	8	8
T_o (MPa)	23.1	50.7
	1	3

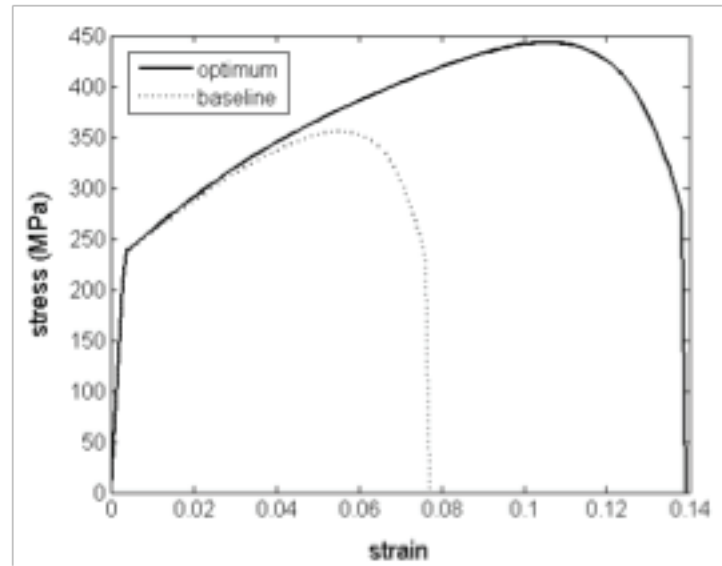


Fig. 3. Comparison of the stress-strain curves of the baseline and optimum designs.

To verify the accuracy of P_m found using Eq. (1), we also performed a nonlinear FEA to simulate the crush response of the multi-cell tube using the FEA code LS-DYNA. The stress-strain curve used in the FE simulations assumes a piecewise linear hardening material model with no rate sensitivity, failure, or damage. Using such a material model and ignoring any inertia effect, brings the results of dynamic FEA (in the range of 15 m/s impact velocity) fairly close to the quasi-static results. The FE-based P_m for the optimum design is about 5% higher than the quasi-static mean crush force predicted by the analytical model in Eq. (1). Additional details about

ATC and the application problem can be found in publication number 5 (Acar et al. 2009). We intend to apply the same approach to more complex product-material systems such as a front-end structure made of magnesium alloys.

Process-Product Analysis and Design

The initial focus of the research presented in this section of the report is twofold: 1) to perform numerical simulation of the sheet forming process of lightweight metal alloys such as aluminum and magnesium, and 2) to couple process simulation with product performance analysis and design optimization. Our goal is to investigate the merits of integrating ISV-based plasticity damage models with process-product simulation and optimization.

The forming process of interest is deep drawing / stamping (in single or multiple stages) and the primary performance attribute is the specific energy absorption under impact loading. In forming simulation, a blank sheet of material is held between the holder and the lower die while pressed by a punch or an upper die. The applied load causes plastic deformation (material flow) resulting in the sheet taking the shape defined by the geometry of the dies. During unloading, the part can deviate from the die geometry depending on the amount of spring back as dictated by residual stresses governed by the part geometry including the wall thickness and part temperature during the forming process.

Application Problem

A simple model, as shown in Figure 4, is used for the sheet forming process. Here, we used ABAQUS/Explicit for the loading phase of the cold forming process. The holders and the dies are modeled with analytical rigid surfaces whereas the blank is modeled with shell (S4R) elements. The holder force, friction coefficients between the contacting surfaces, punch load, and its load rate can all be used as process simulation parameters.

As a result of this forming process, the state variables such as stress, elastic/plastic strain, and the hardening parameters are no longer zero in the material. This information is retained in defining the correct initial conditions when the subsequent unloading simulation is performed using ABAQUS/Standard (implicit). In this part of the simulation, the holders and the upper die are separated from the formed part allowing for the simulation of spring back action as well as the measurement of the residual stresses. The final part geometry is influenced by the amount of spring back. Using the true part geometry as defined by process simulation along with the retained values of state variables, a crash (performance) simulation is performed with ABAQUS/Explicit.

For crash simulation, symmetric boundary conditions are imposed along the unloaded edges of the sheet to simulate a single cell rail (Figure 4). The model is held fixed at its base and is impacted by a mass of 300 kg traveling at a speed of 10.0 m/s. The crash simulation is done in ABAQUS/Explicit and the state variables are initiated from the result of forming simulation. To study the effect of process parameters on crash performance of the tube, the following cases are considered:

1. Using the die-matching geometry and ignoring the initial values of the state variables.
2. Considering the changes in geometry (spring back) and ignoring the initial values of the state variables.
3. Considering the spring back and residual stresses.

4. Considering the spring back, residual stresses and kinematic hardening.
5. Considering the spring back, residual stresses, isotropic hardening and damage.

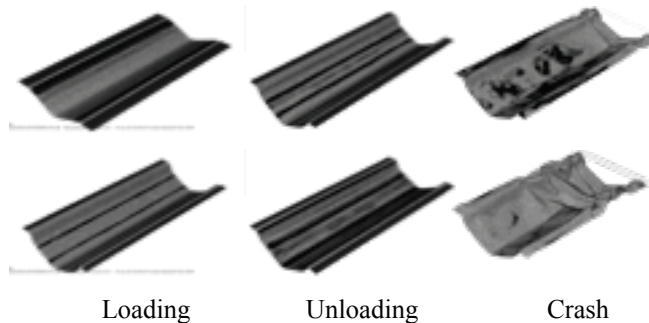


Fig. 4. Product-process simulation for case 4.

In cases 1-3, the material follows multi-linear isotropic and linear kinematic hardening laws whereas in case 4 it uses a linear kinematic and in case 5, a linear isotropic hardening model with damage.

Figure 4 shows the deformed shapes during loading, unloading (spring back) and crush using the properties of a steel alloy. In this case, the final stress distribution in each step is used as the initial state for the subsequent simulation. The plots of crush force versus time for cases 1, 2, and 4 are compared in Figure 5. The spring back can affect the energy absorption and collapse mode of the rail. In the material model used here, the residual stresses and the kinematic hardening state variable do not have a considerable influence on the energy absorption behavior.

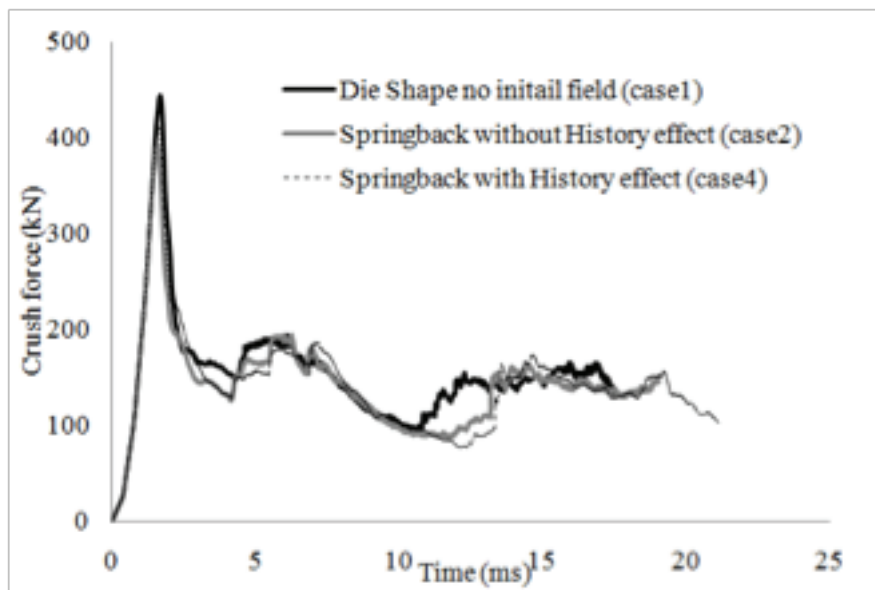


Fig. 5. Comparison of crush force history for cases 1, 2, and 4.

One of our objectives in this research is to study coupled process-product simulation and optimization. We have successfully developed and tested a framework for process based design optimization with Simufact.forming as the process simulation tool. However, we are continuing to work on details related to the proper transfer of information between the analysis code and the optimizer for problems involving complex geometries and a multi-stage forming process.

Modeling of Inclusion Enhanced Polymers

The addition of nano-inclusions such as nanofibers at certain volume fractions to a polymer material is shown to enhance the overall mechanical properties of the resulting nano-enhanced matrix. In hybrid multi-scale composite materials, where conventional reinforcing fibers are combined with nano-enhanced matrix, the nano-inclusions also improve the interfacial shear strength properties between the fibers and the enhanced matrix.^{7,8}

One of the challenging issues affecting the use of nano-enhanced polymers in industrial design applications is the limited understanding of their mechanical properties. In recent years, many modeling approaches ranging from molecular dynamic simulations at nano scale to FEA with homogenized properties at macro scale have been developed. Hybrid methods that use both FEA and micromechanical models seem to offer improvements in terms of both accuracy and computational performance.^{9,10}

Prediction of Stiffness Properties

We investigated the influence of carbon nanofiber inclusions on mechanical properties of a thermoset polymer matrix material (i.e., vinyl ester).

For the case of aligned nanofibers (modeled as parallel cylindrical inclusions), the simplified form of Mori-Tanaka method is used to calculate the resulting in-plane stiffness properties of the modified matrix. Here, the modified matrix is treated as a transversely isotropic material and labeled as material A.¹¹ For a small nanofiber volume fraction, f , the effective or homogenized elastic constants of material A can be calculated analytically as

$$\frac{E_{11}}{E_0} = \frac{1}{1 + f(A_1 + 2\nu_0 A_2)/A}, \quad \frac{E_{22}}{E_0} = \frac{1}{1 + f[-2\nu_0 A_3 + (1 - \nu_0)A_4 + (1 + \nu_0)A_5 A]/2A} \quad (8)$$

$$\frac{G_{12}}{G_0} = 1 + \frac{f}{\frac{G_0}{G_1 - G_0} + 2(1-f)S_{1212}}, \quad \frac{G_{23}}{G_0} = 1 + \frac{f}{\frac{G_0}{G_1 - G_0} + 2(1-f)S_{2323}}$$

where E_0 and G_0 represent the elastic and shear moduli of the matrix, G_1 and f are the shear modulus and volume fraction of the nanofibers, S_{ijkl} 's are the Eshelby's transformation tensor components calculated based on the aspect ratio of the nanofibers and the Poisson's ratio of the matrix, and A 's are constants calculated from the elastic properties of the nanofibers and the neat matrix.

Figure 6 illustrates the variations of the elastic properties of material A as a function of f for different nanofiber aspect ratios. The material properties used for these plots are: $E_0 = 3.5$ GPa, $\nu_0 = 0.35$, $E_1 = 450$ GPa, $\nu_1 = 0.19$, where the subscripts 0 and 1 refer to the matrix and nanofiber, respectively.

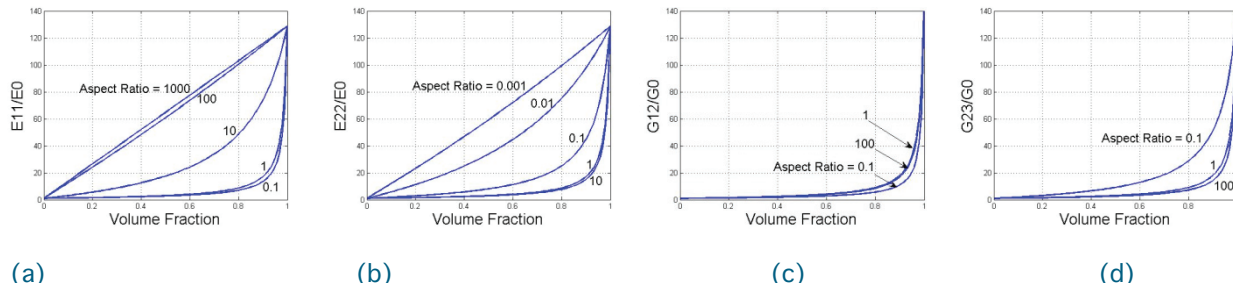


Fig. 6. Variations of normalized (a) longitudinal, (b) transverse, (c) in-plane shear, and (d) out-of-plane shear moduli as a function of nanofiber volume fraction.

Since the nanofibers are aligned and have superior properties in comparison to the neat matrix, the modified matrix properties tend to improve with an increase in f . However, it is interesting to note that the rate of increase depends on the aspect ratio of the nanofibers. In the case of E_{11} , the rate is highly nonlinear for small aspect ratios and becomes linear as aspect ratio increases. The trend is opposite for E_{22} . The rates of increase in G_{12} and G_{23} are nonlinear functions of f as noted in Eq. (8), with aspect ratio having a more pronounced impact on G_{23} than G_{12} .¹² It should be noted that the Mori-Tanaka homogenization scheme has been shown to yield reasonable results in low volume fraction (dilute) composites. Hence, we focused on low volume fraction cases.

For the case of randomly oriented nanofibers, we used two analytical modeling approaches: (1) treating the modified matrix as a composite laminate made of transversely isotropic layers, and (2) using the general Mori-Tanaka method. In the first approach, the matrix (labeled as material B) is modeled as an equivalent quasi-isotropic [0/45/-45/90]_s laminate made of multiple layers of material A.⁸ It should be noted that the laminated composite layers in this stage are reinforced only by unidirectional discontinuous nanofibers. The out-of-plane stiffness properties are assumed to be the same as the in-plane properties in the quasi-isotropic laminate. Based on a building block approach, the material constituent analyzer (MCA) in the analysis code GENOA is used to calculate the stiffness properties.

In the second approach, the general Mori-Tanaka method is based on Eshelby's solution for an ellipsoidal inclusion in an infinite domain requiring the averaging of the 4th order stiffness tensor in all directions. We have completed the major portion of a MATLAB implementation of the general Mori-Tanaka method and are working on the orientation averaging part of the algorithm to have a stand-alone analysis tool to continue our investigation.

Prediction of Strength Properties

For prediction of the unidirectional strength properties of material A, the shear lag theory is used. For material B, a progressive failure analysis with the computer software, GENOA is performed to characterize the general strength properties of the modified matrix.

The goal we are pursuing in this area is to use the calculated stiffness and strength properties of the modified matrix in the quasi-static analysis of laminated fiber reinforced composite crush tubes enabling the optimization of such components with proper balance between cross sectional geometry and properties of nano-inclusions, fiber, and matrix materials.

Crush Simulation of Composite Tubes

The main energy absorption mechanism in polymer composite crush tubes is in the form of widespread micro-fracture. Progressive failure analysis (PFA) can be used to capture the effects

of micro-fractures through different failure criteria. Here, the PFA capabilities of GENOA are coupled with FEA capabilities of LS-DYNA to perform crush simulations of composite tubes.

First, the stiffness properties of the laminate are calculated using the classical lamination theory in GENOA/MCA as input to LS-DYNA. After completion of one nonlinear FE solution step, the updated stress and strain data are transferred back to GENOA/PFA, which can use over ten different failure criteria to search for failure in the FE model. When failure is detected, the stiffness properties of the damaged plies are reduced using the stiffness degradation factors that are derived from physical experiments. These factors depend on the failure mode and loading type. Once all the plies experience catastrophic failure, the element is removed from the model, and the updated laminate properties replace the old material card before FEA proceeds to the next iteration.

Ideally, the PFA results should be transferred back to the FE solver after each time step. However, to improve computational efficiency, the transfer is made after the completion of several time steps. To enhance solution accuracy, the number of damaged elements is checked, and if it is less than the specified limit, the time step is halved and the current step is restarted based on the updated damage state.

Application Problem

A quasi-static analysis is used to simulate the axial crushing of a carbon-epoxy cylindrical tube at 55% fiber volume fraction is considered. The tube is held fixed at its base and a linear incremental displacement is applied at its tip. The tube length, outer diameter, and wall thickness are $L = 90$ mm, $D = 50.8$ mm, and $t = 1.33$ mm, respectively. The contact friction coefficient between the rigid wall and the tube is set at 0.3. A frictionless self-contact condition is also defined for all the element surfaces to prevent element-element inter-penetration due to excessive deformation.

Using analytical micromechanical models, the ply properties are calculated. The laminate or element properties are derived from classical lamination theory to introduce the A, B and D matrix elements as the material card (*MAT_118) in LS-DYNA. The resultant or running stress in the element mid-surface is used for stress calculations in individual plies. In order to obtain a stable crush pattern, a trigger mechanism, in the form of a small axi-symmetric conical groove with length of 5.13 mm and diameter of 52.36 mm is placed near the free (impacted) end of the tube. [Figure 7](#) shows the deformation shape as obtained in GENOA/LS-DYNA simulation.

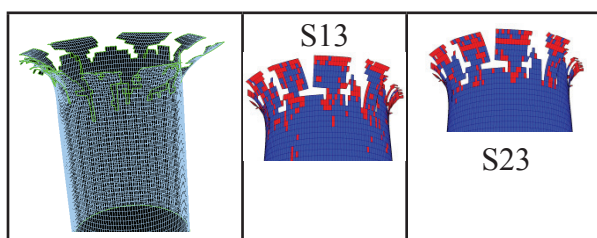


Fig. 7. Predicted crush mode and transverse shear damage distributions as measured by S13 and S23.

Since the FE model uses shell elements, the actual delamination cannot be captured. However, the general frond pattern is similar to several experimental results as reported in the literature. Figure 7 also shows the transverse shear damage distribution in the tube.

The energy absorption behavior of a crush tube is characterized based on the crush force-crush distance curve. Although crush distance can be readily obtained from the simulation output, the value of crush force is derived from contact force. The contact force is calculated based on the displacement of interacting components and an associated fictitious spring between two contacting nodes (interface stiffness).

The proper selection of interface stiffness for the crush tube model becomes a challenging task when the material properties of the tube and barrier are not similar. For example, in most crush experiments, the load is applied by a steel block, which has a higher modulus compared to carbon-epoxy composite. In LS-DYNA, the interface stiffness can be calculated based on the master, slave or the minimum of the two. Due to the fact that the stiffness property is degraded in the contacting elements, using any of these options for interface stiffness calculation would either overestimate or underestimate the crush force. Another method is to calculate the interface stiffness based on the time step size and the nodal mass of the contacting surfaces, which does not depend on the stiffness of either the master or slave surfaces.

Our goal in this research is to accurately model the crush response of polymer composite crush tubes. Through proper coupling of GENOA/PFA with LS-DYNA, we were able to find crush patterns that are similar to those found in physical experiments. However, the energy absorption estimations are still not very accurate and require further effort. The work presented in this section is tied closely to that in the previous section as we intend to examine the role of nano-enhanced matrix materials in improving the crush performance of composite crush tubes.

Conclusions

Good progress has been made in multiple fronts. We were able to develop an analytical model to predict mean crush force of multi-corner metallic tubes, perform multilevel decomposition and optimization of a product-material system, conduct coupled simulations involving both the manufacturing process and the subsequent product performance analysis, develop tools to model mechanical characteristics of polymer matrix materials with nano-inclusions, and perform crush simulation of polymer composite tubes. We are moving towards our goal of coupled process-material-product simulation and optimization with multi-scale material models.

Presentations/Publications/Patents

1. Acar, E., Rais-Rohani, M., and Eamon, C., "Structural Reliability Analysis using Dimension Reduction and Extended Generalized Lambda Distribution," *International Journal of Reliability and Safety* (in press, 2009).
2. Acar, E., Solanki, K., Rais-Rohani, M., and Horstemeyer, M., "Uncertainty Analysis of Damage Evolution Computed Through Microstructure-Property Relations," *Journal of Probabilistic Mechanics* (accepted, 2009).
3. Kim, S-G., Horstemeyer, M., Baskes, M., Rais-Rohani, M., Kim, S., Jelinek, B., Houze, J., Moitra, A., and L. Liyanage, "Semi-empirical Potential Methods for Atomistic Simulations of Metals and Their Construction Procedure," *Journal of Materials Engineering and Technology* (in press, 2009).
4. Solanki, K., Acar, E., Rais-Rohani, M., Horstemeyer, M., and Steele, G., "Product Design Optimization Using Microstructure-Property Relations and Associated Uncertainties," *International Journal of Design Engineering*, Vol. 2, No. 1, 2009, pp. 47-79.
5. Acar, E., Rais-Rohani, M., Najafi, A., Marin, E., and Bammann, D., "Concurrent Design of Product-Material Systems using Multilevel Optimization," Proceedings of the 5th AIAA Multidisciplinary Design Optimization Specialists Conference, Palm Springs, CA, May 4-7, 2009.

6. Najafi, A., Axial Collapse of Thin-Walled, Multi-Corner, Multi-Cell Tubes, an MS Thesis, Mississippi State University, August 2009.
7. Rouhi, M., Topology Optimization of Continuum Structures Using Element Exchange Method, an MS Thesis, Mississippi State University, May 2009.

References

1. Bradshaw RD, Fisher FT, Brinson LC. 2003. Fiber waviness in nanotube-reinforced polymer composites: II. Modelling via numerical approximation of the dilute strain concentration tensor. *Compos Sci Technol* 63(11):1705-22.
2. Dowling NE. 1999. Mechanical behavior of materials, engineering methods for deformation, fracture, and fatigue. 2nd ed. NJ: Prentice Hall. Chap. 9.
3. Fisher FT, Bradshaw RD, Brinson LC. 2003. Fiber waviness in nanotube-reinforced polymer composites—I: modulus predictions using effective nanotube properties. *Compos Sci Technol* 63(11):1689-1703.
4. Garg M, Abdi F, McHugh S. Analyzing interlaminar shear strength of multi-scale composite via combined finite element and progressive failure analysis approach. In: SAMPE Fall Technical Conference on Multifunctional Materials; 2008; Memphis, TN.
5. Horstemeyer MF. 2001. From atoms to autos, a new design paradigm using microstructure-property modeling, part 1: Monotonic loading conditions. Sandia National Laboratories, Rep. No. Sand2000-8662.
6. Kim MK, Michelena NF, Papalambros PY, Jiang T. 2003. Target cascading in optimal system design. *J Mech Des* 125:474-80.
7. Michelena NF, Kim HM, Papalambros PY. A system partitioning and optimization approach to target cascading, In: Proceedings of the 12th International Conference on Engineering Design. 1999; Munich, Germany.
8. Najafi A, Rais-Rohani M. Influence of cross-sectional geometry on crush characteristics of multi-cell prismatic columns. In: Proceedings of the 49th AIAA/ ASME/ASCE/AHS/ASC Structures, Structural Dynamics, and Materials Conference; 2008 Apr 7-10; Schaumburg, IL.
9. Tandon GP, Weng GJ. 1984. The effect of aspect ratio of inclusions on the elastic properties of unidirectionally aligned composites. *Poly Compos* 5:327-33.
10. Thostenson ET, Li WZ, Wang DZ, Ren ZF, Chou TW. 2002. Carbon nanotube/carbon fiber hybrid multiscale composites. *J Appl Phys* 91(9):6034-37.
11. Wierzbicki T, Abramowicz W. 1989. The mechanics of deep plastic collapse of thin-walled structures. In: Wierzbicki T, Jones N, eds. Structural failure. p. 281–326.

Acknowledgments

The contributions of research assistants: Dr. Erdem Acar, Ali Najafi, Mohammad Rouhi, and Cynthia Tamasco are gratefully acknowledged.

L. Fatigue of Lightweight Automotive Materials in the Southern Regional Center for Lightweight Innovative Designs (SRCLID)

Principal Investigator: J.Brian Jordon
Co-Principal Investigator: Mark. F. Horstemeyer
Center for Advanced Vehicular Systems (CAVS)
Mississippi State University (MSST)
206 Carpenter Bldg., PO Box ME
Mississippi State, MS 39762
(662) 325-8977; e-mail: bjordon@cavs.msstate.edu

Technology Area Development Manager: Dr. Carol Schutte
(202) 287-5371; e-mail: carol.schutte@ee.doe.gov

Project Manager: Magda Rivera
(304) 285-1359; e-mail: magda.rivera@netl.doe.gov

Contractor: Mississippi State University
Contract No.: DE-FC26-06NT42755

Objective

Develop design and prognostic tools for fatigue of lightweight automotive components.

Approach including industrial partner/collaborator and path to technology transfer and commercialization

The major portion of the fatigue life involves the incubation and growth of a small crack, which is profoundly influenced by the microstructural features, such as void or intermetallic inclusions, grain size, orientation or dendrite size, and second arm spacing, etc. In terms of modeling, a crack growth model relies heavily on accurately modeling the incubation and growth of a microstructurally small crack, including the influence of microstructural features such as grain boundaries and particles. Thus, the approach of this task can be decomposed into the following main tasks:

- Fatigue testing and characterization
- Simulations of fatigue crack initiation and growth
- Fatigue life model development and predictions
- Modeling calibration and validation
- Transfer of the experimental data and fatigue models (industrial partners for this task are General Motors and Ford)

Milestone, Metrics, and Accomplishments

- Task 3.1 – Perform strain-life tests with various means stress level for AM30.
 1. Conducted strain-life tests of Mg AM30 from various locations of GM rail.

- *Task 3.2 – Perform strain-life tests with various means stress level for AZ61.*
 1. Developed a detailed test plan for the tensile and fatigue specimens to be machined from Mg AZ61 alloy.
 2. Performed tensile testing on Mg AZ61 alloy in the extruded and transverse directions.
 3. Conducted strain-life tests of Mg AZ61 alloy in the extruded and transverse directions.
- *Task 3.3 – Perform long crack growth tests of the alloys selected.*
 1. Conducted long crack test via compact tension specimens for Mg AZ31 alloy.
- *Task 3.4 – Conduct micromechanical simulations on the cyclic behavior the Mg alloy using a developed ISV model.*
 1. Conducted simulations to evaluate the stress field around a crack tip.
- *Task 3.5 – Conduct the finite element analysis for opening stress induced by crack tip plasticity for AM30 wrought Mg alloy using a developed crystal plasticity model.*
 1. Conducted simulations of crack growth under various crystal orientations.
- *Task 3.6 – Examine fracture surfaces.*
 1. Examined and quantified the source of fatigue crack initiation on Mg AM30 GM rail.
 2. Determined structure-property relationships between microstructure features and fatigue life.
- *Task 3.7 – Develop multistage fatigue models for the AM30 and AZ61 wrought Mg alloys.*
 1. Developed multistage fatigue model for AM30 and AZ61 alloys.
 2. Incorporated structure-property relationships into the MultiStage Fatigue model to predict the scatter in the fatigue life.
 3. Generated fatigue life predictions based on specific microstructure information of Mg AM30 alloy.
- *Task 3.8 – Validate the models with components specified by sponsors.*
 1. Identified component for validation purposes.
- *Task 3.9 – Fatigue experiments for a joint specified by sponsor.*
 1. Developed test matrix and test specimens for Mg friction stir spot weld lap-joint coupon testing.
 2. Conducted monotonic and cyclic lap-joint testing on Mg friction stir spot welds.
 3. Characterized fracture mode and path of Mg friction stir spot welds.
- *Task 3.10 – Develop a first order fatigue model for a joint based on fatigue experiments and joint simulations.*
 1. Implemented crack growth model for predicting fatigue life of lap-joint of Mg friction stir spot welds.
- *Task 3.11 – Provide service loading spectrums and key loading conditions and specify on materials and joints of interests (GM and FORD).*
 1. Working with industry partners to determine their needs for spectrum loading.

Future Direction

- Continue material testing and modeling of friction stir spot welds including:
 1. Crack growth characterization.
 2. Crack initiation.
 3. Microstructural evaluations.
 4. Conduct round-robin fatigue tests of Mg friction stir spot welds.
 5. MSF model adaption to spot welds.
- Continue material testing and modeling of Mg AZ61 and AM30 extrusions.
 1. Evaluate grain size, orientation and distribution and particles sizes.
 2. Complete the monotonic and cyclic stress-strain tests on the given extrusion samples.
- Generate small crack data on AZ61 and AM30 coupons to study fatigue incubation and crack-growth behavior
- Evaluation structure-property relations of AZ31 alloy based on fracture surfaces.
- Perform MSF analyses of the uniaxial, strain-controlled fatigue tests on unnotched Mg coupons.
- Conduct Multi-axial fatigue of Mg AZ31 alloy.
- Microstructure influence on fatigue cast Mg alloys.
- Validate fatigue models.

Introduction

Due to an increased interest to achieve a reduction in green house gases through improvements in fuel economy in automobiles, lightweight materials have become the focus of recent research. At the forefront of this effort are magnesium alloys. The high strength-to-weight ratio of magnesium makes it a highly attractive alternative to traditional automotive industry metals. Due to the ease of production, most magnesium alloys employed in manufactured components are cast; however, wrought alloys typically have better mechanical properties and are typically employed in structural components of the automobile. Thus, a need arises for a predictive tool that can capture the fatigue damage in wrought magnesium alloys with the intent of determining/designing the best alloy for use in a range of automotive applications. Therefore, the overarching goal of this task is the development of a physically-motivated microstructurally-based fatigue model.

In order to reach the goal of using more light weight metals in automobiles, understanding and modeling the fatigue damage of welded joints is of great importance. As with the base materials, research is needed to determine the reliability and performance of potential welding techniques and develop microstructurally-based modeling approaches. While research in the area of fatigue in friction stir spot welds is not unique, recent work has been exclusively focused FCC alloys and not HCP alloys such as magnesium.

Finally, the investigation of fatigue behavior of nanoscale materials has been of significant interest to many researchers due to the development of technologies of nano-materials. As such, understanding how fatigue damage initiates and grows at the nanoscale for magnesium alloys will lead to better modeling approaches at the higher length scales.

Structure-property Relations of Fatigue in Mg AM30 Alloy

The fatigue properties of an AM30 magnesium alloy extruded into a crash rail-shaped component were evaluated experimentally and numerically. Fully-reversed, strain control fatigue tests were conducted on specimens extracted from regions having a varying grain size and texture. Using scanning electron microscopy, the fracture surfaces of each failed specimen were analyzed in order to establish the relationship between microstructure and fatigue behavior. Texture and grain size were identified through EBSD analysis. Parallels between microstructural features such as particle size, grain size, Taylor Factor, and the number of cycles to failure were determined. The numerical analyses concerned simulation of the fatigue life to failure using a microstructure-based multistage fatigue model originally developed for cast aluminum alloys and later adapted for magnesium.

The microstructure anisotropy associated with the extruded rail contains non-uniform texture and grain sizes as a result of the extrusion process. Due to the speed of the extrusion, limited recrystallization occurred and thus microstructural heterogeneities developed. As such, the average grain size and initial Taylor Factor based on electron backscatter diffraction (EBSD) results of the rail were measured and are shown in [Figure 1](#). The fatigue specimens tested as part of this study were taken from the six regions indicated in Figure 1 and labeled as A, B, C, E, G, and I. Post-mortem fractography was conducted on fatigue specimens tested under fully-reversed constant strain amplitudes of 0.003mm/mm in ambient temperature and humidity. Each of the fracture surfaces were examined under a scanning electron microscope (SEM) with the intent to determine the sources of crack initiation. [Figure 2](#) shows a typical intermetallic particle that initiated the fatigue crack. Chemical analysis of the intermetallics revealed that the particles were composed of Mg-Al-Mn compounds. As such, these types of particles are more brittle than the surrounding matrix and tend to fracture rather than debond. Fracturing of the intermetallic particles was observed on all of the surfaces imaged via the SEM, and no evidence of debonding was observed. Furthermore, all of the particles were found to be located on the surface of the specimen, and no subsurface particles initiated a fatigue crack. Each of the cyclic failures stemmed from only one particle and not multiple particles. Also observed in the SEM images was evidence of twinning on the fatigue fracture surfaces similar to literature (Begum et al. (2008) and Fan et al. (2009)).

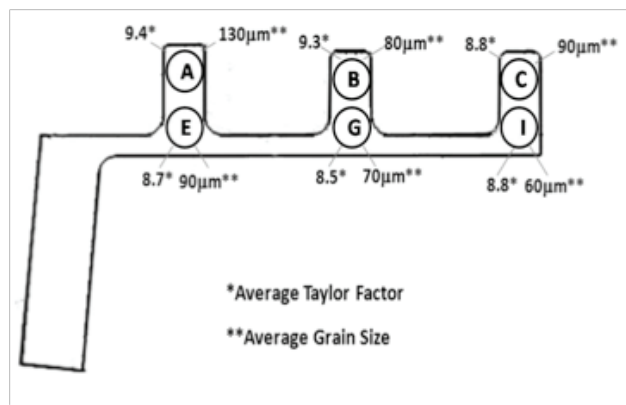


[Figure 1](#). The average grain size and Taylor Factor in the extruded magnesium AM30 obtained using EBSD analysis.

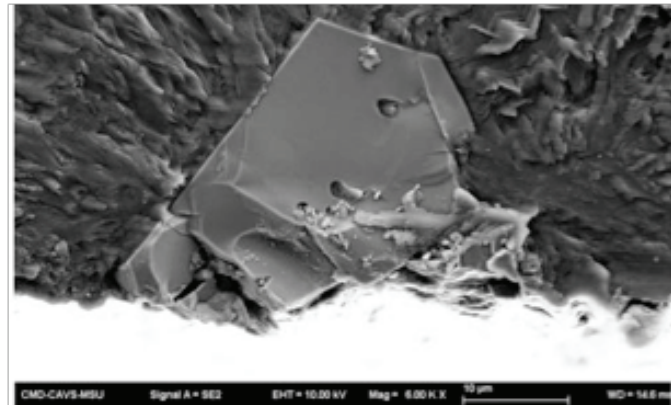


[Figure 2](#). Typical Post-mortem fractograph of magnesium AM30 aluminum alloy that shows the intermetallic particle that initiated the fatigue crack.

Part of the objective of this study was to correlate structure-property relationships to microstructure features with the intent to predict the scatter that is typically observed in fatigue studies. The square root particle area versus the number of cycles to failure are shown in [Figure 3a](#). The trends of both the square root particle area versus failure cycles show that specimens with smaller particles had greater fatigue resistance compared to specimens with larger particles and specimens with smaller particles had better fatigue life. To further characterize

the microstructure of the AM30 alloy in regards to the fatigue behavior, the average grain size and initial Taylor Factors are plotted against the number of cycles to failure. Figure 3b displays the number of cycles versus average grain size. While this plot displays significant scatter, the trend suggests that the alloy exhibits greater fatigue resistance for smaller grains compared to specimens with larger grains. This conclusion is not unexpected considering grain boundary blocking can slow the rate of crack growth.

Likewise, Figure 3c shows that the smaller Taylor Factor values resulted in generally higher fatigue lives. While Fig 3c also displays some level of scatter, the trend suggests that the alloy exhibits greater fatigue resistance for smaller initial Taylor Factors compared to specimens with larger Taylor Factors. The calculation of the Taylor Factor, which is calculated by taking the summation of the amount of shear of the active slip system and then normalizing by the deformation step (Raabe (1995)), represents basically how susceptible the slip shear systems are to shear deformation. Thus, higher initial Taylor Factors mean more local shear compared to lower Taylor Factors. Since crack initiation is dependent on local shear strain, higher Taylor Factor values suggest that crack initiation will occur earlier compared to lower Taylor Factors.

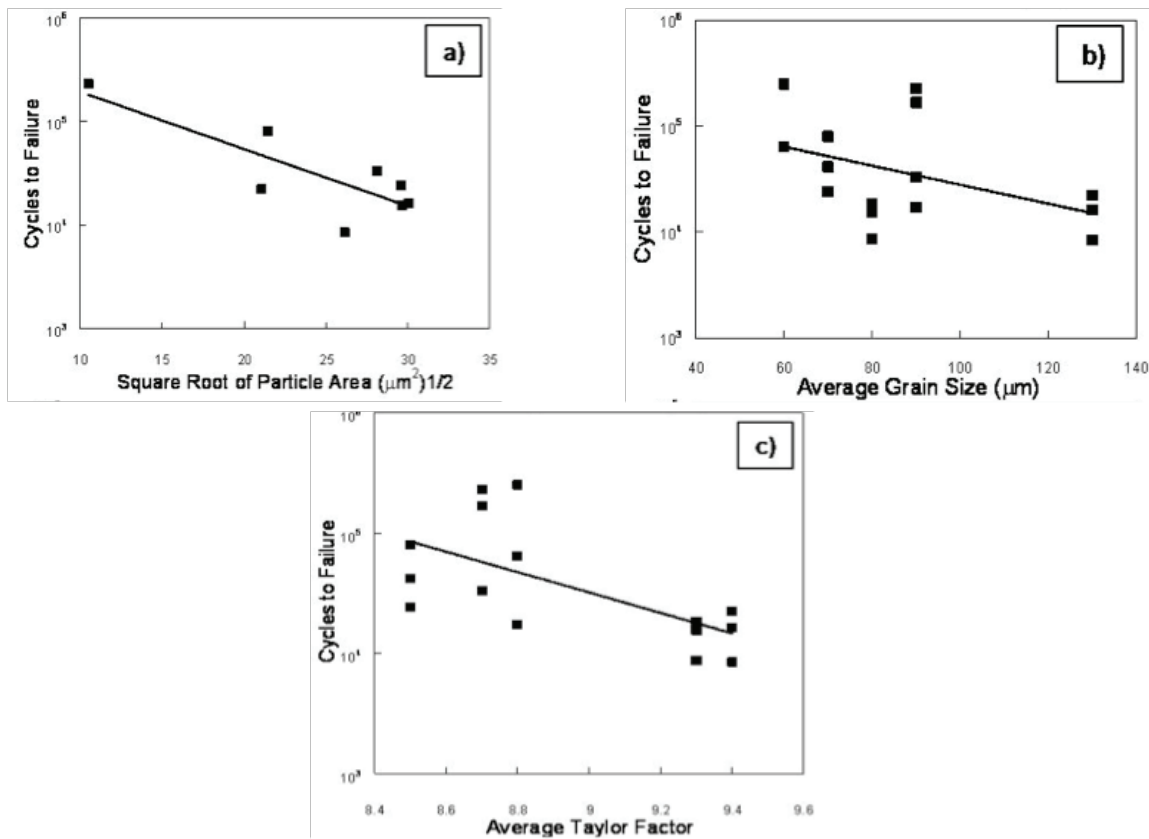


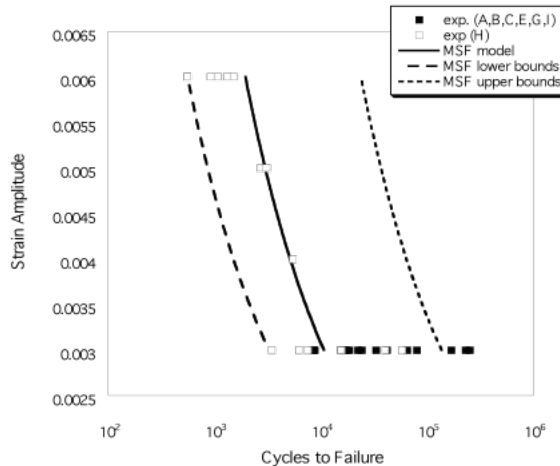
Figure 3. Number of cycles to failure versus the square root of the particle area(a), average grain size (b), and average Taylor Factor (c).

Fatigue Modeling

Microstructurally-based fatigue damage predictions on various aluminum and magnesium alloys have been successfully modeled (cf. McDowell et al. (2003)) using a multistage approach. This approach incorporates three stages of fatigue damage evolution at various scales (McDowell et al. (2003)): nucleation; microstructurally small/physically small crack growth; and long crack growth. As such, the total fatigue life can be decomposed as

$$N_{\text{Total}} = N_{\text{Inc}} + N_{\text{MSC/PSC}} + N_{\text{L}}$$
 (1)

where N_{Total} is the total fatigue life. N_{Inc} is the number of cycles to incubate a crack at an inclusion, which can be a relatively large constituent particle, a large pore, or a cluster of each or both. While the MSF model has been correlated to magnesium alloys prior to this study, this modeling effort was focused on wrought magnesium where past work focused on cast alloys. As such, the main driving forces in cast alloys are primarily the casting pores (McDowell et al. (2003)). However, the material of interest is an extruded magnesium alloy that does not contain casting pores or oxide films. Thus, based on experimental results in this study, the primary source of fatigue damage is intermetallic particles. Figure 4 shows the MSF model results compared to the experimental data. The MSF results show a mean value and the lower and upper bounds based on the structure-property information obtained in this study.. For comparison purposes, additional fatigue results of extruded magnesium AM30 ($R=-1$) of various strain amplitudes are also shown (H).



There were two main fatigue mechanisms for the FSSW in magnesium AZ31 alloy. The nugget pull-out failure observed for the two maximum load levels tested (2.5 and 3.0kN, R=0) occurred because as the crack propagated circumferentially around the nugget, the shear/tensile stress in the remaining net area of the nugget increased with each advancement of the crack front. Once the crack had propagated around approximately half of nugget diameter, the shear/tensile stresses acting on the net area were such that the remaining cross section failed under shear/tensile overload. The second type of fatigue failure occurred when the maximum cyclic load was below 2.5kN. Once the crack had propagated circumferentially around the nugget, the crack then propagated outward through sheet material. Thus, the maximum net stress during the cyclic loading never exceeded the ultimate tensile/shear strength, which allowed the crack to propagate through the base material. Also, a secondary crack denoted as was also observed to initiate under the range of the load levels tested. However, this secondary crack propagated in the opposite direction of the primary crack propagation path. While this secondary crack was observed to propagate to the free surface, the crack eventually became non-propagating. Thus, the secondary crack was not considered in the fatigue modeling efforts.

Fatigue Modeling

Given the crack like nature of the interface shown in Fig. 5, the modeling approach presented here is $N_{\text{Total}} \approx N_{LC}$ based on the assumption that a majority of the fatigue life is consumed in the crack growth regime such that. This assumption is supported by previous fatigue of spot weld work (cf. Lin et al. (2008)). The basic approach employed here is to use a modified Paris law, which is based on a stress intensity factor, to calculate the number of cycles needed to grow the crack from the tip of the interfacial hook to the free surface of the spot weld. Since a stress intensity solution for the FSSW is not currently available, we used a method similar to Lin et al. (2008), in which a kinked crack stress intensity solution for RSW is employed.

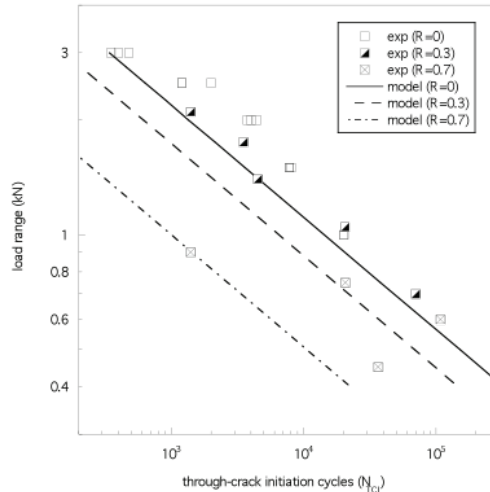


Figure 6. Through-crack initiation life results of friction stir spot welds tested at R=0, R=0.3, and R=0.7 compared to the crack growth model.

The crack growth model compared well, if not slightly conservative, with the FSSW through-crack fatigue-life results for the three R-ratios tested as shown in Figure 6. The conservative predictions of the model are likely due to modeling the crack growth from the tip of interfacial hook and not accounting for the crack growth in the interface leading up to the hook tip. The other obvious deviation of the model to the experimental results is in regards to the slope of the higher R-ratio tests—specifically R=0.3 and R=0.7. The R-ratio effect leads to a shift in the model prediction but does not change the slope of the prediction. However, the experimental results showed a decreasing slope versus load range as the R-ratio increased. This change in slope is likely due to crack closure, where at R=0.7, the crack is most likely fully open through the full load range. In contrast, at R=0, crack closure is the greatest and, as such, the slope of the prediction should be reflected in the model.

Fatigue Crack Propagation Simulations

The fatigue crack propagation behavior of magnesium single crystals at the nanoscale was analyzed using molecular dynamics simulation. The interatomic potential used in this investigation is Embedded Atom Method (EAM) potential. The studies of the mechanism of fatigue crack growth in different crystal orientation were performed using CC (center crack) specimens and EC (edge crack) specimens as shown in Figure 7. For CC specimen, the periodic boundary conditions were assigned in the x and z directions, while for the EC specimen, only the z direction was allowed periodic boundary conditions. Ten crystal orientations of initial crack, namely, orientation A-(110)[100], orientation B- (100)[110], orientation C-(100) [0001], orientation D-(110)[0001], orientation E-(0001)[100], orientation F-(0001)[110], orientation G (101)[012], orientation H (101)[110], orientation I (102)[101], and orientation J (102)[110] were analyzed for verifying the influences of the lattice orientation, strain rate, temperature, and grain boundary. In order to verify the effects of the grain boundary, the mechanism of fatigue propagation was also investigated in several bicrystal simulations. The development of dislocation and twin structure around the crack tip is also displayed by the simulation. The centrosymmetry parameter was used to highlight the defects including crack surface, slip band, and twin.

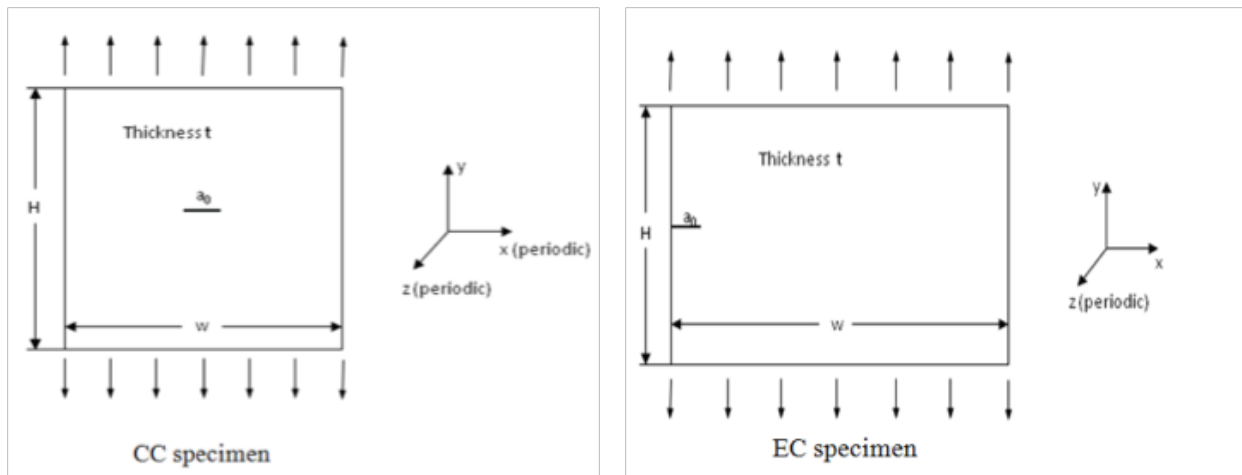


Figure 7. Specimens used for the simulation of fatigue crack growth.

The following major conclusions can be drawn according to the simulation results:

1. The mechanism of fatigue crack propagation is strongly dependent on the crystal orientations of the initial cracks. Different plastic deformation modes occurred at the crack tips in different crystal orientations.
2. The resistance of fatigue crack growth of Orientation B is the highest while the crack growth rate of Orientation D is the highest.
3. The dislocation emissions and twin bands occurring at the crack tips due to the stress concentration play major roles on the mechanisms of fatigue crack growth.
4. The fatigue crack growth rate decreased with an increasing strain rate (frequency).
5. The mechanism of fatigue crack growth in the Orientation A was strongly affected by the temperature, while the temperature does not have a significant influence on the mechanism of fatigue crack extension in other orientations. In the case of Orientation A, the propagation mechanism at high temperature was void nucleation ahead of the crack tip and the linkage of the void with the main crack. In general, the growth rate decreased with increasing temperature in all orientations except orientation A, B, and E.

6. The grain boundary exerts strong effects on the fatigue crack growth. The DF-horizontal grain boundary is the weakest. For the FD-vertical grain boundary, the twin band occurring at the crack tip was suppressed by the grain boundary, and, consequently, the fatigue crack growth was stopped. On the contrary, for the DF-vertical grain boundary, the plastic deformation zone at the crack tip was so small that the grain boundary had no resistance on the fatigue crack growth.
7. In the correlation of growth rate $da/dN = c\Delta CTOD$, the proportional constant c for different orientations was calculated by the atomistic simulations. The values of c for magnesium were much larger than those of copper reported in the previous studies on fcc crystals, implies that magnesium is a semi-brittle material.

Conclusions

The following is the main conclusion of the research realized in Task 3 for FY 2009:

- Fatigue of base magnesium alloys (AM30 and AZ61):
 1. In terms of fatigue crack initiation in extruded magnesium AM30 alloy, the fatigue crack initiation was dominated by intermetallic particles consisting of Mg-Al-Mn located at the surface. In general, the specimens that exhibited higher fatigue resistance typically had fatigue cracks that initiated from smaller intermetallics. Likewise, larger particles that initiated the fatigue cracks had lower cycles to failure. Mg-Al-Mn particles that initiated the fatigue cracks were observed to fracture rather than debond.
 2. For the AM30, greater fatigue life was generally associated with specimens that contained smaller grain sizes: the larger the average grain size, the lower the fatigue life.
 3. For the AM30, specimens with a lower average initial Taylor Factors exhibited a better fatigue resistance compared to specimens with a higher calculated Taylor Factor.
 4. The MultiStage Fatigue (MSF) model was adapted to capture the influences of the microstructural characteristics and influences of the extruded alloy. As such, the MSF model was able to predict the scatter of the fatigue results with good agreement for the Mg AM30 alloy.
 5. The Mg AZ61 alloy was tested under fully-reversed strain control in the transverse and the extruded directions. The experimental results show that the alloy exhibited differences between the transverse and the extruded direction with in the low strain amplitudes.
- Fatigue of friction stir spot welds:
 1. In terms of failure mode for the friction stir spot weld, the fatigue crack propagated through the tip of the interfacial hook, which the interfacial hook is a bi-product of the friction stir spot weld process. Once the crack grew past the hook tip, the crack grew along the maximum principle direction due the mixed mode loading and propagated to the free surface. The crack then propagated along the circumference and either failed due to a shear overload or continued to propagate through the width of the coupon.
 2. The crack growth approach to modeling the fatigue of the friction stir spot weld gave reasonable results despite the lack of a precise stress intensity factor solution.
 3. Based on the crack growth calculations performed here, the fatigue resistance of this friction stir spot weld can be improved by reducing the size of the primary interfacial hook.

- Molecular Dynamics Simulations of Magnesium:
 1. Simulations were performed on magnesium crystals under cyclic loading.
 2. Simulations results showed that growth of the crack was affected by the crystal orientation
 3. Simulations results showed that growth of the crack was affected by temperature.

Presentations/Publications/Patents

1. J. Jordon, M. Horstemeyer, S. Daniewicz, H. Badarinarayan, and J. Grantham. *Material Characterization and Modeling of Friction Stir Spot Welds in a Magnesium AZ31 Alloy*. J Eng Mater Technol. (Under review).
2. T. Tang and M. Horstemeyer. *Fatigue Crack Growth in Magnesium Single Crystals under Cyclic Loading: Molecular Dynamics Simulation*. J Comput Mater Sci. (Under review).
3. J. Jordon, M. Horstemeyer, and J. Grantham. Fatigue Behavior of Magnesium AZ31 in Friction Stir Spot Welds. In: ASME International Mechanical Engineering Congress and Expo; 2009 Nov 13-19; Lake Buena Vista, Florida.
4. J. Bernard, J. Jordon, and M. Horstemeyer. *Fatigue Structure-Property Evaluation of AM30 Magnesium Alloy*. TMS (The Minerals, Metals & Materials Society). (Accepted 2010 Feb).
5. J. Jordon, M. Horstemeyer, H. Badarinarayan, and J. Grantham. *Fatigue Evaluation of Friction Stir Spot Welds in Magnesium Sheets*. TMS. (Accepted 2010 Feb).
6. T. Tang and M. Horstemeyer. *Atomistic Simulations of Fatigue Crack Growth and the Influence of Temperature on Fatigue Behavior in Magnesium Crystals*. In: Proceedings of 2010 TMS Annual Meeting & Exhibition; 2010 Feb 14-18; Seattle, WA. (Accepted).

References

1. S. Begum, D. Chen, S. Xu, and A. Luo. 2008. *Strain-Controlled Low-Cycle Fatigue Properties of a Newly Developed Extruded Magnesium Alloy*. Metall Mater Trans A 39A:3014-26.
2. C. Fan, D. Chen, and A. Luo. 2009. *Dependence of the Distribution of Deformation Twins on Strain Amplitudes in an Extruded Magnesium Alloy After Cyclic Deformation*. Mat Sci Eng A 519:38-45.
3. D. Raabe. 1995. *Modeling of Active Slip Systems, Taylor Factors and Grain Rotations during Rolling and Compression Deformation of Polycrystalline Intermetallic L12 Compounds*. Acta Metallurgica et Materialia 43(4):1531-40.
4. D. McDowell, K. Gall, M. Horstemeyer, and J. Fan. 2003. *Microstructure-Based Fatigue Modeling of Cast A356-T6 Alloy*. Eng Fract Mech 70(1):49-80.
5. J. Newman and N. Dowling. 1998. *A Crack Growth Approach to Life Prediction of Spot-Welded Lap Joints*. Fatigue Fract Eng Mater Struct 21:1123-32.
6. P. Lin, J. Pan, and T. Pan. 2008. *Failure Modes and Fatigue Life Estimations of Spot Friction Welds in Lap-Shear Specimens of Aluminum 6111-T4 Sheets, Part 1: Welds Made by a Concave Tool*. Int J Fatigue 30(1):74-89.

M. A Modified LENS Process for Controlled Net Shaping-Induced Local Microstructure and Properties

Principal Investigator: Sergio Felicelli
Professor
Mechanical Engineering, Carpenter Engineering Bldg, Rm 210
Mississippi State, MS 39762
(662)325-1201; e-mail: felicelli@me.msstate.edu

Participant: Liang Wang
Assistant Research Professor
Center for Advanced Vehicular Systems, CAVS 2212
Mississippi State University, P.O. Box 5405
Mississippi State, MS 39762
(662)325-9235; e-mail: liangw@cavs.msstate.edu

Technology Area Development Manager: Dr. Carol Schutte
(202) 287-5371; e-mail: carol.schutte@ee.doe.gov

Project Manager: Magda Rivera
(304) 285-1359; e-mail: magda.rivera@netl.doe.gov

Contractor: Mississippi State University
Contract No.: DE-FC-26-06NT42755

Objective

- We aim to produce net shape alloy components with optimized as deposited microstructures by developing new manufacturing methodologies based on the Laser Engineered Net Shape (LENS) process.
- These methodologies aim to modify the thermal history of the material to control grain sizes and phase transformations. The modification of the thermal history will be guided by simulation tools that calculate optimized heat flux distribution and cooling rates, which can achieve a desired microstructure.
- To demonstrate our objective, we will explore different materials such as low alloy steels, stainless steels, and aluminum alloys, deposited in form of single walled builds and other geometries that can be representative of an actual component.

Approach

Our approach will proceed in the following sub-tasks:

Sub-Task 1:

- We will study the solidification phenomena occurring in the molten pool during the LENS process in order to predict the microstructure of the deposited material, including the formation of dendrites, grains, and pores.
- We will develop a solidification model that solves the transport equations in the pool using a combination of finite element and cellular automaton techniques.

- With the model, we will investigate the microstructure formation under different process parameters that affect the cooling rate during solidification.
- Given the temporary unavailability of our LENS machine, we will use an outside provider to obtain samples fabricated under different conditions. Stainless steel 316 will be initially used for this research.
- The microstructure of the samples will be characterized with SEM, XRCT, and optical microscopy in order to compare with model predictions.
- The validated model will then be used to explore new process conditions that result in a finer and more uniform microstructure and that can be confirmed experimentally in a systematic way.

Sub-Task 2:

- We will develop an in-house capability to build parts with the LENS machine at MSST. Currently, we have a LENS-750 old model donated to MSST by TARDEC in 2006. This machine has had a number of technical issues that have prevented us from building usable parts.
- A second machine, a newer 850M model, will come to MSST. This machine also has technical problems that need to be addressed, in particular, an improvement of the atmosphere control system.
- With the technical assistance of the manufacturer, we will make an assessment of what machine to keep and implement a course of action to have a working machine in the least amount of time possible.
- The possession of this in-house capability is considered essential to executing our fundamental research and design, performing necessary experiments, securing a fast supply of samples, and advancing our knowledge of this technology.
- In addition, the ability to operate our own LENS machine opens the possibility of using LENS in other projects at MSST or proposes joint research that involves this technology.

Accomplishments

- Porosity Characterization in 316L Stainless Steel LENS Deposits.
- Dendrite growth simulation development in the molten pool during the solidification in LENS
- Modeling study on cooling rate and primary and secondary dendrite arm spacing (PDAS/ SDAS)

Future Direction

- Allocate a new laser system (1kW IPG fiber laser) to CAVS and install to the current LENS 750 system.
- Apply the Lattice Boltzmann and cellular automaton techniques to simulate solidification under convection in the LENS process, with the goal of predicting DAS, grain size, and, possibly, phase transformations.
- Develop a thermal model to include double heat sources in order to control the cooling rate in the LENS process.

Introduction

Laser-assisted powder deposition, such as Laser Engineered Net Shaping (LENS), is a direct-metal rapid prototyping process in which metallic powder delivered by nozzles is melted by a laser beam (Lewis and Schlienger (2000); Griffith et al.(2000)). By moving the substrate or the laser beam, the structure can be built line by line into a wide variety of complex geometries. The LENS process produces a very small heat-affected zone (HAZ) and high cooling rates ($> 10^3$ °C/s). However, unless a careful tuning of the process parameters is performed, large pores can systematically form either at the interface separating two adjacent layers or within the bulk of the layer (Susan et al. (2006)). This issue keeps LENS technology from wider acceptance and application in industry.

The interlayer pores elongate along the layer boundaries but with an irregular free surface. It is believed that the presence of these pores can be generally attributed to a discrepancy in the temperature distribution in the deposited material behind the laser track. Unmelted powder could flow onto the colder underlying layer and cause a discrepancy in the melt pool hydrodynamics. This tendency of pore formation was in fact observed to be reduced by careful adjustment of the process parameters, such as laser power and laser scan speed (Wang and Felicelli (2007)); Kobryn et al. (2000)). Another important phenomenon could stem from the mechanical properties of the underlying layer. It was observed that a relatively low ductility of the deposited material correlates with more interlayer porosity (Groh (2006)).

The intralayer pores were observed to systematically take a spherical form and not to occur in specific locations related to the microstructure. The intralayer pores are still nearly impossible to control, and the mechanisms of their formation are still not formally understood (Smugeresky et al. (2007)). It is possible that the gas dissolved or entrapped in the melt may not have sufficient time to escape to the top of the melt pool due to rapid solidification rates associated with typical laser processing. The possible sources of the enclosed gas include surface contamination, entrainment during turbulent impact of particles into the molten pool, contamination by powder-feed gases, gases contained within the powder particles, or vaporization of high vapor pressure alloy constituents. A recent study suggests that the starting powder with certain critical level of porosity and gas content plays an important role on the intralayer porosity formation (Susan et al (2006)). Choi and Chang (2005) have statistically analyzed the pore distribution for an AISI H13 tool steel and suggested that the powder mass flow rate is a significant factor to porosity creation.

The microstructure of LENS parts, which is determined by the thermal history and also controls the mechanical properties, has gained much attention, and many experiments have been conducted to analyze the microstructure, especially the grain size (DAS for columnar dendrite) and morphology. Experimental results have proven that very fine microstructures can form due to the high cooling rates and temperature gradients. Ghosh and Choi (2006) deduced an equation that describes the relationship between the DAS and the thermal behaviors, and, based on the equation, the DAS was calculated to evaluate the microstructure. Very few papers (Grujicic et al. (2001); Miller et al. (2001)) were published on the numerical modeling of the microstructure evolution during the solidification and solid-state phase transformation while cooling down to room temperature, with scarce or no details on the dendrite morphology and growth process.

In this work, we investigated the porosity characterization in 316L LENS single wall deposits with optimized process parameters in order to attempt pore-free samples. The samples were analyzed with Optical Microscopy, X-ray CT, and SEM. A new finite element cellular automaton technique is developed that is able to capture the evolution of the fine microstructure occurring during solidification in a LENS pool. The model can predict the microstructure evolution of the solidification process, DAS and dendrite morphology, and the influence of LENS process parameters on the solidification.

Porosity Characterization in 316L Stainless Steel LENS Deposits

A considerable amount of work has been done with 316L stainless steel atomized powder using a LENS machine. It has been claimed that samples made with 316L are essentially pore free. However, the fact is that it is still unreliable to produce pore-free samples with 316L since the formation of porosity is very sensitive to the process parameters, including the laser power, travel speed, powder type, powder feed rate, melt pool size, open and closed loop control, hatch spacing (spacing in the x-y plane, deposit track overlap), and layer height increment (layer thickness). It is essential to tune up the process in order to eliminate porosity, which is a time and cost consuming process and keeps the LENS technology from wider acceptance and application in industry. Therefore, it is important to understand the fundamental mechanisms of porosity formation to produce pore-free samples consistently.

In this work, a preliminary study has been performed to investigate the porosity characterization in 316L LENS deposits. Three LENS-deposited cylindrical samples were made with optimized process parameters in order to procure pore-free material. All samples were produced at the facilities of Ice Prototyping & Fabrication, Inc. The geometry was 9.5 mm diameter and 50 mm long. The parameters are 0.25 mm layer thickness, and 0.38 mm hatch spacing at 500 mm/min travel speed. The argon mass flow rate is 20 lpm, and the nozzle purge rate is 22 l/min. The oxygen content in the chamber is 4 ppm. For the laser power, the amps were measured to correlate to the 208V, three phase input power consumed by the laser power supply. Typically, 38A is about 600 W of laser power and loses approximately 50W per every 2A drop along the portion of the power curve. For the present study, the laser power is about 550W with 36A.

The samples were analyzed with Optical Microscopy, X-ray CT, and SEM. The size distribution and area fraction of pores and sample microstructure were obtained. All samples showed a large amount of pores. The 1st and 2nd samples were analyzed by OM and SEM; the 3rd sample was analyzed with X-ray CT. [Figure 1](#) shows the diagram of the three samples. The cross sections of Sample 1 ([Figure 2](#)) shows large pores with size of 50 ~ 240 μm . A rather regular pore distribution in a cross section of Sample 2 can be seen in [Figure 3](#). The 3D representation of porosity using the results of X-ray CT is presented in [Figure 4](#). The pores are represented with spots within a representative central portion of the sample, i.e., 4.0 mm in diameter and 12 mm in length. The volume fraction of pores is 0.1% in [Figure 4\(a\)](#) and 0.02% in [Figure 4\(b\)](#). It is noted that both gas pores and interlayer pores were present in the samples. [Figure 5](#) shows cross-section scanning electron microscopy (SEM) images of pores in Sample 1. It can be seen that unmelted powder is present inside the pores. [Figure 6](#) shows the area percentage of pores at different locations. The area percentage of pores is in the range of 0.02 – 0.18%. More pores are present close to the substrate due to lack of fusion between layers in this region.

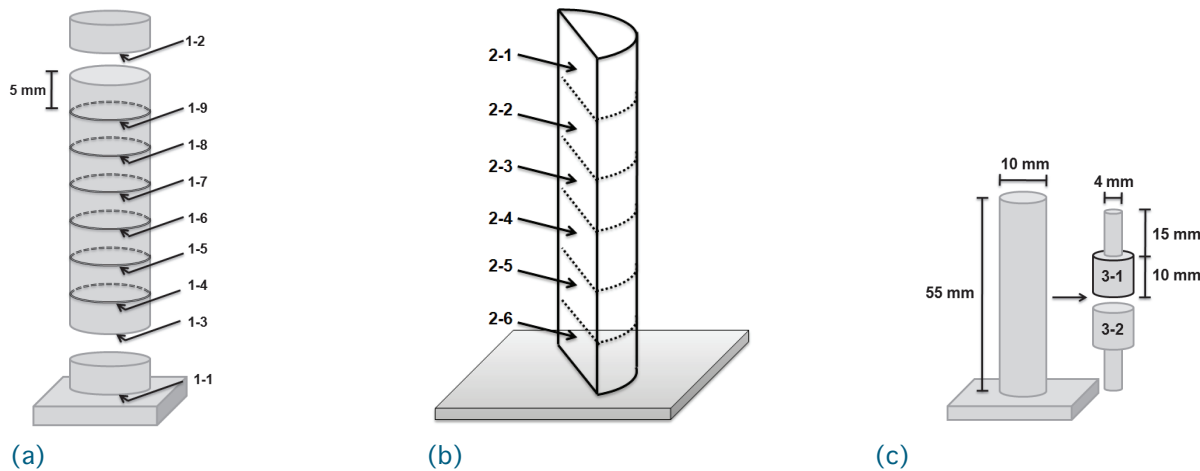
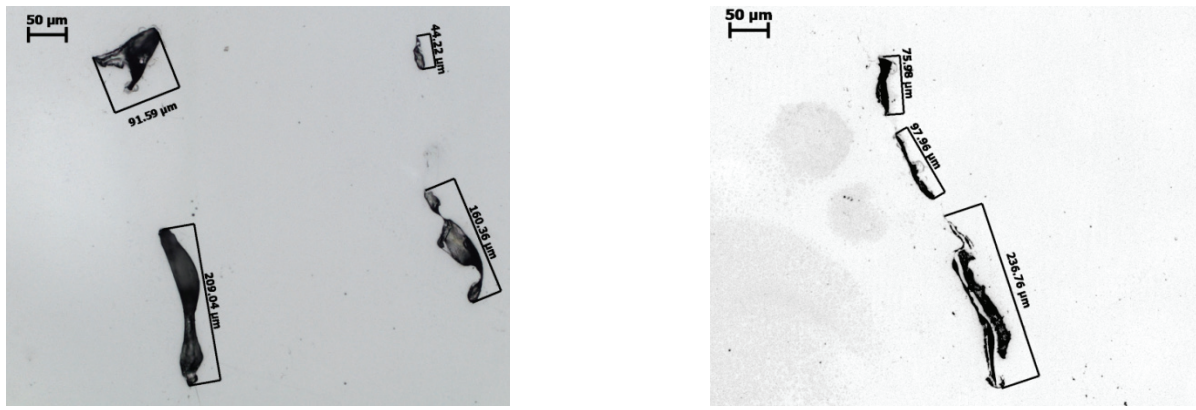


[Figure 1. Schematic of LENS samples.](#)



(a)

(b)

Figure 2. Cross-sections of Sample 1 showing typical pore/void with size of $50 \sim 240 \mu\text{m}$.

Figure 3. Cross-section of Sample 2 showing that pores appear to have a regular distribution.

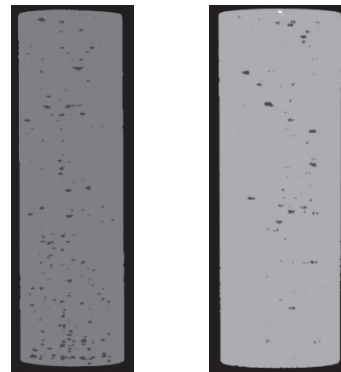


Figure 4. Typical pore distribution in Sample 3 with X-ray CT.

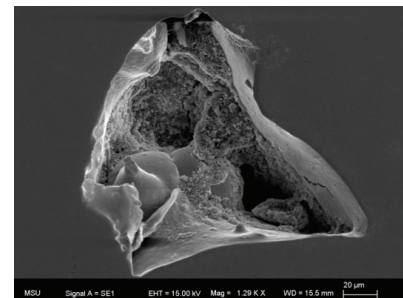
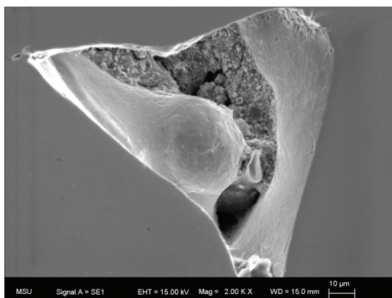


Figure 5. Scanning electron microscope images of pores in sample 1.

In a future study, more samples will be made by adjusting parameters to build fully-dense materials. It should be noted in Figure 3 that there seems to be some ordered pattern in the voids, which align with the hatch spacing of 0.38 mm. A first test will be to increase the laser power while holding all other parameters the same as before to investigate the effect, and a second test will be to decrease the hatch spacing while maintaining all other parameters to observe the effect.

Based on the work mentioned above, we received two additional samples using optimized parameters by increasing the laser power in order to procure pore free samples. The samples are labeled #4 and #5. Sample #5 was run at a higher power, 38 amps versus 36.5 amps for the previous samples, with all other parameters the same. Sample #4 was built with a tighter horizontal hatch spacing, 0.30 mm versus the previous 0.38 mm, with all other parameters the same. However, both samples showed a large amount of pores. Figure 7 shows the pore distribution of the cross section of one of the samples.

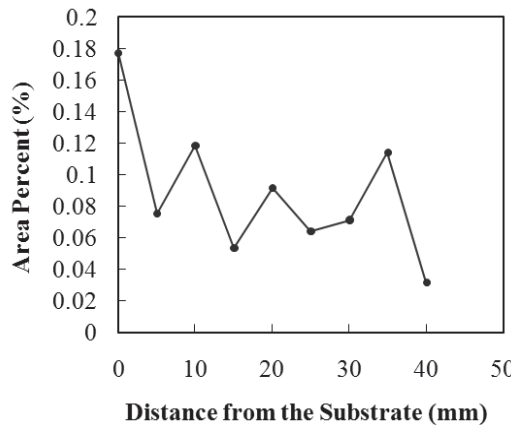


Figure 6. Area percent of porosity for different locations.

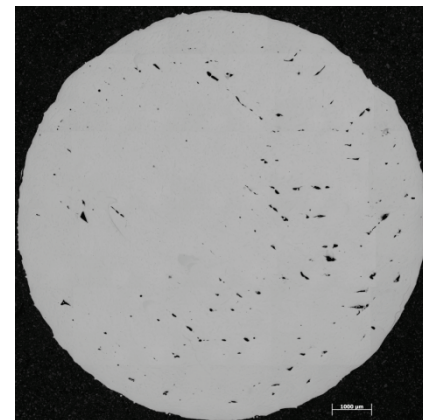


Figure 7. Cross-section of Sample 4 showing large amount of pores.

Dendrite growth in the molten pool during the solidification in LENS - Cooling rate and primary and secondary dendrite arm spacing (PDAS/ SDAS)

The SDAS and PDAS for various cooling rates were determined by examining the simulated dendritic structure in this model. Figure 8 shows the relationship between the cooling rates and the SDAS and PDAS, respectively, both of which indicate that the SDAS and PDAS decrease with increasing cooling rates. The experimental relationship between the SDAS and cooling rate for SS310 from Ref.12 and the experimental data for Fe-Ni-Cr ternary alloys by Electron-Beam Surface melting from Ref.13 were also plotted in Figure 8(a), showing a similar trend with the simulated curve and good agreement for a low cooling rate. A new equation describing the relationship between the cooling rate and SDAS is proposed by fitting the calculation data as indicated in Figure 8(a). The simulated PDAS are significantly higher than the SDAS, reaching values as large as 20 μm for the lower cooling rates. The calculated values of PDAS are also supported by the measured data by Elmer et al. (1989) as shown in Figure 8(b).

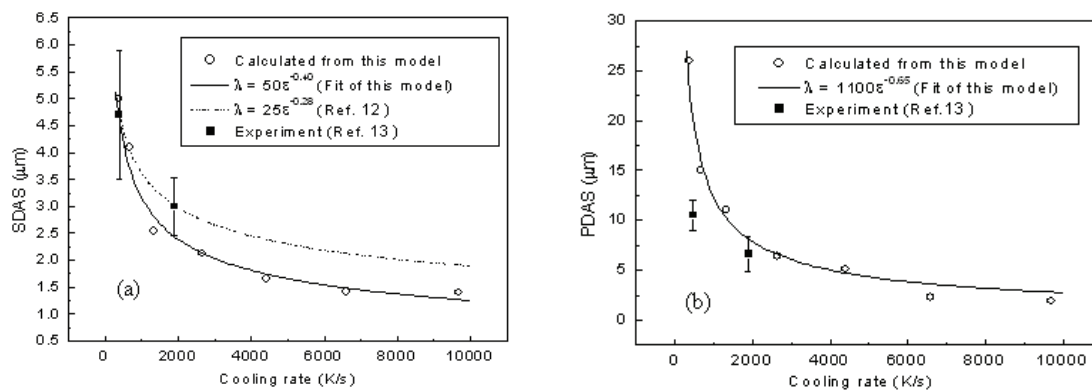


Figure 8. Cooling rate varies with (a) SDAS; (b) PDAS.

Effect of laser travel speed on the dendrite morphology

A single layer of 0.25 mm is deposited over a 5 mm thick substrate. In the calculation, in order to keep approximately a constant size of the molten pool, a higher laser power was used for a faster laser speed as in several experimental and modeling works.

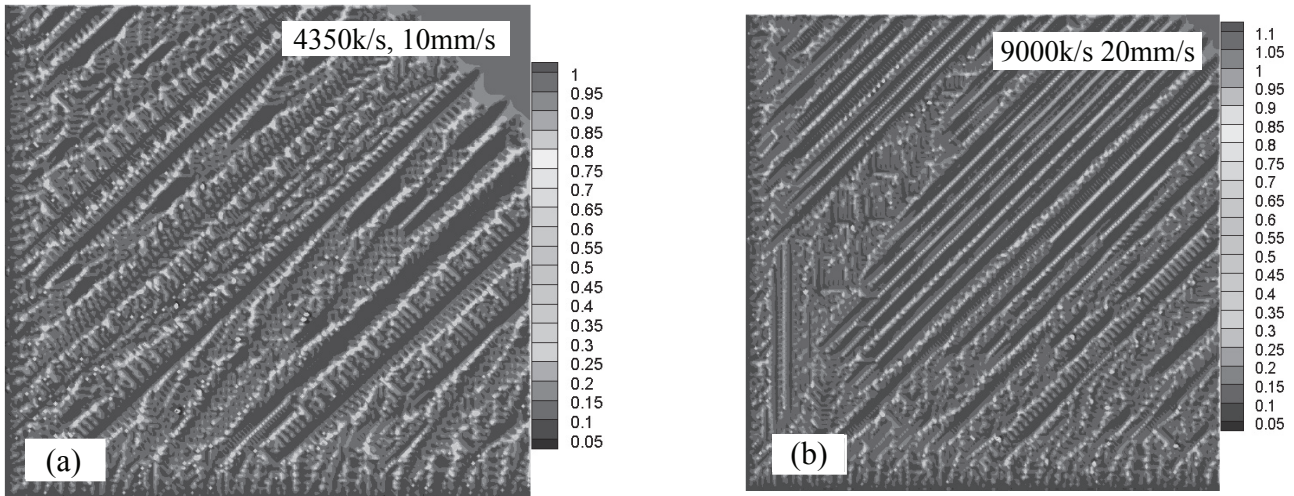


Figure 9. Dendrite morphologies with different laser travel speed, (a) 10 mm/s; (b) 20 mm/s.

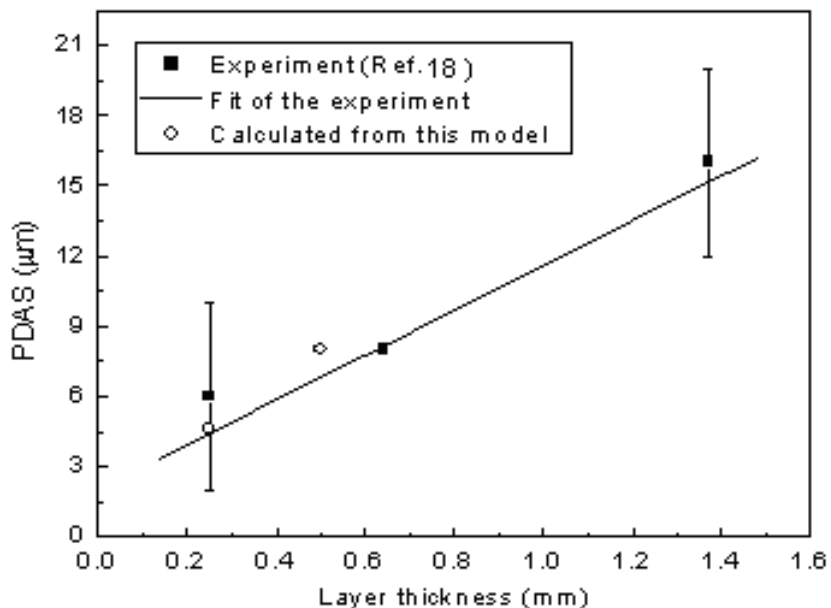


Figure 10. The simulated PDAS by this model, indicated as hollow circle, is plotted against the layer thickness for Fe-0.13wt%C as compared with the data for H13 from Mazumder et al. (1999).

Figure 9 shows the solidification microstructure in the small square domain located in the lower region of the molten pool for different travel speeds of the laser beam. The bar scale on the right denotes solute concentration of carbon in wt%. The figures clearly show columnar-type dendritic growth. Both the PDAS and SDAS decrease by increasing the scan speed of the laser beam. Due to the extremely high cooling rate and the narrow PDAS (less than 5 μm shown in Figure 9(b)), formation of secondary and tertiary arms is not always possible, and the interesting dendrite-to-cellular transition is observed. Previous experimental works (Kobryn et al. (2000); Zheng et al. (2008)) have confirmed that both a finer microstructure and a higher cooling rate were obtained by increasing the laser travel speed. Pal (2000) observed that dendrites and cells coexist in laser welded 316L with scanning speed of 15 mm/s. Pan et al. (1998) conducted laser deposition experiments with a scanning speed of 50.2 mm/s and observed the directional

growth of cells within the center part of the molten pool. In actual depositions, the laser power is constant and if the laser moving speed is increased, a smaller pool size will be obtained, which results in a higher cooling rate and smaller dendrite size. In [Figure 10](#), the simulated PDAS obtained by our model for a layer thickness of 0.25 mm and 0.5 mm (hollow circles in Figure 10) on Fe-0.13wt% C is compared with the experimental data on H13 from Mazumder et al. (1999), showing a very good agreement with the measured data.

Conclusions

- The porosity characterization was investigated in 316L LENS deposits. Five LENS-deposited cylindrical samples were made with optimized process parameters to attempt to procure pore-free materials.
- The formation of porosity is very sensitive to the process parameters, including the laser power, travel speed, powder type, powder feed rate, melt pool size, open and closed loop control, hatch spacing (spacing in the x-y plane, deposit track overlap), layer height increment (layer thickness), etc.
- The results showed that the area percentage of pores was in the range of 0.02 – 0.18% in the samples examined in this study. More pores are present close to the substrate due to the lack of fusion.
- The columnar grain growth process was simulated by a developed solidification model that coupled the FE method and CA technique for single layer deposition.
- The simulation results showed that the DAS can be as small as a few microns. An empirical relation between the DAS and the cooling rate was proposed based on the modeling and experimental results.
- The DAS, including PDAS and SDAS, decrease with increasing cooling rates. With an increasing laser travel speed of the laser beam, the cooling rate increases, this leads to the decrease of the PDAS and SDAS. When a thicker layer is deposited, the DAS decreases.

Presentations/Publications/Patents

1. Yin H, Felicelli SD. Dendrite growth simulation during solidification in the LENS process. *Acta Materialia*. (Accepted).
2. Wang L, Pratt P, Felicelli SD, El Kadiri H, Berry JT, Wang PT, Horstemeyer MF. Pore formation in laser-assisted powder deposition process. *J Manuf Sci Eng* 2009; 131(5):051008 (9 pages).
3. Wang L, Felicelli SD, Craig JE. Experimental and numerical study of the LENS rapid fabrication process. *J Manuf Sci Eng* 2009; 131(4):041019 (8 pages).
4. Pratt P, Felicelli SD, Wang L, Hubbard CR. Residual stress measurement of LENS AISI 410 thin plates via neutron diffraction. *Metall Mater Trans A* 2008; 39A:3155-63.
5. Wang L, Felicelli SD, Pratt P. Residual stresses in LENS-deposited AISI 410 stainless steel plates. *Mater Sci Eng A* 2008; 496:234-41.
6. El Kadiri H, Wang L, Horstemeyer MF, Yassar R, Berry JT, Felicelli S, Wang PT. Phase transformations in low-alloy steel laser deposits. *Mater Sci Eng A* 2008; 494:10-20.

7. Yin H, Wang L, Felicelli SD. Comparison of 2D and 3D thermal models of the LENS® process. ASME J Heat Transfer 2008; 130(10):102101-1-7.
8. Wang L, Felicelli SD, Gooroochurn Y, Wang PT, Horstemeyer MF. Optimization of the LENS® process for steady molten pool size. Mater Sci Eng A 2008; 474:148-56.
9. Wang L, Pratt P, Felicelli SD, El Kadiri H, Berry JT, Wang PT, Horstemeyer MF. Experimental analysis of porosity formation in laser-assisted powder deposition process. In: Supplemental proceedings: Volume 1: Fabrication, materials processing and properties. Warrendale (PA): TMS; 2009. p. 389-96.
10. Wang L, Pratt P, Felicelli SD, El Kadiri H, Berry JT, Wang PT, Horstemeyer MF. Pore formation in laser-assisted powder deposition process. 2008 Sept. CAVS Report #MSST.CAVS. CMD.2008-R0003; Center for Advanced Vehicular Systems, Mississippi State, MS.

References

1. Choi J, Chang Y. 2005. Characteristics of laser aided direct metal/material deposition process for tool steel. Int J Mach Tools Manuf 45:597-607.
2. Elmer WJ, Allen SM, Eagar TW. 1989. Microstructural development during solidification of stainless steel alloys. Metall Mater Trans A 20A:2117- 31.
3. Ghosh S, Choi J. 2006. Modeling and experimental verification of transient/residual stresses and microstructure formation in multi-layer laser aided DMD process. J Heat Transfer 128(7): 662-79.
4. Griffith ML, Ensz MT, Puskar JD, Robino CV, Brooks JA, Philliber JA, Smugeresky JE, Hofmeister WH. 2000. Understanding the microstructure and properties of components fabricated by laser engineered net shaping (LENS). Mater Res Soc 625:9-20.
5. Groh III HC. Development of laser fabricated Ti-6Al-4V. NASA Report, NASA/TM-2006-214256; Glenn Research Center, Cleveland, OH.
6. Grujicic M, Gao G, Figliola RS. 2001. Computer simulations of the evolution of solidification microstructure in the LENS™ rapid function process. Appl Surf Sci 183:43-57.
7. Katayama S, Matsunawa A. 1984. Solidification microstructure of laser welded stainless steels. Proc Mater Process Symposium, Laser Inst America. ICALEO, Vol. 44. p. 60.
8. Kobryn PA, Moore EH, Semiatin SL. 2000. Effect of laser power and traverse speed on microstructure, porosity, and build height in laser-deposited Ti-6Al-4V. Scr Mater 43(4):299-305.
9. Lewis GK, Schlienger E. 2000. Practical considerations and capabilities for laser assisted direct metal deposition. Mater Des 21(4):417-23.
10. Mazumder J, Schifferer A, Choi J. 1999. Direct materials deposition: Designed macro and microstructure. Mater Res Innovations 3(3):118-31.
11. Miller RS, Cao G, Grujicic MJ. 2001. Monte carlo simulation of three-dimensional nonisothermal grain-microstructure evolution: Application to LENS rapid fabrication. J Mater Synth Process 9:329-45.
12. Pal TK. 2000. The structure and properties of laser beam welded stainless steels. Proc Mater Process Symposium, Laser Inst America. ICALEO, Vol. 89, p. C192.

- 13.Pan QY, Lin X, Huang WD, Zhou YH, Zhang GL. 1998. Microstructure evolution of Cu-Mn alloy under laser rapid solidification conditions. Mater Res Bulletin33 (11)1621-33.
- 14.Smugeresky JE, Gill DD, Atwood CJ. New low cost material development technique for advancing rapid prototyping manufacturing technology. Sandia Report, SAND2007-7832, 2007; Sandia National Laboratory, Albuquerque, NM.
- 15.Susan DF, Puskar JD, Brooks JA, Robino CV. 2006. Quantitative characterization of porosity in stainless steel LENS powders and deposits. Mater Charact 57(1):36-43.
- 16.Wang L, Felicelli SD. 2007. Process modeling in laser deposition of multilayer SS410 steel. J Manuf Sci Eng 129(6):1028-34.
- 17.Zheng B, Zhou Y, Smugeresky JE, Schoenung JM, Lavernia EJ. 2008. Thermal behavior and microstructure evolution during laser deposition with laser-engineered net shaping: Part II. Experimental investigation and discussion. Metall Mater Trans A 39(9):2237-45.